SENSITIVITY ANALYSIS OF SCATTERING PARAMETERS AND ITS APPLICATIONS

SENSITIVITY ANALYSIS OF SCATTERING PARAMETERS AND ITS APPLICATIONS

By

Yifan Zhang, B.Eng.

A Thesis
Submitted to the Department of Electrical and Computer Engineering
and the School of Graduate Studies
of McMaster University
in Partial Fulfillment of the Requirements
for the Degree of
Doctor of Philosophy

Doctor of Philosophy (2013)
(Electrical and Computer Engineering)

McMaster University
Hamilton, Ontario

TITLE: **Sensitivity Analysis of Scattering Parameters and Its Applications**

AUTHOR: Yifan Zhang
B. Eng. (Electrical Engineering)
Harbin Institute of Technology, Heilongjiang, China

SUPERVISOR: Natalia K. Nikolova, Professor
Ph. D. (University of Electro-Communications)
IEEE Fellow
P. Eng. (Ontario)
Canada Research Chair in High Frequency Electromagnetics

NUMBER OF PAGES: XVII, 154

To the past five years, to the happiness and sharing with my family and friends.

ABSTRACT

This thesis contributes significantly to the advanced applications of scattering parameter sensitivity analysis including the design optimization of high-frequency printed structures and in microwave imaging. In both applications, the methods exploit the computational efficiency of the self-adjoint sensitivity analysis (SASA) approach where only one EM simulation suffices to obtain both the responses and their gradients with respect to the optimizable variables.

An *S*-parameter self-adjoint sensitivity formula for multiport planar structures using the method of moments (MoM) current solution is proposed. It can be easily implemented with existing MoM solvers. The shape perturbation which is required in computing the system-matrix derivatives are accommodated by changing the material properties of the local mesh elements. The use of a pre-determined library system matrix further accelerates the design optimization because the writing/reading of the system matrix to/from the disk is avoided. The design optimization of a planar ultra-wide band (UWB) antenna and a double stub tuner are presented as validation examples.

In the application of the sensitivity-based imaging, the SASA approach allows for real-time image reconstruction once the field distribution of the reference object (RO) is known. Here, the RO includes the known background medium of the object under test

(OUT) and the known antennas. The field distribution can be obtained using simulation or measurement.

The spatial resolution is an important measure of the performance of an imaging technique. It represents the smallest detail that can be detected by a given imaging method. The resolution of the sensitivity-based imaging approach has not been studied before. In this thesis, the resolution limits are systematically studied with planar raster scanning and circular array data acquisition. In addition, the method's robustness to noise is studied. A guideline is presented for an acceptable signal-to-noise ratio (SNR) versus the spatial and frequency sampling rates in designing a data-acquisition system for the method.

This thesis validates the sensitivity-based imaging with measured data of human tissue phantoms for the first time. The differences in dielectric properties of the targets are qualitatively reflected in the reconstructed image. A preliminary study of imaging with inexact background information of the OUT is also presented.

ACKNOWLEDGEMENTS

It is a great pleasure for me to acknowledge many people who made this thesis possible.

First and foremost, I would like to express my sincere gratitude to my supervisor Dr. Natalia K. Nikolova for her expert supervision and guidance, encouragement and patience throughout the course of this work. I am grateful for her continuous support as a great mentor and friend who has been a significant presence in my life. For the past four years, her patience, motivation, enthusiasm and immense knowledge have contributed a lot to my personal growth. I will always be thankful for her endless support in my life and at school. It has been an honor to work with her.

Next, I would like to thank my co-supervisors Dr. John Bandler and Dr. Nagula Sangary, as well as my supervisory committee meeting members, Dr. Mohamed H. Bakr and Dr. Xun Li, for their precious time and valuable suggestions for the work done in this thesis.

I also want to thank all the colleagues and friends from the Computational Electromagnectis Laboratory for all the interesting discussions and fruitful comments and for making our laboratory a pleasant work place. My thanks to all members from our group including: Yunpeng Song, Li Liu, Reza Amineh, Aastha Trehan, Yu Zhang, Haohan Xu, Kaveh Moussakhani, Sheng Tu, Yona Baskharoun, Justin McCombe and Qingsha Cheng.

I would like to thank my family members and relatives in China whom I love so much. I thank my mother and father for their love and endless support. Without their support, I would never reach this far. Finally, I would like to thank my dearest Yanqing for always standing by me, encouraging me and believing in me.

Contents

List of Figures

List of Tables

Chapter 1

INTRODUCTION

1.1 MOTIVATION

A variety of numerical algorithms for full-wave electromagnetic (EM) analysis emerged as computing resources became more powerful and widely available since the 1970s. Accurate and complete field representation has thus become available as long as the respective theoretical models could include all EM interactions. However, these algorithms require significant computer memory and time as opposed to equivalent-circuit models. Even today, full-wave EM analysis appears very slow for modeling and design purposes of a complete microwave structure.

The design sensitivity information is crucial in engineering problems such as optimization, statistical, yield and tolerance analysis. However, the efficient sensitivity analysis with full-wave EM simulations remains a challenge. Adjoint-based approaches to the evaluation of the gradient of microwave systems have been proposed recently [1]-[9]. The system response may be defined as the state variables directly, e.g., the voltages of a circuit, the field distribution or the current density distribution. These are examples of distributed responses. The response may also be in the form of network parameters, e.g.,

S-parameters, which appear in the form of functionals of the state variables, e.g., functionals of the $\mathbf{E}$ field solution.

The adjoint-based approach yields the response and its sensitivity through two analyses: the original structure (or circuit); and the adjoint structure (or circuit). In general, two system analyses are sufficient regardless of the number of design variables. In high-frequency analysis, the adjoint variable method has been applied with the finite element method (FEM) [2][3], the method of moments (MoM) [4]-[6], the finite-difference time-domain (FDTD) method [7], and the transmission-line matrix (TLM) method [8][9].

Since the advent of the self-adjoint EM sensitivity analysis methods [10]-[14], the estimation of the response gradient became more efficient because the analysis of the adjoint problem is avoided. This is achieved by formulating an adjoint-problem solution which can be obtained from the solution of the original problem by simple mathematical transformations. This is the major advantage of the self-adjoint formulations. There, the *S*-parameter sensitivity can be calculated from two types of state variables: surface current solution (or current density) [12] and volume field solution [13][14].

The focus of our work is on the EM sensitivity analysis using: (i) MoM current solutions with applications in design optimization, and (ii) volume field solutions with applications in microwave imaging.

In [11], a new *S*-parameter sensitivity analysis method for three dimensional high-frequency structures is proposed. The advantage of the technique is that it is independent of the EM solver since it requires only the surface current and charge densities for

sensitivity computation. However, it cannot be implemented in the case of infinitesimally thin metallic structures due to the singularities of the current/charge densities.

In [12], a self-adjoint approach to the *S*-parameter sensitivity analysis using MoM solution has been proposed from planar structures. It does not require solving the adjoint problem. To estimate the system-matrix derivatives with respect to shape parameters, the locations of the mesh nodes are changed in the perturbed structure, i.e., it is assumed that the surface MoM mesh can be "stretched" or "shrunk" to accommodate the shape perturbation. The overhead of the sensitivity computation is significant because N (number of design variables) additional matrix fills are performed for the N perturbed structures from which the finite-difference (FD) estimates of the matrix derivatives are computed. In addition, the technique proposed in [12] is not applied to real-world complex structures as it requires access to the MoM system matrix which is usually unavailable to the software users. Even if the system matrix is available, its size is so large for practical structures that the writing/reading of the system matrix to/from the disk is very time consuming.

In [15], the concept of discrete perturbations of metallic structures is first proposed. It has been implemented in the design optimization of antennas. There, every new structure arising during the optimization is "constructed" by switching "on" and "off" patches of the previous iterate where the "on" state corresponds to a metallic patch while the "off" state corresponds to a dielectric surface. Note that these patches may not be as fine as the computational cells as they only serve as "bricks" in the construction of

the antenna. To our knowledge, this technique has not been implemented in response sensitivity analysis or in gradient-based optimization.

In this thesis, an *S*-parameter self-adjoint sensitivity formula for multiport planar structures is proposed which can be easily implemented with existing MoM solvers. In contrast to [12], the mesh nodes are fixed. In this work, the shape perturbations are accommodated by changing the material properties of the local mesh elements. For example, a metallic surface patch in the nominal design can be "de-metalized" to a patch of a dielectric surface. The components that contain design variables are meshed with finer grid. This enables fine tuning during the design optimization and at the same time keeps the computational resources at reasonable levels. In our study, we propose the use of a pre-determined library structure which is large enough to contain all possible metallic shapes arise during the optimization. The corresponding system matrix then can be repeatedly used during design optimization in order to obtain the system matrices of each iterate. Therefore, the writing/reading of the system matrix to/from the disk [12] is avoided. The design optimization of complex structures is greatly accelerated.

Methods to perform the self-adjoint *S*-parameter sensitivity analysis using volume field solutions have also been proposed before. FEM and FDTD field solutions have been used to calculate the *S*-parameter sensitivities in [13] and [14], respectively. The estimation of the sensitivities is efficient as the computation requires only one simulation of the original problem.

In [16], the *S*-parameter sensitivity analysis is for the first time implemented in microwave imaging. There, a new general method for response-sensitivity analysis is

suggested. The method is independent of the forward model, i.e., the method of simulation. Its only restriction is that the problem must be reciprocal, i.e., the medium is linear with symmetric constitutive tensors, $\boldsymbol{\varepsilon} = \boldsymbol{\varepsilon}^T$ and $\boldsymbol{\mu} = \boldsymbol{\mu}^T$.

The detection algorithm generates *Jacobian maps*. They are plots of the Fréchet derivatives, i.e., the derivatives of the response difference function with respect to the voxel permittivities and/or conductivities versus the voxel locations. The sensitivity maps can be interpreted as images showing areas in the background medium where the voxel permittivities differ significantly from those in the object under test (OUT). The method aims at obtaining a diagnostic conclusion of whether scatterers (e.g., defects in materials, abnormal tissues in organs, etc.) are likely to be present or not in the OUT.

The method uses the following information to reconstruct the image: (i) the responses measured with the assumed normal state of the object, i.e., the reference object (RO); (ii) the responses measured with the OUT where there may be abnormalities; (iii) the **E**-field distribution in the RO under the known excitations (can be obtained via simulation or measurement). The differences in the responses acquired with the RO and the OUT are then formed. The derivatives of the RO responses with respect to the complex permittivity of each voxel in the RO are computed using the self-adjoint sensitivity analysis method [14]. Using the response derivatives of the RO, the response-difference derivatives are computed and used to generate Jacobian maps (i.e., maps of the Fréchet derivatives). These maps represent the property difference between the RO and the OUT. Abnormalities are thus identified and localized by significant parameter differences (peaks and dips) in the image.

The advantage of the imaging method is that it does not involve the inversion of a matrix and the computations are fast. The method, on the other hand, requires electromagnetic (EM) simulation or measurement of the RO, which includes the known reference medium and the known antennas. Once the required data from the RO is available, the self-adjoint formulation of the response-sensitivity calculation allows for real-time image reconstruction from the measured microwave responses of any OUT. Multiple ROs can also be used if necessary as this is not going to have significant impact on the time required to obtain an image.

An important measure of the performance of an imaging technique is its *spatial resolution*, i.e., the size of the smallest shape detail in the image. Its value can be defined as the width at the half-power level of the image of a small but detectable object. This value also represents the smallest distance between two small objects which are clearly discernible in the image [17]. If the two objects are close, so that the distance between them is smaller than the spatial resolution, they will appear as a single object in the image. Until now, the resolution of the sensitivity-based imaging approach has not been studied and this is the focus of the current study.

In addition, the method's noise robustness is important for its implementation with realistic microwave measurements. A guideline for an acceptable signal-to-noise ratio is needed in designing a data-acquisition system for the sensitivity-based method. Since the effect of noise has not been studied before, we focus on this problems as well and relate it to the spatial and frequency sampling rates.

Finally, the imaging method is for the first time validated using measured data of

human-tissue phantoms. The phantoms are made to mimic human breast with double tumor simulants with different size and/or contrast. In addition, a preliminary study of imaging without the exact knowledge of the background medium of the OUT is presented based on simulated data of a human tissue model.

1.2 CONTRIBUTIONS

The author has contributed to a number of original developments presented in this thesis. These are briefly described next.

(1) A computationally efficient way of calculating *S*-parameters sensitivities using MoM current solution; published in [18]-[22].

(2) An analytical EM model which allows for fast and accurate computation of the OUT and RO models in sensitivity-based imaging; published in [23][24].

(3) Spatial resolution limits and robustness to noise of the sensitivity-based imaging using data acquired with cylindrical sensor systems; published in [24][25].

(4) Spatial resolution limits and robustness to noise using data acquired with planar raster scanning systems [26].

(5) Image reconstruction using measured data of human-tissue phantom for the first time, published in [27].

(6) Preliminary study of image reconstruction without the exact knowledge of the heterogeneous background medium of the OUT.

1.3 OUTLINE OF THE THESIS

This thesis presents advanced applications of the *S*-parameter sensitivity analysis in: (i) design optimization of high-frequency structures using MoM current solutions; (ii) performance study (resolution and robustness to noise) of the sensitivity-based microwave imaging method.

Chapter 2 starts with the mathematical background of the sensitivity analysis using the self-adjoint approach. In order to formulate a response-sensitivity problem as self-adjoint, one needs the self-adjoint constant κ, which relates the original-problem solution to that of the adjoint problem. Since the EM solvers obtain a system response (such as a network parameter) from the state variables $\boldsymbol{x}$ through a functional $f(\boldsymbol{x})$. The self-adjoint constant κ associated with $f(\boldsymbol{x})$ can be found if the functional $f(\boldsymbol{x})$ is known, which is always the case. The formulation of the sensitivity formula using MoM current solution, which is derived based on the specific EM solver FEKO, is given.

In the study using sensitivity-based imaging method, the *S*-parameters are calculated using field distributions. The self-adjoint constant κ is derived from the relations between the original field distribution $\bar{\mathbf{E}}$ and the adjoint field distributions $\hat{\mathbf{E}}$. The derivation of the self-adjoint constant has been shown in [14][16]. The final result of this theoretical derivation is briefly shown in Chapter 2.

Chapter 3 presents the application of the sensitivity analysis with MoM current solution to design optimization. The self-adjoint approach is implemented with discrete shape perturbations on a non-uniform grid. The technique is illustrated through the *S*-

parameter sensitivity analysis of a planar printed antenna and a microwave double-stub tuner. The computed sensitivities are validated by comparing with the central finite-difference estimates at the response level. Gradient-based design optimization is performed using the sensitivity information.

Chapter 4 studies the resolution and noise robustness of the sensitivity-based imaging method using data acquired with two common approaches: (i) planar raster scanning; and (ii) circular sensor array. The configuration of the data acquisition systems is first presented. The analytical models of the incident and the scattered field are then formulated. The former is exact [29] while the latter is based on the linear Born approximation [30]. The spatial resolution limits are derived from the analytical point-spread function (PSF) of the method and are then validated with double-scatterer imaging examples. The method's robustness to noise with respect to the spatial and frequency sampling rates is then studied.

Chapter 5 presents the results obtained with the sensitivity-based imaging method from the measured and simulated data of tissue phantoms. The experimental validation of our imaging method is presented for the first time. The electrical properties and the size of the OUT phantoms are given. Two box-shaped OUT phantoms are used [31]: (i) two scatterers with different contrast and separated by a distance of 50 mm; (ii) two scatterers with the same contrast and separated by a distance of 15 mm. The RO phantom emulates the normal state of the OUT. It is the same as the respective OUT except that there are no embedded scatterers. Two TEM horn antennas are used as imaging sensors and they are placed on both sides of the phantom while facing each other. During the scan, they move

simultaneously over the acquisition plane. With our current system, the transmission coefficients are obtained in a wide frequency band and are used in 2D image reconstruction. In addition, preliminary study of imaging without the exact knowledge of the background medium of the OUT is also performed based on simulated data.

The thesis concludes with Chapter 6 where conclusions and recommendations for the future work are given.

REFERENCES

[1] N. K. Nikolova, J. W. Bandler, and M. H. Bakr, "Adjoint techniques for sensitivity analysis in high-frequency structure CAD," *IEEE Trans. Microwave Theory Tech*., vol. 52, no. 1, pp. 403–419, Jan. 2004.

[2] H. Akel and J. P. Webb, "Design sensitivities for scattering-matrix calculation with tetrahedral edge elements," *IEEE Trans. Magn*., vol. 36, no. 4, pp. 1043–1046, Jul. 2000.

[3] J. P. Webb, "Design sensitivity of frequency response in 3-D finite-element analysis of microwave devices," *IEEE Trans. Magn*., vol. 38, no. 2, pp. 1109–1112, Mar. 2002.

[4] N. K. Georgieva, S. Glavic, M. H. Bakr, and J. W. Bandler, "Feasible adjoint sensitivity technique for EM design optimization," *IEEE Trans. Microwave Theory Tech*., vol. 50, no. 12, pp. 2751–2758, Dec. 2002.

[5] N. K. Nikolova, R. Safian, E. A. Soliman, M. H. Bakr, and J. W. Bandler, "Accelerated gradient based optimization using adjoint sensitivities," *IEEE Trans. Antennas Propag*., vol. 52, pp. 2147–2157, Aug. 2004.

[6] E. A. Soliman, M. H. Bakr, and N. K. Nikolova, "Accelerated gradient-based optimization of planar circuits," *IEEE Trans. Antennas Propag*., vol. 53, no. 2, pp. 880–883, Feb. 2005.

[7] N. K. Nikolova, H. W. Tam, and M. H. Bakr, "Sensitivity analysis with the FDTD method on structured grids," *IEEE Trans. Microwave Theory Tech*., vol. 52, no. 4, pp. 1207–1216, Apr. 2004.

[8] M. H. Bakr and N. K. Nikolova, "An adjoint variable method for frequency domain TLM problems with conducting boundaries," *IEEE Microwave and Wireless Components Letters*, vol. 13, no. 9, pp. 408–410, Sep. 2003.

[9] M. H. Bakr and N. K. Nikolova, "An adjoint variable method for time domain TLM with fixed structured grids," *IEEE Trans. Microwave Theory Tech*., vol. 52, no. 2, pp. 554–559, Feb. 2004.

[10] M. H. Bakr, N. K. Nikolova, and P. A. W. Basl, "Self-adjoint *S*-parameter sensitivities for lossless homogeneous TLM problems," *Int. J. of Numerical Modelling: Electronic Networks, Devices and Fields*, vol. 18, No. 6, pp. 441–455, Nov./Dec. 2005.

[11] M. S. Dadash, N. K. Nikolova, and J. W. Bandler, "Analytical adjoint sensitivity formula for the scattering parameters of metallic structures," *IEEE Trans. Microwave Theory Tech*., vol. 60, no. 9, pp. 2713–2722, Sep. 2012.

[12] N. K. Nikolova, J. Zhu, D. Li, M. H. Bakr, and J. W. Bandler, "Sensitivity analysis of network parameters with electromagnetic frequency-domain simulators," *IEEE Trans. Microwave Theory Tech.*, vol. 54, no. 2, pp. 670–681, Feb. 2006.

[13] N. K. Nikolova, X. Zhu, Y. Song, A. Hasib, and M. H. Bakr, "S-parameter sensitivities for electromagnetic optimization based on volume field solutions," *IEEE Trans. Microwave Theory Tech.*, vol. 57, no. 6, pp. 1526–1538, June 2009.

[14] Y. Song and N. K. Nikolova, "Memory efficient method for wideband self-adjoint sensitivity analysis," *IEEE Trans. Microwave Theory Tech.*, vol. 56, no. 8, pp. 1917–1927, Aug. 2008.

[15] J. M. Johnson and Y. Rahmat-Samii, "Genetic algorithm and method of moments for the design of integrated antennas," *IEEE Trans. Antennas Propagat.*, vol. 47, no. 10, pp. 1606–1614, Oct. 1999.

[16] L. Liu, A. Trehan, and N. K. Nikolova, "Near-field detection at microwave frequencies based on self-adjoint response sensitivity analysis," *Inverse Problems*, vol. 26, 105001, 2010.

[17] N. K. Nikolova, "Microwave imaging for breast cancer detection," *IEEE Microwave Magazine*, vol. 12, pp. 78–94, 2011.

[18] Y. Zhang, N. K. Nikolova, and M. H. Bakr, "Sensitivity analysis with discrete perturbations on method-of-moment grids," *The 26th Annual Review of Progress in Applied Computational Electromagnetics (ACES 2010)*, Apr. 2010.

[19] Y. Zhang and N. K. Nikolova, “Sensitivity analysis with discrete perturbation of planar structure on method-of-moment grids,” *IEEE AP-S/URSI Int. Symp. on Antennas and Propagation*, July 2010.

[20] Y. Zhang, N. K. Nikolova, and M. H. Bakr, “Input impedance sensitivity analysis of patch antenna with discrete perturbations on method-of-moment grids,” *Applied Computational Electromagnetics Society Journal*, vol. 25, no. 10, pp. 867−876, Oct. 2010.

[21] Y. Zhang, A. Pimpale, M. K. Meshram, and N. K. Nikolova, “Printed antenna design using sensitivity analysis based on method of moment solutions,” *IEEE Radio and Wireless Week (RWW 2012)*, Jan. 2012.

[22] Y. Zhang, N. K. Nikolova, and M. K. Meshram, “Design optimization of planar structures using self-adjoint sensitivity analysis,” *IEEE Trans. Antennas Propag*. vol. 60, no. 6, pp. 3060−3066, June 2012.

[23] Y. Zhang, L. Liu, and N. K. Nikolova, “Performance study of a microwave imaging method based on self-adjoint sensitivity analysis,” *European Radar Conference (EuRad 2011)*, Oct. 2011.

[24] Y. Zhang, S. Tu, R. K. Amineh, and N. K. Nikolova, “The resolution and robustness to noise study of a sensitivity-based microwave imaging with data acquired on cylindrical surfaces,” *Inverse Problems*, vol. 28, 115006, 2012.

[25] Y. Zhang, L. Liu, and N. K. Nikolova, “Resolution study for detection algorithm based on self-adjoint sensitivity analysis with microwave responses,” *The 27th*

Annual Review of Progress in Applied Computational Electromagnetics Symposium (ACES 2011), Mar. 2011.

[26] Y. Zhang, S. Tu, and N. K. Nikolova, "The resolution and robustness to noise study of a sensitivity-based microwave imaging using planar raster scanning," in progress.

[27] Y. Zhang, S. Tu, and N. K. Nikolova, "Sensitivity-based microwave imaging with raster scanning," *IEEE MTT-S Int. Microwave Symposium*, June 2012.

[28] Sonnet ***em***, Suites 12.52, Sonnet Software, Inc., USA, 2009.

[29] C. A. Balanis, *Advanced Engineering Electromagnetics*. New York: J. Wiley & Sons,1989.

[30] W. C. Chew, *Waves and Fields in Inhomogeneous Media*. New York: IEEE PRESS, 1995.

[31] R. K. Amineh, M. Ravan, A. Trehan, and N. K. Nikolova, "Near-field microwave imaging based on aperture raster scanning with TEM horn antennas," *IEEE Trans. Antennas Propag*., vol. 59, no. 3, pp. 928–940, Mar. 2011.

Chapter 2

BACKGROUND

2.1 INTRODUCTION

The design sensitivity analysis of a distributed system is important when there is need to improve its performance and/or to know its uncertainties [1]. The design sensitivity is comprised of the derivatives of the responses with respect to the design variables, e.g., shape or material parameters. Engineering problems such as manufacturing and yield tolerances, design of experiments and models, and design optimization, can all benefit from the knowledge of the response sensitivities.

The adjoint-variable method is known to be one of the most efficient approaches to design sensitivity analysis for problems of high complexity where the number of state variables is much larger than the required number of response derivatives. In high-frequency analysis, the adjoint-variable method has been applied with the transmission-line matrix (TLM) method [2][3], the finite-element method (FEM) [4][5], the method of moments (MoM) [6]-[8], and the finite-difference time-domain (FDTD) method [9].

The adjoint-variable approach to response-sensitivity analysis is significantly more efficient than the response-level approximations such as finite differences. This is because it requires two system analyses at the most, regardless of the number of the

system parameters. The accuracy of the adjoint-based sensitivity estimation is of the same order as that of the responses and it does not suffer from catastrophic cancellations. Note that the adjoint-variable sensitivity computation is exact when the derivatives of the system matrices with respect to the system variables are analytically available. However, since the computation uses field solutions of finite numerical accuracy, its output is not exact and some degradation of accuracy may be expected due to the errors in the EM simulations.

Sensitivity analysis with a self-adjoint approach has been proposed with various EM numerical methods including the TLM method [10][11], the FEM method [12][13], the MoM [14], and the FDTD method [15]-[17]. Note that some of the methods based on volume field solution, e.g., [13][17], are applicable with any EM solver capable of producing the required field distributions since they are independent from the respective numerical methods.

In the self-adjoint approach, the second (adjoint) system analysis is eliminated which further improves the efficiency of the sensitivity evaluation. This is achieved by formulating an adjoint-problem solution which can be obtained from the solution of the original problem by simple mathematical transformations. This is the major advantage of the self-adjoint formulations. The self-adjoint sensitivity analysis (SASA) is possible due to the reciprocity of the EM problem. The time required by the SASA computation is negligible compared with the simulation time of the EM problem.

A SASA approach using MoM current solution has been proposed in [14]. The overhead of the sensitivity computation is reduced compared to the adjoint-variable

method [6]-[8]. However, the computation is still significant because N (number of design variables) additional matrix fills are performed for the N perturbed structures from which the finite-difference (FD) estimates of the matrix derivatives are computed. In addition, the size of the system matrix is usually very large for practical structures. Thus, the writing/reading of the system matrix to/from the disk is very time consuming. These drawbacks form the focus of our work which is discussed in detail in Chapter 3.

In the formulation of the S-parameter sensitivity analysis with field solutions, the self-adjoint constant is obtained by relating the adjoint problem (adjoint field distribution) to the original problem (original field distribution). Substantial work has been done in this regard [12][16][17]. The final result of the derivation of the SASA formula using field solution is briefly summarized in this chapter.

In the work presented in [17], the sensitivity-based imaging method has been implemented in numerical examples with circular-sensor array data-acquisition system. There, the concept of the method is shown to be valid in a preliminary study. However, a systematic study is still needed on the method's resolution limit and its robustness to noise. In addition, the method has never been applied to image reconstruction using planar surface acquisition and measurements of tissue phantoms. All these problems will be addressed in Chapters 4 and 5.

2.2 REVIEW OF *S*-PARAMETER SENSITIVITY ANALYSIS WITH METHOD OF MOMENTS SOLUTIONS

Using the MoM, a time-harmonic EM problem involving linear materials can be reduced to a linear system of equations:

$$\boldsymbol{A}(\boldsymbol{p})\boldsymbol{x} = \boldsymbol{b}\,. \tag{2.1}$$

The system matrix $\boldsymbol{A} \in \mathbb{C}^{M\times M}$ is a function of the shape and material parameters $\boldsymbol{p} \in \mathbb{R}^{N\times 1}$. Here, M is the number of state variables and N is the number of design variables. $\boldsymbol{x} \in \mathbb{C}^{M\times 1}$ is the vector of state variables and $\boldsymbol{b} \in \mathbb{C}^{M\times 1}$ is the excitation vector. For now, we assume that $\boldsymbol{x}$ represents the current solution, i.e., $\boldsymbol{x} \equiv \boldsymbol{I}$.

We define a general response function $f(\boldsymbol{p}, \boldsymbol{x}(\boldsymbol{p}))$ of the linear system satisfying (2.1). It depends on the design parameters $\boldsymbol{p}$ implicitly through $\boldsymbol{x}$ but may also have explicit dependence on $\boldsymbol{p}$. The objective of the sensitivity analysis is to obtain the gradient of the system response, i.e.,

$$\nabla_{\boldsymbol{p}} f \text{, subject to } \boldsymbol{A}\boldsymbol{x} = \boldsymbol{b} \tag{2.2}$$

where

$$\nabla_{\boldsymbol{p}} = \left[\frac{\partial}{\partial p_1}, \frac{\partial}{\partial p_2}, \ldots, \frac{\partial}{\partial p_N}\right]. \tag{2.3}$$

The gradient $\nabla_{\boldsymbol{p}} f$ can be obtained as [6]:

$$\nabla_{\boldsymbol{p}} f = \nabla_{\boldsymbol{p}}^{e} f + \hat{\boldsymbol{x}}^T \cdot \left[\nabla_{\boldsymbol{p}} \boldsymbol{b} - \nabla_{\boldsymbol{p}}(\boldsymbol{A}\bar{\boldsymbol{x}})\right] \tag{2.4}$$

where $\nabla_{\boldsymbol{p}}^{e} f$ reflects the explicit dependence of f on $\boldsymbol{p}$. $\bar{\boldsymbol{x}}$ is the solution to the system of

equations (2.1) and it is not subject to differentiation in $\nabla_{\boldsymbol{p}}(\boldsymbol{A}\bar{\boldsymbol{x}})$. Here, it is assumed that the excitation vector $\boldsymbol{b}$ is independent of $\boldsymbol{p}$ because the network ports serve as a reference and are not subject to design changes. Therefore, we have $\nabla_{\boldsymbol{p}}\boldsymbol{b} = \boldsymbol{0}$.

The adjoint state-variable vector $\hat{\boldsymbol{x}}$ satisfies the *adjoint system*:

$$\boldsymbol{A}^T \hat{\boldsymbol{x}} = \hat{\boldsymbol{b}}. \tag{2.5}$$

Here, $\hat{\boldsymbol{b}}$ is the *adjoint excitation*,

$$\hat{\boldsymbol{b}} = \left[\nabla_{\boldsymbol{x}} f\right]^T. \tag{2.6}$$

We assume that the EM problem is reciprocal and, therefore, (2.1) can be cast in a symmetric form, i.e.,

$$\boldsymbol{A} = \boldsymbol{A}^T. \tag{2.7}$$

Note that the system matrices are exactly symmetric only if Galerkin's discretization procedure is applied in the MoM. However, due to the reciprocity of the linear EM problem, even with other techniques, the system matrix tends to be symmetric when the mesh is sufficiently fine [14]. Here, we use the MoM based simulator Sonnet ***em*** [18] and FEKO [19] whose system matrices satisfy (2.7) exactly.

Observing (2.1) and (2.5), if the adjoint system has the form

$$\boldsymbol{A}\hat{\boldsymbol{x}} = \kappa \boldsymbol{b}, \tag{2.8}$$

then the adjoint solution can be obtained directly as

$$\hat{\boldsymbol{x}} = \kappa \boldsymbol{x}. \tag{2.9}$$

Here, the *self-adjoint constant* κ is introduced to relate the adjoint and the original system solutions.

In [14], the self-adjoint constant is derived based on the MoM-based EM solver FEKO and it is obtained as

$$\kappa_{jk} = -\frac{2Z_0}{V_e^{(j)} V_e^{(k)}}. \tag{2.10}$$

Here, Z_0 is the system impedance, $V_e^{(\upsilon)}$ ($\upsilon = j,k$) is the υ-th port voltage source. The subscript *jk* in κ_{jk} denotes that the self-adjoint constant relates to the particular response S_{jk}.

The final expression for calculating the *S*-parameter sensitivity is given as

$$\begin{aligned} &\frac{\partial S_{jk}}{\partial p_n} = \frac{2Z_0}{V_e^{(j)} V_e^{(k)}} \left(\bar{\boldsymbol{I}}^{(j)} \right)^T \cdot \frac{\partial \boldsymbol{A}}{\partial p_n} \cdot \bar{\boldsymbol{I}}^{(k)}, \\ &j,k = 1,2,\ldots,K;\ n = 1,2,\ldots,N. \end{aligned} \tag{2.11}$$

Here, κ denotes the number of ports and $\bar{\boldsymbol{I}}^{(\xi)}$ ($\xi = j,k$) is the current distribution when the ξ-th port is excited. Note that (2.11) is derived for the specific MoM simulator in the FEKO software where the *S*-parameters are calculated from the current solution.

In (2.11), the derivative of the system matrix with respect to the shape parameter is computed using the first-order finite-difference approximation [14]

$$\frac{\partial \boldsymbol{A}}{\partial p_n} \approx \frac{\Delta \boldsymbol{A}}{\Delta p_n} = \frac{\boldsymbol{A}_n - \boldsymbol{A}}{\Delta p_n}. \tag{2.12}$$

Here, $\boldsymbol{A}_n = \boldsymbol{A}(\boldsymbol{p} + \Delta p_n \cdot \boldsymbol{u}^{(n)})$, where $\boldsymbol{u}^{(n)}$ is a vector whose elements are all zero except the *n*-th one, $u_n = 1$. Note that (2.12) is applicable only if $\boldsymbol{A}_n$ and $\boldsymbol{A}$ are of the same size, i.e., the two respective meshes contain the same number of nodes and elements. Moreover, the numbering of the nodes and elements must correspond to the same locations (within the prescribed perturbation) in the original and perturbed structures, i.e., the mesh topology must be preserved [14].

Specificaly, to estimate (2.12), the locations of the mesh nodes are changed in the perturbed structure, i.e., it is assumed that the surface MoM mesh can be "stretched" or "shrunk" to accommodate the shape perturbation. Thus, the overhead of the sensitivity computation is significant because *N* additional matrix fills are performed for the *N*-th perturbed structures to form $\boldsymbol{A}_n$, $n = 1, ..., N$. In addition, the technique proposed in [14] is not applied to real-world complex structures as it requires access to the MoM system matrix which is usually unavailable to the software users. Even if the system matrix is available, its size is usually very large for practical structures, which makes the writing/reading of the system matrix to/from the disk prohibitive.

2.3 REVIEW OF *S*-PARAMETER SENSITIVITY ANALYSIS WITH VOLUME FIELD SOLUTIONS

The generic response in the frequency-domain EM sensitivity analysis is the functional

$$F(\mathbf{E}, \mathbf{p}) = \iiint_{\Omega} f(\mathbf{E}, \mathbf{p}) d\Omega \tag{2.13}$$

where Ω is the computational volume, $\mathbf{E}$ is the field solution, and $f(\mathbf{E},\mathbf{p})$ is the local response, which depends on the field solution $\mathbf{E}$.

The goal of sensitivity analysis is to compute the response gradient (response sensitivity) $\nabla_{\boldsymbol{p}} F$. In this study, we focus on *S*-parameter sensitivity analysis with respect to the constitutive parameter $p^{(m)}(\boldsymbol{r}')$ of voxel at location $\boldsymbol{r}'$. Here, *m* denotes the *m*-th sampled frequency ($m = 1,\ldots,N_{\mathrm{f}}$), in the cases where the constitutive parameters are frequency-dependent.

One application of the self-adjoint sensitivity analysis with volume field solutions is in microwave imaging [17]. For a receiving antenna of the dipole type, we can assume that the *S*-parameter can be computed using

$$S_{jk}^{(m)} = \mathbf{E}_{jk}^{(m)} \cdot \boldsymbol{\rho}_j \tag{2.14}$$

where $\boldsymbol{\rho}_j$ is the polarization vector of the *j*-th receiving antenna and $\mathbf{E}_{jk}^{(m)}$ is the $\mathbf{E}$-field at position $\boldsymbol{r}_j$ when the transmitter at position $\boldsymbol{r}_k$ radiates at the *m*-th frequency ($m = 1,\ldots,N_{\mathrm{f}}$).

Having $F \equiv S_{jk}^{(m)}$ in (2.13), the derivative of $S_{jk}^{(m)}$ with respect to the voxels' permittivities/conductivities can be written as [17]:

$$\frac{\partial S_{jk}^{(m)}}{\partial p^{(m)}(\boldsymbol{r}')} = -\kappa_j^{(m)} \iiint_{\Omega} \mathbf{E}^{(m)}(\boldsymbol{r}',\boldsymbol{r}_j) \cdot \frac{\partial R\left[\mathbf{E}^{(m)}(\boldsymbol{r}',\boldsymbol{r}_k)\right]}{\partial p^{(m)}(\boldsymbol{r}')} \mathrm{d}\Omega . \tag{2.15}$$

Here, $p^{(m)}(\boldsymbol{r}') = \varepsilon_{\mathrm{r}}^{(m)}(\boldsymbol{r}')$, $\sigma^{(m)}(\boldsymbol{r}')$; where $\varepsilon_{\mathrm{r}}^{(m)}(\boldsymbol{r}')$ and $\sigma^{(m)}(\boldsymbol{r}')$ are the relative permittivity and conductivity of the voxel at $\boldsymbol{r}'$. $\mathbf{E}^{(m)}(\boldsymbol{r}', \boldsymbol{r}_\xi)$ ($\xi = j, k$) is the m-th frequency incident **E**-field at location $\boldsymbol{r}'$ when the transmitter is at $\boldsymbol{r}_\xi$. Also,

$$\frac{\partial R\left[\mathbf{E}^{(m)}(\boldsymbol{r}', \boldsymbol{r}_k)\right]}{\partial p^{(m)}(\boldsymbol{r}')} = k_m^2 \mathbf{E}^{(m)}(\boldsymbol{r}', \boldsymbol{r}_k) \cdot \frac{\partial}{\partial p^{(m)}(\boldsymbol{r}')}\left[\varepsilon_{\mathrm{r}}^{(m)}(\boldsymbol{r}') - j\frac{\sigma^{(m)}(\boldsymbol{r}')}{\omega_m \varepsilon_0}\right] \tag{2.16}$$
$$p^{(m)} = \varepsilon_{\mathrm{r}}^{(m)}, \sigma^{(m)}$$

where $k_m = \omega_m \sqrt{\mu_0 \varepsilon_0}$ is the wavenumber.

In the case where the source is a current excitation, the self-adjoint constant in (2.15) is

$$\kappa_j^{(m)} = -\frac{1}{\mathrm{i} J_j^{(m)} \omega_m \mu_0 \Delta\Omega_j}. \tag{2.17}$$

Here, $J_j^{(m)}$ is the current density of the j-th point-like dipole antenna, μ_0 is the permeability of vacuum, and $\Delta\Omega_j$ is the volume of the antenna where $J_j^{(m)}$ exists.

For the completeness of this review, we also present the S-parameter self-adjoint sensitivity formula in the general case of port excitation. The general S-parameter is defined as [12]

$$S_{jk}^{(m)(w)} = \frac{\iint_{S_j} \left(\mathbf{E}_{k0}^{(m)} \times \mathbf{h}_j^{(m)(w)}\right) \cdot d\boldsymbol{s}}{\iint_{S_k} \left(\mathbf{E}_{k,\mathrm{inc}}^{(m)} \times \mathbf{h}_k^{(m)(w)}\right) \cdot d\boldsymbol{s}} - \delta_{jk} \tag{2.18}$$
$$\delta_{jk} = \begin{cases} 1, & j = k, \\ 0, & j \neq k, \end{cases}$$

where w denotes the desired mode, $h_{\xi}^{(m)(w)}$ ($\xi = j,k$) is the dual (or magnetic) port modal vector, $\mathbf{E}_{k0}^{(m)}$ is the field resulting from exciting the k-th port, and $\mathbf{E}_{k,\mathrm{inc}}^{(m)}$ is the incident field at the k-th port. The port surfaces are s_j and s_k.

The derivative of the S-parameter with respect to the voxels' permittivies/conductivities is again calculated using (2.15) but the slef-adjoint constant which corresponds to the general S-parameter definition in (2.18) is now [12]:

$$\kappa_j^{(m)} = \frac{1}{\mathrm{i}2V_j^{(m)}V_k^{(m)}\omega_m\mu_0}. \tag{2.19}$$

Here, $V_{\xi}^{(m)}$ ($\xi = j,k$) is the modal magnitude of the excitation at the ξ-th port.

In summary, (2.15) is the sensitivity formula for computing the derivatives of the S-parameters with respect to a voxel's constitutive properties. In the work presented in [17], point-like current source excitation is used and the sensitivity is calculated using (2.17). In [17], the concept of the sensitivity-based imaging has been validated through numerical examples with circular sensor-array data acquisition system. The target can be shown as peaks or dips in the image. However, the method's resolution limits and the robustness to noise have never been systematically studied. In addition, the method has not been implemented using numerical models or measured phantoms with planar raster scanning data acquisition. These problems are in the focus of our work on the sensitivity-based imaging method which is discussed in Chapters 4 and 5.

2.4 CONCLUSION

The self-adjoint approach to sensitivity analysis improves significantly the computation since solving the adjoint problem is avoided. The mathematical background of the previous approaches to the *S*-parameters self-adjoint sensitivity analysis (SASA) derivation using MoM current solution is briefly presented. The sensitivity formula based on a specific MoM solver (FEKO) is also given. The drawbacks of the existing SASA technique have been stated; these form the focus of our work discussed in Chapter 3.

A review of the *S*-parameter sensitivity analysis formulation with volume field solution is also briefly discussed. Its application to microwave imaging has been proven promising in previous preliminary studies. Yet, systematic evaluation of the method's resolution limits and robustness to noise has not been performed. Also, its implementation with measured data has never been addressed before. Here, we address all these unsolved problems and for the first time validate the method with measured data acquired with tissue phantoms.

REFERENCES

[1] D. G. Cacuci, *Sensitivity & Uncertainty Analysis, Volume 1: Theory*. Boca Raton, FL: Chapman & Hall/CRC, 2003.

[2] M. H. Bakr and N. K. Nikolova, “An adjoint variable method for frequency domain TLM problems with conducting boundaries,” *IEEE Microwave and Wireless Components Letters*, vol. 13, no. 9, pp. 408–410, Sep. 2003.

[3] M. H. Bakr and N. K. Nikolova, “An adjoint variable method for time domain TLM with fixed structured grids,” *IEEE Trans. Microwave Theory Tech*., vol. 52, no. 2, pp. 554–559, Feb. 2004.

[4] H. Akel and J. P. Webb, “Design sensitivities for scattering-matrix calculation with tetrahedral edge elements,” *IEEE Trans. Magn*., vol. 36, no. 4, pp. 1043–1046, Jul. 2000.

[5] J. P. Webb, “Design sensitivity of frequency response in 3-D finite-element analysis of microwave devices,” *IEEE Trans. Magn*., vol. 38, no. 2, pp. 1109–1112, Mar. 2002.

[6] N. K. Georgieva, S. Glavic, M. H. Bakr, and J. W. Bandler, “Feasible adjoint sensitivity technique for EM design optimization,” *IEEE Trans. Microwave Theory Tech*., vol. 50, no. 12, pp. 2751–2758, Dec. 2002.

[7] N. K. Nikolova, R. Safian, E. A. Soliman, M. H. Bakr, and J. W. Bandler, “Accelerated gradient based optimization using adjoint sensitivities,” *IEEE Trans. Antennas Propag*., vol. 52, pp. 2147–2157, Aug. 2004.

[8] E. A. Soliman, M. H. Bakr, and N. K. Nikolova, “Accelerated gradient-based optimization of planar circuits,” *IEEE Trans. Antennas Propag*., vol. 53, no. 2, pp. 880–883, Feb. 2005.

[9] N. K. Nikolova, H. W. Tam, and M. H. Bakr, “Sensitivity analysis with the FDTD method on structured grids,” *IEEE Trans. Microwave Theory Tech.*, vol. 52, no. 4, pp. 1207–1216, Apr. 2004.

[10] M. H. Bakr, N. K. Nikolova, and P. A. W. Basl, “Self-adjoint *S*-parameter sensitivities for lossless homogeneous TLM problems,” *Int. J. of Numerical Modelling: Electronic Networks, Devices and Fields*, vol. 18, no. 6, pp. 441–455, Nov./Dec. 2005.

[11] P. A. W. Basl, M. H. Bakr, and N. K. Nikolova, “Theory of self-adjoint S-parameter sensitivities for lossless nonhomogeneous transmission-line modeling problems,” *IET Microwave Antennas Propag.*, vol. 2, no. 3, pp. 211–220, Apr. 2008.

[12] N. K. Nikolova, X. Zhu, Y. Song, A. Hasib, and M. H. Bakr, “*S*-parameter sensitivities for electromagnetic optimization based on volume field solutions,” *IEEE Trans. Microwave Theory Tech.*, vol. 57, no. 6, pp. 1526–1538, June 2009.

[13] M. S. Dadash, N. K. Nikolova, and J. W. Bandler, “Analytical adjoint sensitivity formula for the scattering parameters of metallic structures,” *IEEE Trans. Microwave Theory Tech.*, vol. 60, no. 9, pp. 2713–2722, Sep. 2012.

[14] N. K. Nikolova, J. Zhu, D. Li, M. H. Bakr, and J. W. Bandler, “Sensitivity analysis of network parameters with electromagnetic frequency-domain simulators,” *IEEE Trans. Microwave Theory Tech.*, vol. 54, no. 2, pp. 670–681, Feb. 2006.

[15] N. K. Nikolova, Y. Li, Y. Li, and M. H. Bakr, “Sensitivity analysis of scattering parameters with electromagnetic time-domain simulators,” *IEEE Trans. Microwave Theory Tech.*, vol. 54, No. 4, pp. 1598–1610, Apr. 2006.

[16] Y. Song and N. K. Nikolova, “Memory efficient method for wideband self-adjoint sensitivity analysis,” *IEEE Trans. Microwave Theory Tech.*, vol. 56, no. 8, pp. 1917–1927, Aug. 2008.

[17] L. Liu, A. Trehan, and N. K. Nikolova, “Near-field detection at microwave frequencies based on self-adjoint response sensitivity analysis,” *Inverse Problems*, vol. 26, 105001, 2010.

[18] Sonnet ***em***, Suites 12.52, Sonnet Software, Inc., USA, 2009.

[19] FEKO, Suites 6.0, EM Software & Sustems Ltd., USA, 2011.

Chapter 3

SENSITIVITY ANALYSIS WITH METHOD-OF-MOMENT SOLUTIONS

3.1 INTRODUCTION

Adjoint-variable sensitivity analysis approaches have been developed before for the method of moments (MoM) [1]-[3]. Their computational speed is limited by performing an adjoint-system analysis and/or the need to estimate the derivative of the system matrix. The self-adjoint sensitivity analysis (SASA) technique using MoM solutions has been proposed in [4]. The sensitivity analysis is accelerated since solving the adjoint problem is avoided. However, the method proposed in [4] has had limited applications as explained next.

The overhead of the sensitivity computation in [4] is still significant because N additional matrix fills are performed for the perturbed structures in order to compute the finite-difference (FD) estimates of the matrix derivatives. In addition, the method is not applied to real-world complex structures. This is because it requires access to the MoM system matrix which is usually unavailable to the software users. Even if the system matrix is available, its size is usually very large for practical structures; thus, it is very time consuming to write/read the system matrix to/from the disk during optimization.

To avoid the N additional matrix fills and the writing/reading of these matrices to/from the disk [4], discrete perturbations of the shape parameters on a pre-determined non-uniform MoM grid are proposed here and the grid is used repeatedly to perform sensitivity analysis. The shape perturbations are accommodated by changing the material properties of the local mesh elements. For example, a metallic surface patch in the nominal design can be "de-metalized" to a patch of a dielectric surface. The components that contain design variables are meshed with finer grid. This enables fine tuning during the design optimization and at the same time keeps the computational resources at reasonable levels. The pre-determined system matrix can be repeatedly used during design optimization. The design optimization of complex structures is greatly accelerated as the matrix fills and the writing/reading of the system matrix to/from the disk [4] are avoided.

To calculate the S-parameters sensitivities using the self-adjoint approach, the formula is derived for multi-port structures based on the MoM solver Sonnet ***em*** which can provide the system matrix to the user. In the self-adjoint sensitivity analysis (SASA) problem, the self-adjoint constant κ is needed. It relates the original-problem excitation to that of the adjoint problem and, due to the linearity of the EM problem, it also relates the original and adjoint field solutions. A system response $f(\boldsymbol{x})$ (such as a network parameter) is obtained from the EM state variables (representing the field solution) $\boldsymbol{x}$. The self-adjoint constant κ for a given response can be found once $f(\boldsymbol{x})$ is known. In the formulation of the S-parameters sensitivity analysis with current solutions, we consider the MoM-based solver Sonnet ***em*** [5]. It calculates the S-parameters using the Y-

parameters, which are computed from the current solution $\boldsymbol{I}$ at the ports. Thus, the self-adjoint constant is first derived for the *Y*-parameters. Then the *S*-parameter sensitivities are calculated from those of the *Y*-parameters.

In this chapter, the *S*-parameter sensitivity formula is first derived from the sensitivities of the *Y*-parameters and is then implemented in the design optimization of a printed patch antenna and a stub tuner.

3.2 SENSITIVITY FORMULA USING MOM CURRENT SOLUTIONS

Here, our derivation of the self-adjoint sensitivity formula using MoM current solutions is presented. We use MoM solvers, e.g., Sonnet ***em***, for planar microwave structures, that calculate first the *Y*-parameters from which the *S*-parameters are obtained. In order to obtain the self-adjoint constants for the *S*-parameters, those for the *Y*-parameters have to be obtained first.

The derivatives of the *S*-parameters can be expressed through the derivatives of the *Y*-parameters using the chain rule:

$$\frac{\partial S_{jk}}{\partial p_n} = \sum_{r,q=1}^{K} \left(\frac{\partial S_{jk}}{\partial Y_{rq}} \cdot \frac{\partial Y_{rq}}{\partial p_n} \right), \quad \begin{matrix} j,k = 1,\ldots,K \\ r,q = 1,\ldots,K \end{matrix} \tag{3.1}$$

where n = 1,…, N, and K is the number of ports. The *S*-parameters relate to the *Y*-parameters as

$$\boldsymbol{S} = \left(\boldsymbol{Y}_0 - \boldsymbol{Y}\right)\left(\boldsymbol{Y}_0 + \boldsymbol{Y}\right)^{-1} \tag{3.2}$$

where $\boldsymbol{Y}_0 = diag[1/Z_{01}, 1/Z_{02},\ldots, 1/Z_{0K}]$ is a diagonal matrix and Z_{0s} ($s = 1,...,K$) is the s-th port impedance. The derivatives $\partial S_{jk} / \partial Y_{rq}$ are analytically available from (3.2).

By definition, the Y-parameters relate the port currents and voltages as

$$I_r = \sum_{r=1}^{K} Y_{rq} V_q \ . \tag{3.3}$$

Here, I_r is the current at port r and V_q is the voltage at the port q. V_q takes the value of 1 V or 0 V, depending on whether it is excited or not. Thus, (3.3) is rewritten as

$$I_r^{(q)} = Y_{rq} \ . \tag{3.4}$$

The superscript q of $I_r^{(q)}$ denotes the excited port q. Assuming the edge of port r is discretized into M_r segments, $I_r^{(q)}$ is given by

$$I_r^{(q)} = \sum_{h=1}^{M_r} J_{r,h}^{(q)} \cdot d_h^r \ . \tag{3.5}$$

Here, $J_{r,h}^{(q)}$ is the surface current density normal to the h-th mesh segment (with length d_h^r) at port r when port q is excited. Note that the excitation of the original system (2.1) when port r is excited is:

$$\boldsymbol{b}^{(r)} = [0,\ldots,0, \underbrace{1,\ldots,1}_{M_r \text{ elements}}, 0,\ldots,0]^T \ . \tag{3.6}$$

The derivatives of the Y-parameters with respect to a specific parameter p_n are obtained by replacing the response function f in (2.4) with the Y-parameters:

$$\frac{\partial Y_{rq}}{\partial p_n} = \frac{\partial^e Y_{rq}}{\partial p_n} - \left(\hat{\boldsymbol{x}}_r^{(q)}\right)^T \cdot \frac{\partial \boldsymbol{A}}{\partial p_n} \cdot \bar{\boldsymbol{x}}^{(q)}, \quad \begin{array}{c} r,q = 1,\ldots,K \\ n = 1,\ldots,N. \end{array} \tag{3.7}$$

Here, $\bar{\boldsymbol{x}}^{(q)}$ is the solution of (2.1) when port q is excited. $\hat{\boldsymbol{x}}_r^{(q)}$ is the adjoint solution for the sensitivity of the parameter Y_{rq}. The term $\partial^e Y_{rq} / \partial p_n$ is zero since there is no explicit dependence of Y_{rq} on p_n.

The derivatives of the system matrix are estimated as

$$\frac{\partial \boldsymbol{A}}{\partial p_n} \approx \frac{\Delta \boldsymbol{A}}{\Delta p_n} = \frac{\boldsymbol{A}(p_n + \Delta p_n) - \boldsymbol{A}(p_n - \Delta p_n)}{2\Delta p_n} \tag{3.8}$$

where Δp_n (n = 1,…, N) are the respective parameter perturbations.

Note that the matrices $\partial \boldsymbol{A} / \partial p_n$ (n = 1,…, N) may be analytically available. However, their evaluation is not only solver specific but also it is far from trivial. In addition, the analytical evaluation of the system matrix derivatives does not improve the efficiency as compared to using the finite difference estimates $\Delta \boldsymbol{A} / \Delta p_n$. Therefore, it is often the case that the system matrix derivatives are approximated using finite differences.

In using (3.8), the discrete approach based on a pre-determined library matrix can significantly accelerate the computations. This is explained in detail in Section 3.3.

As per (2.5), the adjoint solution $\hat{\boldsymbol{x}}_r^{(q)}$ in (3.7) is the solution to the adjoint system of equations:

$$\boldsymbol{A}\hat{\boldsymbol{x}}_r^{(q)} = \left(\nabla_{\boldsymbol{x}^{(q)}} Y_{rq}\right)^T . \tag{3.9}$$

Here, $(\nabla_{\boldsymbol{x}^{(q)}} Y_{rq})^T$ is the adjoint excitation, which, according to (3.4), is

$$\hat{\boldsymbol{b}}_{rq} = \left(\nabla_{\boldsymbol{x}^{(q)}} I_r^{(q)}\right)^T . \tag{3.10}$$

Since we assume that $\boldsymbol{x} \equiv \boldsymbol{I}$ are the corresponding currents of the MoM solution, according to (3.5) and (3.10), the adjoint excitation is

$$\hat{\boldsymbol{b}}_{rq} = [0,\ldots,0,\ \underbrace{1,\ldots,1}_{M_r \text{ elements}},0,\ldots,0]^T . \tag{3.11}$$

This excitation is the same as the excitation of the original system when port r is excited. Thus, we have $\hat{\boldsymbol{x}}_r^{(q)} = \overline{\boldsymbol{x}}^{(r)}$ and $\kappa_{rq} = 1$, where $\overline{\boldsymbol{x}}^{(r)}$ is the solution of (2.1) when port r is excited. Note that the subscript rq in κ_{rq} denotes that the self-adjoint constant is related to the particular response Y_{rq}.

Thus, the respective derivatives of the Y-parameter in (3.7) are computed as

$$\frac{\partial Y_{rq}}{\partial p_n} = -\left(\overline{\boldsymbol{I}}^{(r)}\right)^T \cdot \frac{\partial \boldsymbol{A}}{\partial p_n} \cdot \overline{\boldsymbol{I}}^{(q)}, \quad \begin{array}{l} r,q = 1,\ldots,K, \\ n = 1,\ldots,N. \end{array} \tag{3.12}$$

Here, $\overline{\boldsymbol{I}}^{(r)}$ and $\overline{\boldsymbol{I}}^{(q)}$ are the current solution vectors, when the original system is excited at port r and port q, respectively.

Now, (3.1) can be re-written as

$$\begin{array}{l} \dfrac{\partial S_{jk}}{\partial p_n} = -\displaystyle\sum_{r,q=1}^{K} \left[\frac{\partial S_{jk}}{\partial Y_{rq}} \cdot \left(\overline{\boldsymbol{I}}^{(r)}\right)^T \cdot \frac{\partial \boldsymbol{A}}{\partial p_n} \cdot \overline{\boldsymbol{I}}^{(q)} \right], \\ j,k = 1,2,\ldots,K;\ n = 1,2,\ldots,N. \end{array} \tag{3.13}$$

This is the formula for the S-parameter sensitivity analysis and it is further applied to EM-based design optimization.

For the completeness of this study, the sensitivity formula is also discussed when the MoM solver may provide surface current density solutions. In this case, we have $\boldsymbol{x} \equiv \boldsymbol{J}$. We denote the system matrix as $\boldsymbol{A}'$ in this case, i.e., $\boldsymbol{A}'\boldsymbol{J} = \boldsymbol{b}$.

We assume a matrix whose diagonal elements consist of the discretization segment lengths as:

$$\boldsymbol{B} = diag[d_1, d_2, \ldots, d_M]\,. \tag{3.14}$$

Then, the current solution $\boldsymbol{I}$ and the current density solution $\boldsymbol{J}$ are related as

$$\boldsymbol{I} = \boldsymbol{B}\boldsymbol{J}\,. \tag{3.15}$$

It follows that $\boldsymbol{A}'$ and the system matrix $\boldsymbol{A}$ of the current solution are related as $\boldsymbol{A} = \boldsymbol{A}'\boldsymbol{B}^{-1}$. Now, the *S*-parameter sensitivity (3.13) in the case of current-density solution is:

$$\begin{aligned} \frac{\partial S_{jk}}{\partial p_n} &= -\sum_{r,q=1}^{K}\left[\frac{\partial S_{jk}}{\partial Y_{rq}}\cdot\left(\boldsymbol{B}\overline{\boldsymbol{J}}^{(r)}\right)^T\cdot\frac{\partial(\boldsymbol{A}'\boldsymbol{B}^{-1})}{\partial p_n}\cdot\boldsymbol{B}\overline{\boldsymbol{J}}^{(q)}\right], \\ &= -\sum_{r,q=1}^{K}\left[\frac{\partial S_{jk}}{\partial Y_{rq}}\cdot\left(\boldsymbol{B}\overline{\boldsymbol{J}}^{(r)}\right)^T\cdot\frac{\partial \boldsymbol{A}'}{\partial p_n}\cdot\overline{\boldsymbol{J}}^{(q)}\right], \quad \begin{array}{l} j,k = 1,2,\ldots,K, \\ n = 1,2,\ldots,N. \end{array} \end{aligned} \tag{3.16}$$

3.3 METHOD-OF-MOMENT GRID FOR SENSITIVITY ANALYSIS

A meshing approach for the MoM-based sensitivity analysis is proposed which is particularly suitable for design optimization. It is based on computing first a large *library matrix* $\boldsymbol{A}_{lib}$ for the so called *library structure*. The library structure is a pre-determined structure which is large enough to contain all possible metallic segments in the structure of interests that may arise during sensitivity analysis or design optimization. The corresponding library matrix is then repeatedly used to provide respective system matrices for all iterative structures. Non-uniform square mesh is used to discretize the planar structure. The structure components that are subject to optimization, i.e., they depend on the design variables, are discretized with finer mesh, while the “fixed”

structures (areas that are not changed during the design procedure) are discretized with coarser mesh.

To illustrate the concept, two examples are presented (shown in Fig. 3.1). In Fig. 3.1 (a), a planar antenna fed by a coplanar waveguide (CPW) is shown and the nominal design parameters are also given. The substrate material is FR4 with relative permittivity $\varepsilon_r = 4.4$ and thickness 1.6 mm. The antenna consists of a slotted patch with the exterior length L_p and the exterior width W_p. The length d_4 and width W_2 of the stepped portion of the patch are set to 1 mm and 3.5 mm, respectively. H_f is the distance between the slotted patch and the feed.

The T-shape tuning stub (grey patches) inside the rectangular ring is used here to create a band-notch characteristic. The design variables are W, D, and h, which tune the stub. W is the width of the upper portion of the T-shape stub; D is the width of the lower portion of the stub, and h is the length of the lower portion of the stub. A large region around the T-shape stub, the stub itself and a small portion of the rectangular ring where the stub connects to it are meshed with a fine grid of step size $\delta_2 = 0.25\ \text{mm}$. This fine grid in effect defines all patches which may change from metallic to dielectric or vice versa during the optimization process. Meanwhile, a coarser grid of step size $\delta_1 = 0.50\ \text{mm}$ is used to mesh the area where changes in the geometry are not allowed, for example, the CPW. All shown mesh patches are assumed to be metallic in the library structure (patches in both white and grey). A library matrix $\boldsymbol{A}_{lib}$ is thus generated based on the library structure. Any new structure can be viewed as a subset of the library structure

indicated by the grey area. Each new system matrix $\boldsymbol{A}$ can be obtained by switching off/on the corresponding elements of $\boldsymbol{A}_{lib}$ by eliminating/adding the respective rows and columns.

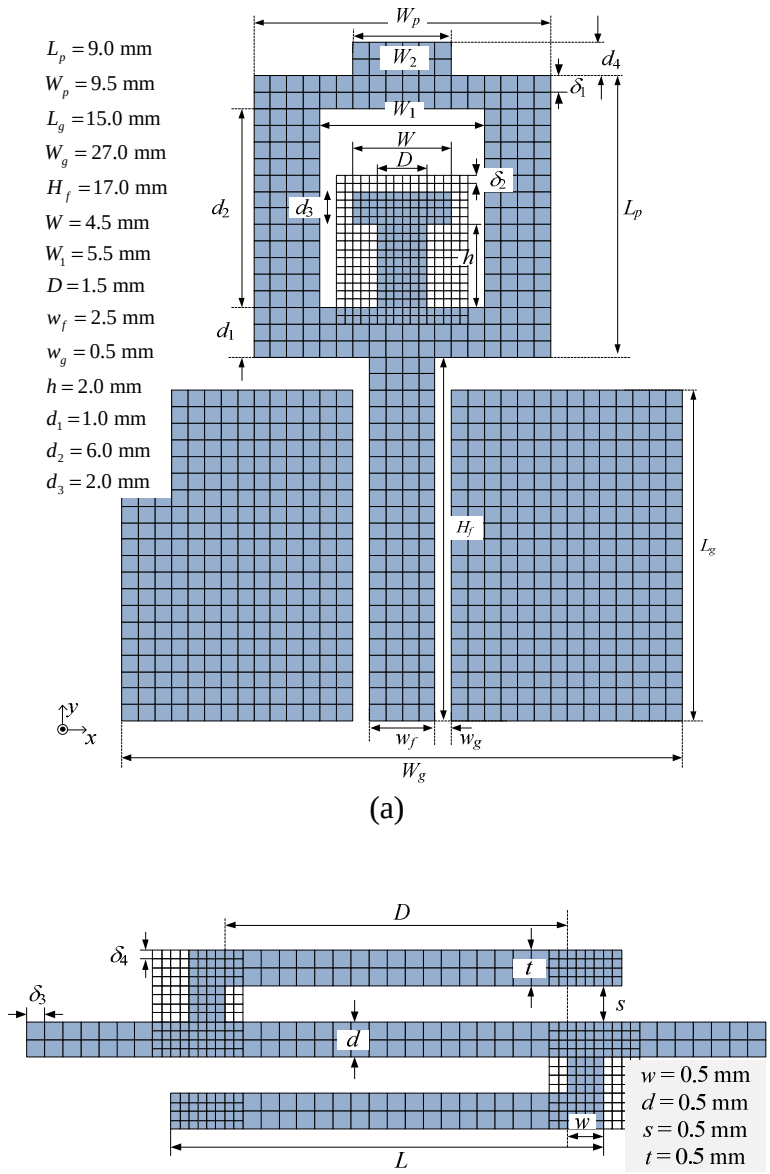

(a)

(b)

Fig. 3.1 Demonstration of the library structure and its sub-set structure: (a) printed slot antenna and (b) double-stub tuner. Dimensions are shown in the insets.

In Fig. 3.1 (b), a double-stub tuner, which is built on a substrate of $\varepsilon_r = 4.4$ and thickness of 0.8 mm, is presented. The two stubs of length *L* are symmetrically located on both sides of the microstrip line. The distance between the two stubs is *D*. The widths of the stubs and the microstrip line are t and w, respectively. The nominal design parameters are given in the figure inset.

Three types of regions are meshed with a fine grid of step size $\delta_4 = 0.125\ \text{mm}$: (i) the ends of the two stubs in order to perform the fine tuning of the stub length L; (ii) the regions where the vertical portion of the two stubs may change during the design iterations; and (iii) the regions where the stubs connect to the transmission line. The areas that do not evolve during optimization are discretized with square patches of step size $\delta_3 = 0.25\ \text{mm}$. The library structure is built and can be used in a similar way as the previous example.

To perform the derivative estimation in (3.8), $\boldsymbol{A}(p_n + \Delta p_n)$ and $\boldsymbol{A}(p_n - \Delta p_n)$ are needed. These are the system matrices of the perturbed planar structures where the *n*th parameter is perturbed in the forward and backward directions. All these structures are subsets of the library structure.

3.4 SENSITIVITY ANALYSIS VALIDATION

The *S*-parameter sensitivity analysis of an antenna and a double-stub tuner are presented. In order to illustrate the accuracy of the proposed approach with non-uniform MoM grid, the *S*-parameter derivatives are calculated with three approaches: (i) the proposed

sensitivity formula (3.13) using the central finite-difference (CFD) estimates of the system matrix derivatives (3.8) on a non-uniform MoM grid; (ii) the proposed formula (3.13) using a fine uniform MoM grid (the step sizes are δ_2 and δ_4 in the antenna and the tuner example, respectively); and (iii) *S*-parameter derivatives estimation with CFD at the response level using the same meshing as (ii). Note that MoM grid are used in the first and the second approaches in order to have consistent library structures that will be used in the design optimization examples in Section 3.5 where the computational effort comparison among the three approaches are illustrated.

The S_{11}-parameter sensitivity analysis with respect to h in the printed antenna is presented. The non-uniform mesh used in the first approach is shown in Fig. 3.1 (a) with a perturbation of $\delta_2 = 0.25\ \text{mm}$. In the second and third approaches, a fine uniform mesh is used with a step size of $\delta_2 = 0.25\ \text{mm}$. The derivatives $\partial|S_{11}|/\partial h$ are plotted against a frequency sweep from 3 GHz to 11 GHz in Fig. 3.2. The derivatives $\partial|S_{11}|/\partial h$ are also plotted against a sweep of the parameter h in Fig. 3.3. The three sensitivity curves are in good agreement.

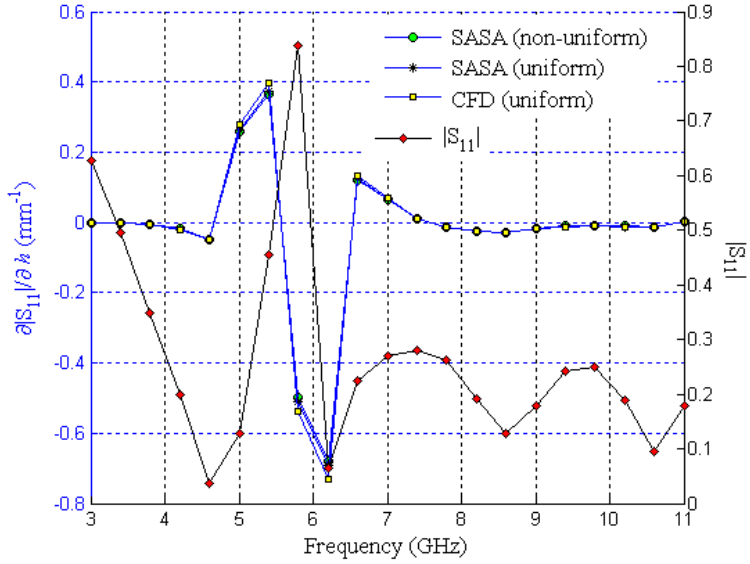

Fig. 3.2 $|S_{11}|$ and its derivatives with respect to h against frequency (h = 2.0 mm, W = 4.5 mm, and D = 1.5 mm). "SASA" stands for results with the proposed self-adjoint sensitivity analysis. "CFD" stands for results with central finite differences at the response level.

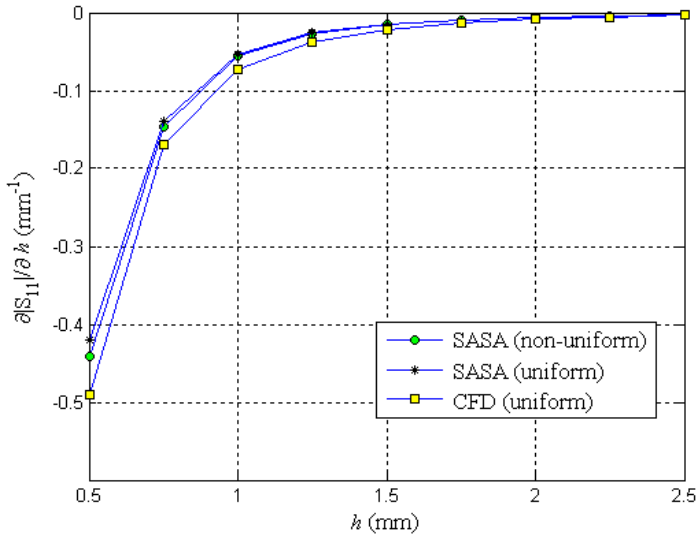

Fig. 3.3 $\partial|S_{11}|/\partial h$ plot against a sweep of h (W = 4.5 mm, D = 1.5 mm) at f = 4 GHz.

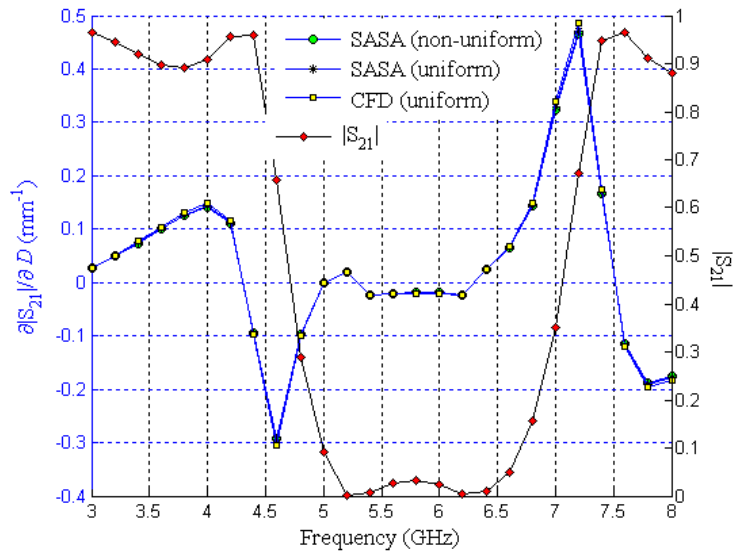

Fig. 3.4 $|S_{21}|$ and its derivatives with respect to D (D = 7.0 mm, L = 7.0 mm).

The S_{21}-parameter sensitivity analysis is carried out for the double-stub tuner shown in Fig. 3.1 (b). The derivatives of $|S_{21}|$ with respect to D for a frequency sweep from 3 GHz to 8 GHz are plotted in Fig. 3.4. The derivatives $\partial|S_{21}|/\partial D$ for a sweep of D are shown in Fig. 3.5. Again, good agreement is achieved among the three curves. We observe that the first approach requires the least computational effort due to the use of library matrix and self-adjoint sensitivity calculation. The efficiency comparison of the three approaches will be further discussed with design optimization examples in Section 3.5.

Note that the accuracy of the sensitivity computation is influenced by the size of the perturbed grid. As the grid size decreases the estimation of $\Delta \boldsymbol{A}/\Delta p_n$ tends to converge to its actual analytical value, which results in more accurate sensitivity analysis.

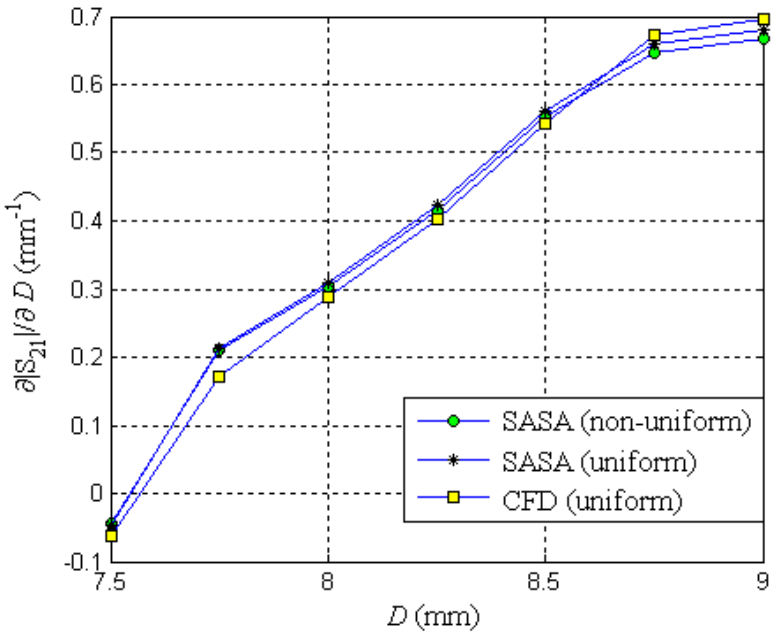

Fig. 3.5 Plot of the derivatives $\partial|S_{21}|/\partial D$ for a sweep of D (L = 7.0 mm) at f = 4.5 GHz.

3.5 DESIGN OPTIMIZATION EXAMPLES

Gradient-based optimizations of the S-parameters of the two structures introduced in Section 3.3 are performed. The Matlab function *fminimax* [6] is used for the optimization. It minimizes the worst-case (largest) value of a set of multivariable objective (or cost) functions, starting at an initial estimate. During the optimization, the design variables are updated iteratively by a line search algorithm [6], which requires the response Jacobian $(\nabla_p \boldsymbol{F})^T$ where $\boldsymbol{F}$ is the vector of objective functions to be minimized.

Three types of optimization are carried out in both examples. In type 1, the library structure with non-uniform MoM grid is used as shown in Fig. 3.1 (a). The S-parameter

derivatives are calculated with the proposed sensitivity formula (3.13) and using the CFD estimates of the system-matrix derivatives (3.8) on the non-uniform MoM grid. In type 2, the uniform fine-meshed library structure (the step sizes are δ_2 and δ_4 in the two examples, respectively) is used. The *S*-parameter derivatives are again calculated with (22). In type 3, no library structure or user-calculated derivative information are provided. The structure is discretized with fine uniform MoM grid (the same as type 2). The optimizer performs response-level finite-difference estimates to provide the sensitivity information.

3.5.1 Planar ultra-wide band (UWB) printed antenna

The goal is to design an UWB antenna as shown in Fig. 3.1 (a) with: i) impedance matched from 4 GHz to 10.5 GHz; ii) a rejection band from 5.4 GHz to 5.8 GHz with center frequency of 5.6 GHz. The objective function is defined as

$$\min \max \{F_1(f_m), F_2(f_0)\} \tag{3.17}$$

where

$$\begin{aligned} F_1(f_m) &= |S_{11}(f_m)| - 0.3, \quad \text{for } 4.0 \text{ GHz} \le f_m \le 5.0 \text{ GHz}, \\ &\qquad\qquad\qquad\qquad\quad 6.2 \text{ GHz} \le f_m \le 10.5 \text{ GHz}, \\ &\qquad\qquad\qquad\qquad\quad m = 1, \ldots, N_{f1}, \\ F_2(f_0) &= 0.9 - |S_{11}(f_0)|, \quad \text{for } f_0 = 5.6 \text{ GHz}. \end{aligned} \tag{3.18}$$

N_{f1} is the number of sampling frequency points in the given frequency range. The design variables are $\boldsymbol{p} = [h, W, D]^T$, with initial values $\boldsymbol{p}_0$ = [0.5, 1.5, 0.5]^T mm. The other parameters are fixed at the values given in Fig. 3.1 (a).

TABLE 3.1

COMPARISON OF THE THREE OPTIMIZATION PROCEDURES IN THE ANTENNA EXAMPLE.

	Type 1	Type 2	Type 3
number of iterations	8	8	14
calls for EM solver	37	37	124
system solving time (s)	37	185	620
matrix fill time (s)	1	3	124
total time (s)	38	188	744

The type 1 optimization converges after eight iterations with the objective function being equal to 0.2. The EM solver is called 37 times. The optimized design variables are $\boldsymbol{p}_1^* = [1.5, 2.5, 1.5]^T$ mm. The type 2 optimization converges to the same result as in the Type 1 optimization with the same number of iterations. However, its computational overhead is about five times higher because of the fine uniform mesh of the entire structure. The type 3 optimization converges after fourteen iterations with a value of the objective function 0.35. The optimized design is given by $\boldsymbol{p}_2^* = [1.5, 2.0, 1.5]^T$ mm. However, the EM solver is called 124 times. The efficiency comparison of the three approaches is shown in Table 3.1. The Type 1 optimization is the most efficient among all three optimization types. The Type 3 optimization requires the most computational effort. The evolution of the objective function versus the iteration of the three types of optimization is shown in Fig. 3.6.

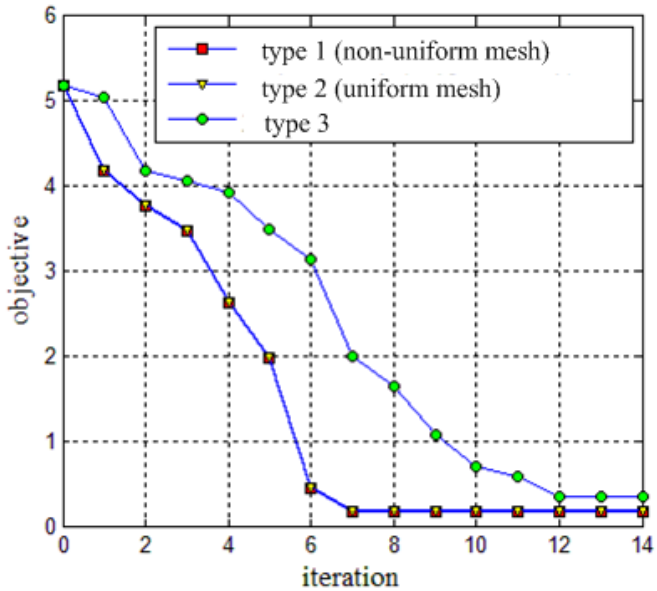

Fig. 3.6 Progress of the three optimization procedures in the printed antenna example.

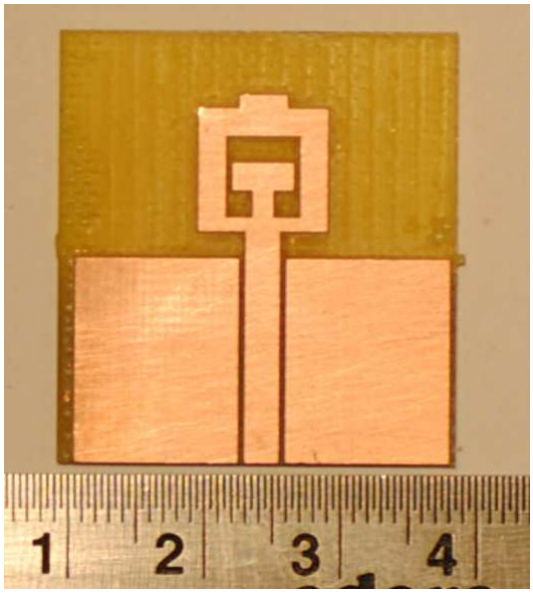

Fig. 3.7 Photo of the proposed antenna prototype.

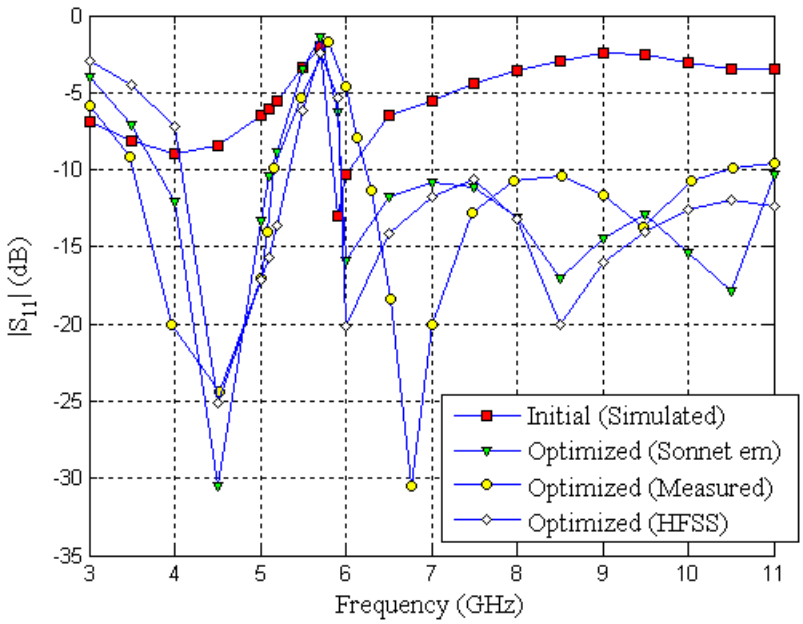

Fig. 3.8 $|S_{11}|$ plot of the initial and the optimized antenna designs.

An antenna is prototyped based on the parameters $\boldsymbol{p}_1$*. The photo of the prototype is shown in Fig 3.7. The measured as well as the simulated S_{11}-parameter of the optimized design (simulated by Sonnet ***em*** and HFSS) are presented in Fig. 3.8. For comparison, the S_{11}-parameter of the initial design is also shown. The measured and the simulated results show good agreement in the lower frequency band while there are some differences at higher frequencies. This may be due to the fact that the Subminiature Type A (SMA) connector and the coaxial cable are not modeled in the simulation.

3.5.2 Planar double-stub tuner

The goal is to design a double-stub tuner (shown in Fig. 3.1 (b)) with a stop band from 5 GHz to 6 GHz. The objective function is minimized using a minimax optimizer as:

$$\min \max \left\{ F_1(f_u^{(1)}), F_2(f_v^{(2)}) \right\} \tag{3.19}$$

where

$$
\begin{aligned}
&F_1(f_u^{(1)}) = \left|S_{21}(f_u^{(1)})\right| - 0.05, \text{ for 5 GHz } \le f_u^{(1)} \le \text{ 6 GHz,} \\
&F_2(f_v^{(2)}) = 0.9 - \left|S_{21}(f_v^{(2)})\right|, \text{ for 3 GHz } \le f_v^{(2)} \le \text{ 4GHz,} \\
&\qquad\qquad\qquad\qquad\qquad\qquad \text{7 GHz } \le f_v^{(2)} \le \text{ 8GHz,} \\
&\qquad\qquad\qquad\qquad\qquad\qquad u = 1,\ldots,N_{f2};\ v = 1,\ldots,N_{f3}.
\end{aligned}
\tag{3.20}
$$

Here, N_{f2} and N_{f3} are the numbers of sampling frequency points in the respective frequency ranges. The design variables are $\boldsymbol{p} = [L, D]^T$, with initial values $\boldsymbol{p}_0 = [9.0,\ 9.0]^T$ mm. The other parameters are fixed at the values given in Fig. 3.1 (b).

The Type 1 and Type 2 optimization procedures converge after five iterations with the objective functions being equal to 0.09. They achieve the same optimized design $\boldsymbol{p} = [7.5, 7.0]^T$ mm. The EM solver is called 21 times in both cases. The Type 2 optimization takes more computational time than the Type 1 optimization due to the computational load caused by the fine mesh. The Type 3 optimization converges after nine iterations, giving the same optimized design as the other two types. However, the EM solver is called 54 times. The comparison of the three approaches is shown in Table 3.2. Type 1 optimization requires the least overall computational time while Type 3 optimization requires the largest. The simulated S_{21}-parameters of the initial design and the optimized design are presented in Fig. 3.9 for comparison. The optimized design is simulated not only with Sonnet ***em*** but also with in HFSS.

TABLE 3.2

COMPARISON OF THE THREE OPTIMIZATION PROCEDURES IN THE STUB TUNER EXAMPLE.

	approach 1	approach 2	approach 3
number of iterations	5	5	9
calls for EM solver	21	21	54
system solving time (s)	10.5	42	108
matrix fill time (s)	1	2	108
total time (s)	11.5	44	216

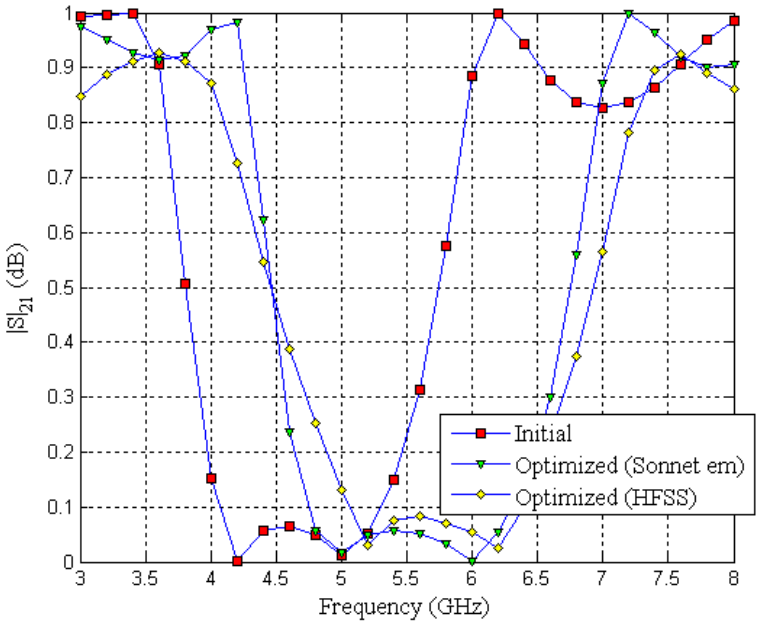

Fig. 3.9 $|S_{21}|$ plot of the initial and the optimized double-stub tuner design.

In summary, the proposed approach reduces the computational load in gradient-based optimization significantly. This is achieved due to three factors. (i) The mesh is

kept the same during the design optimization and the sensitivity analysis. Structural changes are achieved only by “metallization” and “de-metallization” of the patches in the library structure. Thus, re-meshing is avoided and the system matrices are obtained fast. (ii) There is no need to export the system matrices for every iteration because the library matrix is generated once at the beginning of the optimization. (iii) The computational resources are kept at a reasonable level during simulation due to the non-uniform mesh.

3.6 CONCLUSION

A self-adjoint approach using discrete perturbations on a non-uniform MoM grid is applied to the *S*-parameters sensitivity analysis of high-frequency structures and their design optimization. It provides fast matrix fills for optimization purposes and a computationally efficient way for calculating the sensitivity information. Results from the designs of an UWB antenna and a double-stub tuner validate the proposed method and its superior performance in reducing the computational effort.

REFERENCES

[1] E. A. Soliman, M. H. Bakr, and N. K. Nikolova, “Neural networks – method of moments (NN-MoM) technique for the efficient filling of the MoM coupling matrix,” *IEEE Trans. Antennas Propag.*, vol. 52, no. 6, pp. 1521–1529, June 2004.

[2] N. K. Nikolova, R. Safian, E. A. Soliman, M. H. Bakr, and J. W. Bandler, "Accelerated gradient based optimization using adjoint sensitivities," *IEEE Trans. Antennas Propag*., vol. 52, pp. 2147–2157, Aug. 2004.

[3] E. A. Soliman, M. H. Bakr, and N. K. Nikolova, "Accelerated gradient-based optimization of planar circuits," *IEEE Trans. Antennas Propag*., vol. 53, no. 2, pp. 880–883, Feb. 2005.

[4] N. K. Nikolova, J. Zhu, D. Li, M. H. Bakr and J. W. Bandler, "Sensitivity analysis of network parameters with electromagnetic frequency domain simulators," *IEEE Trans. Microwave Theory Tech*., vol. 54, pp. 670−677, Feb. 2006.

[5] Sonnet ***em***, Suites 12.52, Sonnet Software, Inc., USA, 2009.

[6] MATLAB (R2010a), The MathWorks, Inc., USA, 2010.

Chapter 4

SPATIAL RESOLUTION AND ROBUSTNESS TO NOISE OF THE SENSITIVITY-BASED IMAGING

4.1 INTRODUCTION

Image reconstruction with microwave responses is a promising methodology for noninvasive evaluation, testing, and diagnostics in medicine [1]-[7], nondestructive testing [8][9], geophysical prospecting, remote sensing and underground surveillance [10]-[13]. In microwave imaging, the ability of microwaves to penetrate optically opaque materials (e.g., tissue, soil, concrete, etc.) is being exploited. The goal is the reconstruction of the permittivity and/or conductivity distribution in the object under test (OUT).

Microwave imaging can be generally categorized into quantitative imaging and qualitative imaging in terms of the dielectric profile in the reconstructed image. In the former, the actual values of the permittivities and/or conductivities of the OUT are estimated and plotted to produce an image. In the latter, targets are identified in the image only as locations of scattering sources, the brightness of which is representative of the overall permittivity/conductivity differences between the background medium and the

target.

A microwave detection algorithm based on a response-sensitivity formulation has been proposed in [14]. It aims at qualitatively uncovering abnormalities in the OUT (e.g., structural flaws, cancerous tissue, or a hidden weapon) whose normal state (or background) is assumed known. Here, the normal state of the object is referred to as the reference object (RO). The RO need not be homogeneous. The technique yields an image of the contrast in the dielectric properties of the OUT and the RO. The method has been introduced in [14] has been validated with examples using electromagnetic (EM) simulations of circular-sensor array data acquisition.

The method's advantage is that it does not involve the inversion of a matrix and the computations are fast. The method, on the other hand, requires EM simulations of the RO, which includes the known reference medium and the known antennas. These simulations are performed off-line as part of the system calibration. Once the simulation of the RO is available, the self-adjoint formulation of the response-sensitivity calculation allows for real-time image reconstruction from the measured microwave responses of any OUT. Multiple ROs can also be used if necessary as this is not going to have significant impact on the time required to obtain an image.

The *spatial resolution*, i.e., the smallest detail that represents truthfully a detail in the imaged object [15], is an important measure of the performance of an imaging technique. It can be defined as the width at the half-power level of a very small but detectable single object's image, i.e., the width of the point-spread function (PSF) of the technique at the –3 dB level. If any two objects are closely spaced so that the distance

between them is smaller than the spatial resolution, they will appear as a single object in the image.

Until now, the resolution of the sensitivity-based imaging approach has not been studied and this is the focus of the current work. In particular, we consider two cases of common wideband data acquisition approaches: i) planar raster scanning where the transmission/reception (Tx/Rx) sensors scan over the object; and ii) tomographic acquisition where the Tx/Rx sensors are arranged in a circular array.

The resolution limit is first derived theoretically for both the planar and the circular acquisition cases and is then verified by imaging examples exploiting analytical EM models. In the evaluation of the method's spatial resolution, the RO and the OUT are modeled analytically, where the RO model provides the incident field while the OUT model provides the total field, which is the superposition of the incident and the scattered field. The respective responses are also calculated. The use of analytical EM models in this study eliminates possible ambiguities in the evaluation of the spatial resolution which may be encountered if numerical simulation models are used.

Finally, the effect of noise has not been studied before and yet the noise robustness is important for the method's implementation with realistic microwave measurements. We focus on this problems as well and relate it to the spatial and frequency sampling rates. A guideline is also provided for an acceptable signal-to-noise ratio (SNR) versus the spatial and frequency sampling rates in designing a data-acquisition system for the method.

4.2 CONFIGURATION OF THE DATA ACQUISITION SYSTEMS

There are two common data acquisition approaches in microwave imaging. The first approach utilizes scanning where usually one or two sensors perform a scan over acquisition surfaces (e.g., see [1],[4],[5],[16]). In the second approach, a fixed array of N_e sensors is used to sample the scattered field (e.g., see [6]). In both cases, the scattered field is usually sampled on canonical surfaces such as planes, cylinders or spheres, or portions of those. Also, the scattered field can be sampled at the location of the transmitter (monostatic case), at a location different from that of the transmitter (bistatic case) or at multiple locations (multistatic case).

4.2.1 Planar raster scanning

An example of the system configuration of an OUT together with a planar-raster scanning arrangement is shown in Fig 4.1. Two Tx/Rx sensors are placed along each other's boresight [17] on both sides of the object. These sensors together with the examined object form a two-port microwave network whose *S*-parameters are measured at the desired frequencies. The two sensors are scanned simultaneously over the two *z* = *const* planes. The data acquisition is performed in both the OUT and the RO to provide the required responses: $S^{(m)}_{\mathrm{OUT},jk}(x,y,z_j)$ and $S^{(m)}_{\mathrm{RO},jk}(x,y,z_j)$ ($j,k=1,2$). Here, (x,y,z_j) denotes the location where the *S*-parameters are sampled: sensor #1 is located at $(x,y,-D/2)$, i.e., $z_1=-D/2$; sensor #2 is located at $(x,y,D/2)$, i.e., $z_2=D/2$. Also, $m = 1,\ldots, N_f$, where N_f is the number of frequency samples.

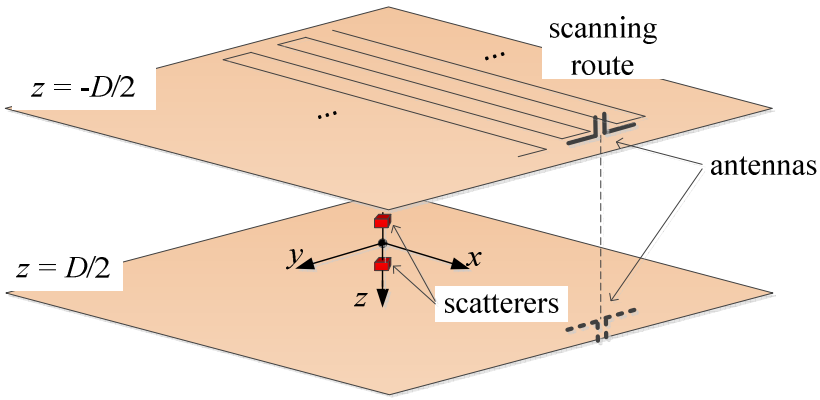

Fig. 4.1 Configuration of the raster scanning setup in an example involving two small scatterers. The two scanning planes are located at $z = -D/2$ and $z = D/2$.

We refer to the *z*-direction as the *range direction* and the resolution in this direction is referred to as the *range resolution*. Similarly, we refer to the *x*-direction as the *cross-range direction*, and the respective resolution is referred to as the *cross-range resolution*. The *y*-direction is also a cross-range direction and its resolution is identical to that in the *x*-direction, provided that the aperture size and the sampling rate are the same as those in the *x*-direction.

It should be emphasized that the two sensors are always placed along each other's boresight (along *z*) in our study. This is because our focus is on the imaging of very lossy objects such as tissue. The signal attenuation in tissue is very high and the signal-to-noise ratio (SNR) for signals propagating away from the boresight is usually low. The boresight alignment of the sensors can provide the shortest path for the signals and, therefore, results in the strongest signal level.

Raster-scan data acquisition is not limited to two-antenna systems (as shown in

Fig. 4.1). Antenna arrays can also be used to acquire data. Such systems can provide more responses and their resolution is expected to be better than the two-sensor scenario studied here. The current study is thus representative of the limitations in the worst-case scenario as far as the sensors number is concerned.

At every measurement (shown in Fig. 4.1), one sensor transmits, e.g., the transmitter at $\boldsymbol{r}_k = (x, y, z_k)$, $k = 1, 2$, and both sensors receive, i.e., the receivers at $\boldsymbol{r}_j = (x, y, z_j)$, $j = 1, 2$. The above acquisition is performed at every frequency f_m ($m = 1, ..., N_\mathrm{f}$). Note that for a small dipole acting as receiving antenna, the response at the receiver location $\boldsymbol{r}_j$ due to the transmitter at $\boldsymbol{r}_k$ is calculated as

$$S_{jk}^{(m)}(x, y, z_j) \equiv \hat{\boldsymbol{\rho}}_j \cdot \mathbf{E}_{jk}^{(m)}(x, y, z_j) \tag{4.1}$$

where $\hat{\boldsymbol{\rho}}_j$ is the antenna polarization vector and $\mathbf{E}_{jk}^{(m)}(x, y, z_j)$ is the **E**-field at $\boldsymbol{r}_j$ when the transmitter at $\boldsymbol{r}_k$ radiates. The expression in (4.1) holds for both the RO and the OUT measurements; this is why the respective subscripts (RO and OUT) are omitted in both the **E**-field and the *S*-parameters.

In the planar acquisition described in Fig. 4.1, the acquisition coordinates z_j ($j = 1, 2$) are constant and defined by $z_1 = -D/2$ and $z_2 = D/2$. Hereafter, in the raster scanning scenario, the coordinate z_j is omitted from the arguments of the responses $S_{jk}^{(m)}$ for short notations as its value is implied by the subscript *j*.

In our examples, the background medium is assumed to be vacuum. In the double-scatterer imaging examples presented later, two voxel-size scatterers are placed around

the origin along the range direction or along the cross-range direction (refer to Fig. 4.1 for the range-alignment example). In the single-scatterer example, the OUT model setup is the same except that there is only one voxel-size scatterer positioned at the origin. The antennas are assumed to be oriented along *y*. The distance between the two sensors is D. The computational cell size is δ and it defines the voxel volume δ^3. We set the scanning steps along the *x*- and *y*- directions to be the same, i.e., $\Delta x = \Delta y = \Delta h$.

Wideband data are used in the image reconstruction. Note that data acquisition in an ultra-wide band (UWB) is preferred in the imaging of human tissues due to the following advantages. First, the inversion is more robust to noise since frequency-dependent image artifacts are likely to cancel. Second, at low frequencies, the signal penetrates better and results in better signal-to-noise ratio. At high frequencies, the image spatial resolution is better due to the shorter wavelengths. Thus, employing UWB responses allows for taking advantage of both, good penetration and better resolution.

Note that the **E**-field distribution in the OUT is the superposition of the *incident field* $\mathbf{E}_{\mathrm{RO}}^{(m)}$ and the *scattered field* $\mathbf{E}_{\mathrm{sc}}^{(m)}$. The field computation is discussed in Section 4.5.

4.2.2 Circular array for tomographic acquisition

The configuration of an OUT with the circular sensor array is shown in Fig. 4.2. N_{e} Tx/Rx sensors are distributed uniformly along a circle. In 3D tomographic imaging, the scattered signals are acquired by the array in a given plane and processed to produce a 2D image in this plane after which the array is moved to the next vertical position. Such

tomographic data acquisition results in a vertical stack of 2D images which represent the 3D OUT.

The sensors together with the examined object form an N_e-port microwave network whose S-parameters are measured at the desired frequencies. Similarly to (4.1), when the receiving antennas are small dipoles the S-parameters are calculated as

$$S_{jk}^{(m)} = \hat{\boldsymbol{\rho}}_j \cdot \mathbf{E}_{jk}^{(m)}. \tag{4.2}$$

The **E**-field and the S-parameters are functions of the location (x_j, y_j, z_j) of the j-th receiver. However, the variable (x_j, y_j, z_j) is omitted since it is implied by the subscript j in the S-parameter notation.

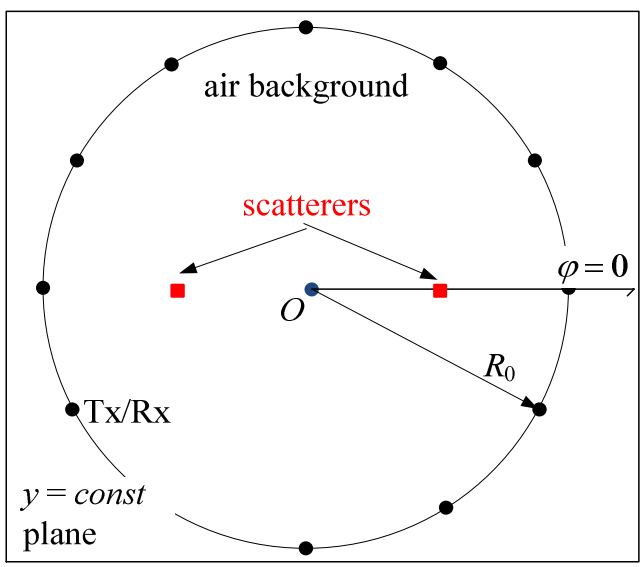

Fig. 4.2 Configuration of the circular-sensor array acquisition setup in an OUT example involving two small scatterers. The black dots indicate the Tx/Rx antennas.

At every measurement, one sensor transmits (e.g., the transmitter at $\boldsymbol{r}_k$) and all sensors receive (the receivers at $\boldsymbol{r}_j$, j = 1,…, N_e). The above acquisition is repeated for every transmitter at $\boldsymbol{r}_k$ (k = 1,…, N_e). A total number of N_e^2 responses are thus measured at every frequency f_m ($m = 1,...,N_f$) for every vertical (y = *const*) acquisition level.

An example of the OUT model is shown in Fig. 4.2. The background medium is vacuum. In the example shown in the figure, two voxel-size scatterers are located in the plane of the sensor array. The computational cell size is δ, and it defines the voxel volume δ^3. The antennas are vertically oriented dipoles. Again, UWB responses are used.

4.2.3 Reference Objects (RO)

The choice of RO in the sensitivity-based method depends on the application. Typically, the RO would mimic as closely as possible the background (target-free) medium and would include an accurate representation of the antennas. In this analytical study, the RO is the same as the OUT except that there is no scatterer embedded. The RO is used to obtain the following information which is needed by the imaging method:

- $\mathbf{E}_{\mathrm{RO}}^{(m)}(\boldsymbol{r}')$: the (normalized) incident field distribution at $\boldsymbol{r}'$;
- $S_{\mathrm{RO},jk}^{(m)}(\boldsymbol{r}_j)$: the responses in the RO acquired with the receiver at $\boldsymbol{r}_j = (x_j, y_j, z_j)$ when the k-th antenna transmits;
- the derivatives of the RO responses with respect to the complex relative permittivity $\tilde{\varepsilon}_{\mathrm{RO,r}}^{(m)}(\boldsymbol{r}')$ in the RO.

Here, $m = 1, \ldots, N_{\mathrm{f}}$; j, k = 1, 2 in the raster scanning example and j, k = 1,… N_{e} in the circular array example. Note that $\mathbf{E}_{\mathrm{RO}}^{(m)}(\boldsymbol{r}')$ is usually obtained using simulations. It could also be acquired with measurements using field probes if the RO medium is mechanically penetrable. Here, it is obtained from analytical models.

With the above data, the Fréchet derivatives in the RO are computed and plotted versus the coordinates of the voxels in the imaged region $\boldsymbol{r}'$. The obtained images are referred to as *Jacobian maps*. Note that in the tomographic circular array approach, 2D maps are obtained in each vertical plane where measurements are taken. In principle, the Jacobian maps can be generated in planes different from that of the sensor array. However, in this case, the signals may be weak and the images may be unreliable. Therefore, the Jacobian map is typically generated in the plane of the sensor array and it is obtained from the signals acquired in this plane only. The scattering by targets in this plane is usually strong, which results in high-fidelity images. In the planar raster scanning approach, 3D Jacobian maps are obtained directly.

4.3 RESPONSE-DIFFERENCE FUNCTION AND ITS DERIVATIVES

To reconstruct the image using the algorithm presented in [14], the following information is needed: (i) the responses measured in the RO; (ii) the **E**-field distribution in the RO under the known excitations (usually obtained via simulation); and (iii) the responses measured in the OUT where abnormalities may exist. The differences in the responses

acquired with the RO and the OUT are used to form a least-square response-difference function. The derivatives of the RO responses with respect to the complex relative permittivity of each voxel in the RO are computed using the self-adjoint sensitivity analysis (SASA) method [18]. The derivatives of the response-difference function are then computed using the RO response derivatives. These derivatives are then used to generate permittivity Jacobian maps, i.e., maps of the Fréchet derivatives. These maps represent the property difference between the RO and the OUT. Abnormalities are thus identified and localized by significant parameter differences (peaks and dips) in the image.

The response-difference function is defined as the difference between the complex responses acquired with the OUT and those acquired with the RO. In the planar raster scanning approach, it can be written as [18]

$$F^{(m)}\left(\tilde{\varepsilon}_{\mathrm{RO,\,r}}^{(m)}(\boldsymbol{r}')\right)=\frac{1}{2N_xN_y}\sum_{u=1}^{N_y}\sum_{v=1}^{N_x}\sum_{j,k=1}^{2}\left|\Delta S_{jk}^{(m)}\left(\boldsymbol{\rho}(u,v)\right)\right|^2 \tag{4.3}$$

where

$$\Delta S_{jk}^{(m)}\left(\boldsymbol{\rho}(u,v)\right)=S_{\mathrm{RO},\,jk}^{(m)}\left(\boldsymbol{\rho}(u,v)\right)-S_{\mathrm{OUT},\,jk}^{(m)}\left(\boldsymbol{\rho}(u,v)\right) \tag{4.4}$$

and $\boldsymbol{\rho}(u,v)=(x_u,y_v)$ with $x_u=X_0+\Delta x\cdot(u-1)$ and $y_v=Y_0+\Delta y\cdot(v-1)$. Here, Δx and Δy are the sampling intervals along x and y, respectively. The scan starts at position (X_0,Y_0). In (4.3), $S_{\mathrm{OUT},\,jk}^{(m)}$ and $S_{\mathrm{RO},\,jk}^{(m)}$ are the S-parameters acquired with the OUT and the RO, respectively. We denote $\tilde{\varepsilon}_{\mathrm{RO,\,r}}^{(m)}(\boldsymbol{r}')$ = $\varepsilon_{\mathrm{RO,\,r}}^{(m)}(\boldsymbol{r}')-\mathrm{i}\sigma_{\mathrm{RO}}^{(m)}(\boldsymbol{r}')/(2\pi f_m\varepsilon_0)$ as the complex relative permittivity distribution in the RO at the m-th frequency. Here, $\varepsilon_{\mathrm{RO,\,r}}^{(m)}(\boldsymbol{r}')$ is the

voxel relative permittivity, $\sigma_{\mathrm{RO}}^{(m)}(\boldsymbol{r}')$ is its conductivity, ε_0 is the permittivity of vacuum, and $\boldsymbol{r}'$ is the voxel location in the imaged region.

Note that the response-difference functions $F^{(m)}$ depend implicitly on the value of $\tilde{\varepsilon}_{\mathrm{RO,\,r}}^{(m)}(\boldsymbol{r}')$ through the field distribution in the RO. Also, both $S_{\mathrm{RO},\,jk}^{(m)}$ and $S_{\mathrm{OUT},\,jk}^{(m)}$ are functions of their respective complex relative permittivities. Here, $\tilde{\varepsilon}_{\mathrm{RO,\,r}}^{(m)}(\boldsymbol{r}')$ is the parameter of interest in the RO in which the derivative is calculated. Therefore, the derivatives of (4.3) with respect to the relative permittivities and the conductivities are:

$$\begin{aligned} D_p^{(m)}(\boldsymbol{r}')\Big|_{p=\varepsilon_{\mathrm{r}},\sigma} &= \frac{\partial F^{(m)}}{\partial p_{\mathrm{RO}}^{(m)}(\boldsymbol{r}')} \\ &= \frac{1}{N_x N_y}\sum_{u=1}^{N_y}\sum_{v=1}^{N_x}\sum_{j,k=1}^{2}\mathrm{Re}\left\{\left[\Delta S_{jk}^{(m)}\left(\boldsymbol{\rho}(u,v)\right)\right]^{*}\cdot\frac{\partial S_{\mathrm{RO},\,jk}^{(m)}\left(\boldsymbol{\rho}(u,v)\right)}{\partial p_{\mathrm{RO}}^{(m)}(\boldsymbol{r}')}\right\} \end{aligned} \tag{4.5}$$

where [14]

$$\frac{\partial S_{\mathrm{RO},\,jk}^{(m)}\left(\boldsymbol{\rho}(u,v)\right)}{\partial p_{\mathrm{RO}}^{(m)}(\boldsymbol{r}')} = \left(-\mathrm{i}\right)^{n}\left(2\pi f_m \varepsilon_0\right)^{2-n}\frac{\Delta\Omega(\boldsymbol{r}')}{J^{(m)}(\boldsymbol{r}_k)\Delta\Omega(\boldsymbol{r}_k)}\left[\mathbf{E}_{\mathrm{RO},\,j}^{(m)}(\boldsymbol{r}')\cdot\mathbf{E}_{\mathrm{RO},\,k}^{(m)}(\boldsymbol{r}')\right]_{\boldsymbol{\rho}(u,v)} \tag{4.6}$$

with

$$n = \begin{cases} 1 & \text{when } p_{\mathrm{RO}}^{(m)} = \varepsilon_{\mathrm{RO,r}}^{(m)}, \\ 2 & \text{when } p_{\mathrm{RO}}^{(m)} = \sigma_{\mathrm{RO}}^{(m)}. \end{cases} \tag{4.7}$$

Here, (4.6) represents the derivatives of the RO responses $S_{\mathrm{RO},\,jk}^{(m)}$ acquired at (x_u, y_v, z_j), j = 1, 2, with respect to the permittivities/conductivities of the RO at $\boldsymbol{r}'$. In (4.6), $\mathbf{E}_{\mathrm{RO},\,k}^{(m)}(\boldsymbol{r}')$ ($k=1,2$) is the incident **E**-field at $\boldsymbol{r}'$ when the transmitter is at $\boldsymbol{r}_k = (x_u, y_v, z_k)$, $k=1,2$, in the RO model. $\Delta\Omega(\boldsymbol{r}')$ is the volume of the voxel located at $\boldsymbol{r}'$; $\Delta\Omega(\boldsymbol{r}_k)$ is the volume of the voxel where the current-density excitation $J^{(m)}(\boldsymbol{r}_k)$ is

located; $J^{(m)}(\boldsymbol{r}_k)$ is the current-density value at the k-th transmitting dipole. Hereafter, $J^{(m)}(\boldsymbol{r}_k)$ is set to $J^{(m)}(\boldsymbol{r}_k) = J_0$ for all transmitters at all frequencies. Also, uniform volume discretization is assumed, which leads to $\Delta\Omega(\boldsymbol{r}_k) = \Delta\Omega(\boldsymbol{r}') = \Omega$. Note that the current-density excitation is a vector defined by $\boldsymbol{J}^{(m)}(\boldsymbol{r}_k) = J_0\hat{\boldsymbol{\rho}}_k$, where $\hat{\boldsymbol{\rho}}_k$ is the transmitting antenna polarization vector.

In the circular array acquisition, the response-difference function is defined similarly as

$$F^{(m)}\left(\tilde{\varepsilon}(\boldsymbol{r}')\right) = \frac{1}{2N_{\mathrm{e}}^{\,2}} \sum_{j=1}^{N_{\mathrm{e}}} \sum_{k=1}^{N_{\mathrm{e}}} \left| S_{\mathrm{RO},jk}^{(m)} - S_{\mathrm{OUT},jk}^{(m)} \right|^2, \quad m = 1, \ldots, N_{\mathrm{f}}. \tag{4.8}$$

Similar to the raster scanning approach, in the circular array acquisition, the derivatives of $F^{(m)}\left(\tilde{\varepsilon}(\boldsymbol{r}')\right)$ with respect to the relative permittivities and the conductivities are obtained as:

$$D_p^{(m)}(\boldsymbol{r}')\Big|_{p=\varepsilon_{\mathrm{r}},\sigma} = \frac{1}{N_{\mathrm{e}}^{\,2}} \sum_{j=1}^{N_{\mathrm{e}}} \sum_{k=1}^{N_{\mathrm{e}}} \mathrm{Re}\left[\left(\Delta S_{jk}^{(m)}\right)^* \frac{\partial S_{\mathrm{RO},jk}^{(m)}}{\partial p_{\mathrm{RO}}^{(m)}(\boldsymbol{r}')} \right]. \tag{4.9}$$

Here, $\partial S_{\mathrm{RO},jk}^{(m)} \big/ \partial p_{\mathrm{RO}}^{(m)}(\boldsymbol{r}')$ is computed using (4.6).

The derivatives in (4.5) and (4.9) are the Fréchet derivatives of the respective response-difference functions (4.3) or (4.8). They can be plotted versus the coordinates of the voxels $\boldsymbol{r}'$ in the imaged region. The image reconstruction is performed using (4.5) and (4.9), in the case of planar raster scanning and circular-sensor array data acquisition, respectively.

4.4 IMAGE FORMATION PROCEDURE

In order to form an image, the following image formation procedure is applied in the case of planar raster scanning.

Step **1** is <u>map generation</u>. The Jacobian map in (4.5) at each sampled frequency f_m ($m = 1,\ldots,N_{\mathrm{f}}$) is computed as a function of the voxel location $\boldsymbol{r}'$.

Here, we re-write (4.5) as

$$D_p^{(m)}(\boldsymbol{r}')\Big|_{p=\varepsilon_{\mathrm{r}},\sigma} = \frac{c^{(m)}}{N_x N_y} \sum_{u=1}^{N_y}\sum_{v=1}^{N_x}\sum_{j,k=1}^{2} \mathrm{Re}\left\{\left[\Delta S_{jk}^{(m)}\left(\boldsymbol{\rho}(u,v)\right)\right]^* \cdot P_p^{(m)}(\boldsymbol{r}')\right\} \tag{4.10}$$

where

$$c^{(m)} = \left(2\pi f_m \varepsilon_0\right)^{2-n} J_0^{-1} \tag{4.11}$$

and

$$P_p^{(m)}(\boldsymbol{r}')\Big|_{p=\varepsilon_{\mathrm{r}},\sigma} = \left(-\mathrm{i}\right)^n \left[\mathbf{E}_{\mathrm{RO},j}^{(m)}(\boldsymbol{r}') \cdot \mathbf{E}_{\mathrm{RO},k}^{(m)}(\boldsymbol{r}')\right]_{\boldsymbol{\rho}(u,v)}\Bigg|_{\substack{n=1,\ \text{when } p=\varepsilon_{\mathrm{r}} \\ n=2,\ \text{when } p=\sigma}} . \tag{4.12}$$

Step **2** is <u>map normalization</u>. Maps $D_p^{(m)}(\boldsymbol{r}')$ at each frequency are normalized using energy normalization [14]:

$$\bar{D}_p^{(m)}(x,y,z)\Big|_{p=\varepsilon_{\mathrm{r}},\sigma} = N(D_p^{(m)}) = \frac{D_p^{(m)}(x,y,z)}{\sqrt{\sum_{a=1}^{N_x}\sum_{b=1}^{N_y}\sum_{c=1}^{N_z}\left|D_p^{(m)}(x_a,y_b,z_c)\right|^2}} . \tag{4.13}$$

Two types of maps are obtained in this step. We refer to $\bar{D}_{\varepsilon_{\mathrm{r}}}(\boldsymbol{r}')$ as *normalized permittivity map* and to $\bar{D}_{\sigma}(\boldsymbol{r}')$ as *normalized conductivity map*. The images represent the permittivity/effective-conductivity differences between the RO and the OUT at f_m.

To combine all normalized Jacobian maps, the following steps are performed.

Step **3** is <u>normalized Jacobian map averaging</u>. The maps obtained in step 2 at all sampled frequencies are summed and averaged to form the *averaged frequency Jacobian map*:

$$M_p(\boldsymbol{r}')\Big|_{p=\varepsilon_\mathrm{r},\sigma} = \frac{1}{N_\mathrm{f}}\sum_{m=1}^{N_\mathrm{f}} \bar{D}_p^{(m)}(\boldsymbol{r}'). \tag{4.14}$$

Step **4** is <u>image formatting</u>. The averaged frequency Jacobian map can be normalized with respect to its maximum:

$$\bar{M}_{p,\mathrm{lin}}(\boldsymbol{r}')\Big|_{p=\varepsilon_\mathrm{r},\sigma} = \frac{\left|M_p(\boldsymbol{r}')\right|}{\left|M_p(\boldsymbol{r}')\right|_\mathrm{max}} \tag{4.15}$$

where $\left|M_p(\boldsymbol{r}')\right|_\mathrm{max}$ is the maximum value of $\left|M_p(\boldsymbol{r}')\right|$. The linear-scale map $\bar{M}_{p,\mathrm{lin}}(\boldsymbol{r}')$ can be plotted as is or it can be plotted in a logarithmic scale:

$$M_{p,\mathrm{dB}} = 10\log_{10}\bar{M}_{p,\mathrm{lin}}(\boldsymbol{r}'). \tag{4.16}$$

Note that the two types of maps $M_p(\boldsymbol{r}')$ obtained in step 3 can also be selected and combined as presented in [14] to form a final coherent diagnostic map. However, this is not the focus here because the obtained images are based on $M_{\varepsilon_\mathrm{r}}(\boldsymbol{r}')$. The imaging using $M_\sigma(\boldsymbol{r}')$ is analogous.

The imaging procedure for the case of circular array data acquisition can be obtained following a similar procedure. Here, we only provide the final result for the averaged frequency map:

$$M_p(\boldsymbol{r}')\Big|_{p=\varepsilon_\mathrm{r},\sigma} = \frac{1}{N_\mathrm{f}}\sum_{m=1}^{N_\mathrm{f}} \bar{D}_p^{(m)}(\boldsymbol{r}') = \frac{1}{N_\mathrm{f}}\sum_{m=1}^{N_\mathrm{f}} N\left(D_p^{(m)}(\boldsymbol{r}')\right). \tag{4.17}$$

Here,

$$D_p^{(m)}(\boldsymbol{r}') = \frac{c^{(m)}}{N_{\mathrm{e}}^2} \sum_{j=1}^{N_{\mathrm{e}}} \sum_{k=1}^{N_{\mathrm{e}}} \mathrm{Re}\left[\left(\Delta S_{jk}^{(m)} \right)^* P_p^{(m)}(\boldsymbol{r}') \right] \tag{4.18}$$

where $c^{(m)}$ is calculated using (4.11) and $P_p^{(m)}(\boldsymbol{r}')$ is calculated analogously to (4.12).

4.5 ANALYTICAL MODELS OF THE INCIDENT AND SCATTERED FIELD

The fundamental spatial resolution is obtained by considering the scattering from a very small (voxel-size) but detectable scatterer. Here, the background medium (i.e., the reference object) is set to be vacuum. The transmitters are assumed to be infinitesimal dipoles, which closely approximate an EM point source (or current element). Thus, the incident field can be calculated using known analytical expressions [19].

The same infinitesimal dipole is used as a receiver, which closely approximates point-wise field sampling as described by (4.1). This is in contrast to the larger aperture antennas (e.g., horn antennas) where the antenna interacts with the field in a large volume in a much more complex manner. Thus, the choice of small dipoles used as sensors enables the analytical calculation of the scatterering parameters.

4.5.1 Incident field

The transmitting antenna is modeled by a current element oriented along the *y* axis (see Fig. 4.1 and 4.2). Thus, in our expression, the planes defined by θ and ϕ are the

elevation and the azimuth planes with respect to the y axis. The incident **E**-field, observed at location $\boldsymbol{r}'$ due to a single dipole radiating at $\boldsymbol{r}_k$ is [19]:

$$\mathbf{E}_{\mathrm{RO},\,k}^{(m)}(\boldsymbol{r}') = \begin{pmatrix} E_x(\boldsymbol{r}') \\ E_y(\boldsymbol{r}') \\ E_z(\boldsymbol{r}') \end{pmatrix}_{\boldsymbol{r}_k} = \begin{pmatrix} \sin\theta\cos\phi & \sin\theta\sin\phi & \cos\theta \\ \cos\theta\cos\phi & \cos\theta\sin\phi & -\sin\theta \\ -\sin\phi & \cos\phi & 0 \end{pmatrix}^{-1} \begin{pmatrix} E_r(\boldsymbol{r}') \\ E_\theta(\boldsymbol{r}') \\ E_\phi(\boldsymbol{r}') \end{pmatrix}_{\boldsymbol{r}_k} \tag{4.19}$$

where

$$\begin{aligned} E_r(\boldsymbol{r}')\big|_{\boldsymbol{r}_k} &= \frac{I_0\eta L\cos\theta}{2\pi d^2(\boldsymbol{r}',\boldsymbol{r}_k)}\left[1+\mathrm{i}\frac{1}{k_{0,m}d(\boldsymbol{r}',\boldsymbol{r}_k)}\right]e^{-jk_{0,m}d(\boldsymbol{r}',\boldsymbol{r}_k)}, \\ E_\theta(\boldsymbol{r}')\big|_{\boldsymbol{r}_k} &= \frac{\mathrm{i}I_0\eta L k_{0,m}\sin\theta}{4\pi d(\boldsymbol{r}',\boldsymbol{r}_k)}\cdot \\ &\qquad \left[1+\mathrm{i}\frac{1}{k_{0,m}d(\boldsymbol{r}',\boldsymbol{r}_k)}-\frac{1}{k_{0,m}^2 d^2(\boldsymbol{r}',\boldsymbol{r}_k)}\right]e^{-jk_{0,m}d(\boldsymbol{r}',\boldsymbol{r}_k)}, \\ E_\phi(\boldsymbol{r}')\big|_{\boldsymbol{r}_k} &= 0, \end{aligned} \tag{4.20}$$

and

$$\begin{aligned} \sin\theta &= \frac{\sqrt{(x'-x_k)^2+(z'-z_k)^2}}{\sqrt{(x'-x_k)^2+(y'-y_k)^2+(z'-z_k)^2}}, \\ \cos\theta &= \frac{y'-y_k}{\sqrt{(x'-x_k)^2+(y'-y_k)^2+(z'-z_k)^2}}, \\ \sin\phi &= \frac{x'-x_k}{\sqrt{(x'-x_k)^2+(z'-z_k)^2}}, \\ \cos\phi &= \frac{z'-z_k}{\sqrt{(x'-x_k)^2+(z'-z_k)^2}}. \end{aligned} \tag{4.21}$$

Here, $d(\boldsymbol{r}',\boldsymbol{r}_k)$ is the distance between the observation point at $\boldsymbol{r}'$ and the center of the dipole at $\boldsymbol{r}_k$, i.e., $d(\boldsymbol{r}',\boldsymbol{r}_k)=|\boldsymbol{r}'-\boldsymbol{r}_k|$, $\boldsymbol{r}'=(x',y',z')$ and $\boldsymbol{r}_\xi=(x_k,y_k,z_k)$. The length of the dipole is $L=\delta$. I_0 is the current magnitude at the dipole's feed point and it relates to the current density J_0 in (4.6) as $I_0=\delta^2 J_0$. Also, η is the wave impedance of the vacuum

and $k_{0,m} = 2\pi f_m \sqrt{\mu_0 \varepsilon_0}$ is the wave number in the RO, where μ_0 is the permeability of the vacuum.

4.5.2 Scattered field

In the OUT, the total **E**-field (observed at $\boldsymbol{r}'$ when the transmitter is at $\boldsymbol{r}_k$) is the superposition of the incident field $\mathbf{E}^{(m)}_{\mathrm{RO},\,k}(\boldsymbol{r}')$ and the scattered field $\mathbf{E}^{(m)}_{\mathrm{sc},\,k}(\boldsymbol{r}')$:

$$\mathbf{E}^{(m)}_{\mathrm{OUT},\,k}(\boldsymbol{r}') = \mathbf{E}^{(m)}_{\mathrm{sc},\,k}(\boldsymbol{r}') + \mathbf{E}^{(m)}_{\mathrm{RO},\,k}(\boldsymbol{r}'), \qquad k = 1, 2. \tag{4.22}$$

The response of the OUT is observed at $\boldsymbol{r}' = \boldsymbol{r}_j$, $j = 1, 2$:

$$S^{(m)}_{\mathrm{OUT},\,jk}(\boldsymbol{r}_j) = \hat{\boldsymbol{\rho}}_j \cdot \mathbf{E}^{(m)}_{\mathrm{OUT},\,k}(\boldsymbol{r}_j) = \hat{\boldsymbol{\rho}}_j \cdot \left[\mathbf{E}^{(m)}_{\mathrm{sc},\,k}(\boldsymbol{r}_j) + \mathbf{E}^{(m)}_{\mathrm{RO},\,k}(\boldsymbol{r}_j)\right]. \tag{4.23}$$

Analogously, the response of the RO at the same location is

$$S^{(m)}_{\mathrm{RO},\,jk}(\boldsymbol{r}_j) = \hat{\boldsymbol{\rho}}_j \cdot \mathbf{E}^{(m)}_{\mathrm{RO},\,k}(\boldsymbol{r}_j). \tag{4.24}$$

Using the linear Born approximation [20], the scattered field when the k-th antenna transmits is calculated as:

$$\mathbf{E}^{(m)}_{\mathrm{sc},\,k}(\boldsymbol{r}') \approx \iiint_{\Omega_{\mathrm{OUT}}} k^2_{0,m}(\boldsymbol{r}'')\Delta\tilde{\varepsilon}^{(m)}(\boldsymbol{r}'')\underline{\boldsymbol{G}}^{(m)}(\boldsymbol{r}', \boldsymbol{r}'')\mathbf{E}^{(m)}_{\mathrm{RO},\,k}(\boldsymbol{r}'')\mathrm{d}\Omega, \; k = 1, 2 \tag{4.25}$$

where

$$\Delta\tilde{\varepsilon}^{(m)}_{\mathrm{r}}(\boldsymbol{r}'') = \tilde{\varepsilon}^{(m)}_{\mathrm{OUT,\,r}}(\boldsymbol{r}'') - \tilde{\varepsilon}^{(m)}_{\mathrm{RO,\,r}}(\boldsymbol{r}'')\,. \tag{4.26}$$

Here, Ω_{OUT} is the volume and $\boldsymbol{r}''$ denotes the locations of the scattering point. In (4.25), $\underline{\boldsymbol{G}}^{(m)}(\boldsymbol{r}', \boldsymbol{r}'')$ is the dyadic Green's function in the medium of the RO. It satisfies [20]

$$\nabla \times \nabla \times \underline{\boldsymbol{G}}^{(m)}(\boldsymbol{r}', \boldsymbol{r}'') - k^2_{0,m}\tilde{\varepsilon}^{(m)}_{\mathrm{RO,\,r}}(\boldsymbol{r}'')\underline{\boldsymbol{G}}^{(m)}(\boldsymbol{r}', \boldsymbol{r}'') = \overline{\boldsymbol{I}}\,\delta(\boldsymbol{r}' - \boldsymbol{r}'') \tag{4.27}$$

where $\overline{\boldsymbol{I}}$ is the identity matrix.

We assume that the complex relative permittivity is 1 for all voxels in the RO. The complex relative permittivity of the scatterer(s) in the OUT is denoted as $\tilde{\varepsilon}_{\mathrm{OUT,\,r}}^{(m)}(\boldsymbol{r}\,'')$. Note that the linear Born approximation is valid only when the constraints on the permittivity and the size δ of the scatterer are satisfied [20]:

$$\Delta\tilde{\varepsilon}_{\mathrm{r}}(\boldsymbol{r}\,'') \ll 1 \tag{4.28}$$

and

$$k_{0,m}\delta\Delta\tilde{\varepsilon}_{\mathrm{r}}(\boldsymbol{r}\,'') \ll 1 \tag{4.29}$$

where

$$\Delta\tilde{\varepsilon}_{\mathrm{r}}(\boldsymbol{r}\,'') = \left|\frac{\tilde{\varepsilon}_{\mathrm{OUT,\,r}}(\boldsymbol{r}\,'')}{\tilde{\varepsilon}_{\mathrm{RO,\,r}}(\boldsymbol{r}\,'')}\right| - 1\,. \tag{4.30}$$

In our study, we set $\Delta\tilde{\varepsilon}_{\mathrm{p}}(\boldsymbol{r}_0) = 0.05$, so that the first constraint is satisfied. Since the size δ of the scatterer is very small, the second constraint is also satisfied in both the near-zone and the far-zone imaging examples.

4.6 RESPONSE-DIFFERENCE DERIVATIVE TRANSFORMATION

As follows from (4.25), the scattered field $\mathbf{E}_{\mathrm{sc}}^{(m)}(\boldsymbol{r}_j, \boldsymbol{r}_k)$ observed at $\boldsymbol{r}_j$, when the antenna at $\boldsymbol{r}_k$ transmits and when a very small scatterer of volume $\Delta\Omega$ is present, is

$$\begin{aligned}\mathbf{E}_{\mathrm{sc}}^{(m)}(\boldsymbol{r}_j, \boldsymbol{r}_k) &\equiv \mathbf{E}_{\mathrm{sc},\,k}^{(m)}(\boldsymbol{r}_j) \\ &= k_{0,m}^2(\boldsymbol{r}\,'')\Delta\tilde{\varepsilon}^{(m)}(\boldsymbol{r}\,'')\underline{\mathbf{G}}^{(m)}(\boldsymbol{r}_j, \boldsymbol{r}\,'')\mathbf{E}_{\mathrm{RO},\,k}^{(m)}(\boldsymbol{r}\,'')\Delta\Omega,\ k = 1, 2.\end{aligned} \tag{4.31}$$

By reciprocity, $\underline{\boldsymbol{G}}^{(m)}(\boldsymbol{r}_j,\boldsymbol{r}")$ in (4.31) can be replaced by the incident field $\mathbf{E}_{\mathrm{RO},j}^{(m)}(\boldsymbol{r}")$ as follows. First, note that the field $\mathbf{E}_{\mathrm{RO},j}^{(m)}(\boldsymbol{r}_j,\boldsymbol{r}")$ at the location $\boldsymbol{r}_j$ due to a sufficiently small source at $\boldsymbol{r}"$ of volume $\Delta\Omega$ and current density $\boldsymbol{J}^{(m)}(\boldsymbol{r}")$ is determined through $\underline{\boldsymbol{G}}^{(m)}(\boldsymbol{r}_j,\boldsymbol{r}")$ as [20]

$$\mathbf{E}_{\mathrm{RO}}^{(m)}(\boldsymbol{r}_j,\boldsymbol{r}") = \mathrm{i}2\pi f_m \mu_0 \Delta\Omega \underline{\boldsymbol{G}}^{(m)}(\boldsymbol{r}_j,\boldsymbol{r}")\boldsymbol{J}^{(m)}(\boldsymbol{r}"). \tag{4.32}$$

In a reciprocal medium, $\underline{\boldsymbol{G}}^{(m)}(\boldsymbol{r}_j,\boldsymbol{r}") = \left[\underline{\boldsymbol{G}}^{(m)}(\boldsymbol{r}",\boldsymbol{r}_j)\right]^T$ [20]. Then, the incident field at $\boldsymbol{r}"$ due to a point source at $\boldsymbol{r}_j$ is:

$$\begin{aligned}\mathbf{E}_{\mathrm{RO}}^{(m)}(\boldsymbol{r}",\boldsymbol{r}_j) &\equiv \mathbf{E}_{\mathrm{RO},j}^{(m)}(\boldsymbol{r}") \\ &= \mathrm{i}2\pi f_m \mu_0 \Delta\Omega \left[\underline{\boldsymbol{G}}^{(m)}(\boldsymbol{r}_j,\boldsymbol{r}")\right]^T \boldsymbol{J}_j^{(m)},\ \boldsymbol{J}_j^{(m)} \equiv \boldsymbol{J}^{(m)}(\boldsymbol{r}_j)\end{aligned} \tag{4.33}$$

which can also be written as

$$\left[\underline{\boldsymbol{G}}^{(m)}(\boldsymbol{r}_j,\boldsymbol{r}")\right]^T \cdot \boldsymbol{\rho}_j J_0 \Delta\Omega = \frac{\mathbf{E}_{\mathrm{RO}}^{(m)}(\boldsymbol{r}")}{\mathrm{i}2\pi f_m \mu_0} = \underline{\boldsymbol{G}}^{(m)}(\boldsymbol{r}",\boldsymbol{r}_j)\cdot \boldsymbol{\rho}_j J_0 \Delta\Omega. \tag{4.34}$$

The relation allows for the replacement of $\underline{\boldsymbol{G}}^{(m)}(\boldsymbol{r}",\boldsymbol{r}_j)\cdot \boldsymbol{J}^{(m)}(\boldsymbol{r}_j)$ by the incident field $\mathbf{E}_{\mathrm{RO},j}^{(m)}(\boldsymbol{r}")$ due to the source at $\boldsymbol{r}_j$, $\boldsymbol{J}_j^{(m)}(\boldsymbol{r}_j)$.

On the other hand, from (4.23) and (4.24), it is evident that the response difference between the RO and the OUT relates to the scattered field as:

$$\Delta S_{jk}^{(m)}(\boldsymbol{r}) = S_{\mathrm{RO},jk}^{(m)}(\boldsymbol{r}) - S_{\mathrm{OUT},jk}^{(m)}(\boldsymbol{r}) = -\boldsymbol{\rho}_j \cdot \mathbf{E}_{\mathrm{sc}}^{(m)}(\boldsymbol{r}_j,\boldsymbol{r}_k) \tag{4.35}$$

where $\mathbf{E}_{\mathrm{sc}}^{(m)}(\boldsymbol{r}_j, \boldsymbol{r}_k)$ is expressed by (4.31). Substituting (4.31) into (4.35), and making use of (4.34) leads to

$$\Delta S_{jk}^{(m)}(\boldsymbol{r}) = \mathrm{i}2\pi f_m \varepsilon_0 \Delta\tilde{\varepsilon}_{\mathrm{r}}^{(m)}(\boldsymbol{r}'') J_0^{-1}\left[\mathbf{E}_{\mathrm{RO},\,j}^{(m)}(\boldsymbol{r}'') \cdot \mathbf{E}_{\mathrm{RO},\,k}^{(m)}(\boldsymbol{r}'')\right]. \tag{4.36}$$

Therefore, for a voxel-size scatterer embedded at $\boldsymbol{r}'' = \boldsymbol{r}_0$ in the background medium, the response difference in (4.35) becomes:

$$\Delta S_{jk}^{(m)}(\boldsymbol{r}) = \mathrm{i}2\pi f_m \varepsilon_0 \Delta\tilde{\varepsilon}_{\mathrm{r}}^{(m)}(\boldsymbol{r}_0) J_0^{-1}\left[\mathbf{E}_{\mathrm{RO},\,j}^{(m)}(\boldsymbol{r}_0) \cdot \mathbf{E}_{\mathrm{RO},\,k}^{(m)}(\boldsymbol{r}_0)\right]. \tag{4.37}$$

Note that in (4.12) and (4.37), the incident **E**-fields $\mathbf{E}_{\mathrm{RO},\,k}^{(m)}(\boldsymbol{\zeta})$, $\boldsymbol{\zeta} = \boldsymbol{r}', \boldsymbol{r}_0$, are computed using (4.19).

In the case of planar raster scanning, the permittivity map can be obtained by the substitution of (4.37) into (4.10):

$$D_{\varepsilon_{\mathrm{r}}}^{(m)}(\boldsymbol{r}') = \frac{\Delta\tilde{\varepsilon}_{\mathrm{r}}^{(m)}(\boldsymbol{r}_0) c^{(m)}}{N_x N_y} \cdot \sum_{n_y=1}^{N_y} \sum_{n_x=1}^{N_x} \sum_{j,k=1}^{2} \mathrm{Re}\left\{\left[-P^{(m)}(\boldsymbol{r}_0)\right]^* \cdot P^{(m)}(\boldsymbol{r}')\right\} \tag{4.38}$$

where

$$P^{(m)}(\boldsymbol{\rho}) = -\mathrm{i} \cdot \mathbf{E}_{\mathrm{RO},\,j}^{(m)}(\boldsymbol{\rho}) \cdot \mathbf{E}_{\mathrm{RO},\,k}^{(m)}(\boldsymbol{\rho}), \quad \boldsymbol{\rho} \equiv \boldsymbol{r}_0, \boldsymbol{r}'. \tag{4.39}$$

In summary, (4.38) represents the image that the algorithm produces when a point scatterer is located at position $\boldsymbol{r}_0$ in the OUT at the frequency f_m ($m = 1, \ldots, N_{\mathrm{f}}$). Hereafter, the frequency index *m* is omitted for brevity. Also, the subscript ε_{r} is omitted as it is always the default parameter of interest. Note that the Jacobian map in (4.38) is the PSF of the imaging algorithm at the *m*-th frequency.

The permittivity map expression in the case of circular array data acquisition is analogous to that of the planar raster scanning. Here, we present the final formula:

$$D_{\varepsilon_r}^{(m)}(\boldsymbol{r}') = -\frac{\Delta\tilde{\varepsilon}^{(m)}(\boldsymbol{r}_0)c^{(m)}}{N_e^2}\sum_{j=1}^{N_e}\sum_{k=1}^{N_e}\mathrm{Re}\left\{\left[P^{(m)}(\boldsymbol{r}_0)\right]^* P^{(m)}(\boldsymbol{r}')\right\}. \tag{4.40}$$

4.7 FUNDAMENTAL RESOLUTION LIMITS IN PLANAR RASTER SCANNING

The fundamental spatial resolution limit R_Δ of an imaging method is its best possible resolution. This best result can be achieved under three conditions: (i) noise-free responses; (ii) continuous spatial and frequency sampling in their respective observation domains; and (iii) infinitely large data acquisition planes. In the chosen setup, the first requirement is satisfied due to the analytical models of the incident and the scattered fields; see (4.19) and (4.25). To satisfy the second requirement, we assume infinitesimal sampling steps in the spatial and frequency domains. Such continuous sampling implies an infinite number of samples. To satisfy the third requirement, we assume that the acquisition surfaces are infinite, i.e., they are squares of size H, where $H \to \infty$. At the same time, the frequency band is limited between $f_{\min}$ and $f_{\max}$.

To investigate the spatial resolution, a single small (point-like) scatterer is assumed at the position $\boldsymbol{r}_0$. Under the sampling conditions stated above, the sums over the spatial and frequency samples in (4.14) can be transformed into integrals. Substituting

(4.38) into (4.14) and normalizing with respect to the length H of the scanning path along each direction, the normalized Jacobian map is obtained as:

$$M(\boldsymbol{r}') = \frac{1}{B}\int_{f_{\min}}^{f_{\max}} \bar{D}(\boldsymbol{r}')\mathrm{d}f = \frac{1}{B}\int_{f_{\min}}^{f_{\max}} N\left(D(\boldsymbol{r}')\right)\mathrm{d}f, \tag{4.41}$$

where

$$D(\boldsymbol{r}') = -\frac{\Delta\tilde{\varepsilon}_{\mathrm{r}}(\boldsymbol{r}_0)c^{(m)}}{H^2}\int_{-H/2}^{H/2}\int_{-H/2}^{H/2}\sum_{j,k=1}^{2}\mathrm{Re}\left\{\left[P(\boldsymbol{r}_0)\right]^* P(\boldsymbol{r}')\right\}\mathrm{d}x\mathrm{d}y \tag{4.42}$$

Here, $B = f_{\max} - f_{\min}$, where $f_{\min}$ and $f_{\max}$ are the lower and upper limits of the frequency band, respectively. N denotes the energy normalization using (4.13).

The final image is the plot of $|M(\boldsymbol{r}')|$ where the maximum/minimum value indicates the location of the point scatterer. This image is in effect the point-spread function (PSF) of the algorithm. Obtaining an explicit closed-form expression for the resolution limits involves an analytical inversion of the function $|M(\boldsymbol{r}')|$. To our best knowledge, this is not possible. Thus, by plotting a line cut of $|M(\boldsymbol{r}')|$ along the desired direction, we evaluate the resolution in the chosen direction as the width of the PSF at the – 3 dB level. In the following examples, we set the scatterer location $\boldsymbol{r}_0$ at the origin of the coordinate system.

4.7.1 Fundamental spatial resolution limits with far-zone data

In the far-zone imaging, the frequency band is in the range from $0.01 f_{\max}$ to $f_{\max}$, and the scanning plane distance is set to $D = 100\lambda_{\min}$. Note that the lower frequency limit $f_{\min}(= 0.01 f_{\max})$ is chosen to be much smaller (100 times) than $f_{\max}$ so that $f_{\min} \ll f_{\max}$

and the center frequency f_c is about $0.5 f_{max}$.

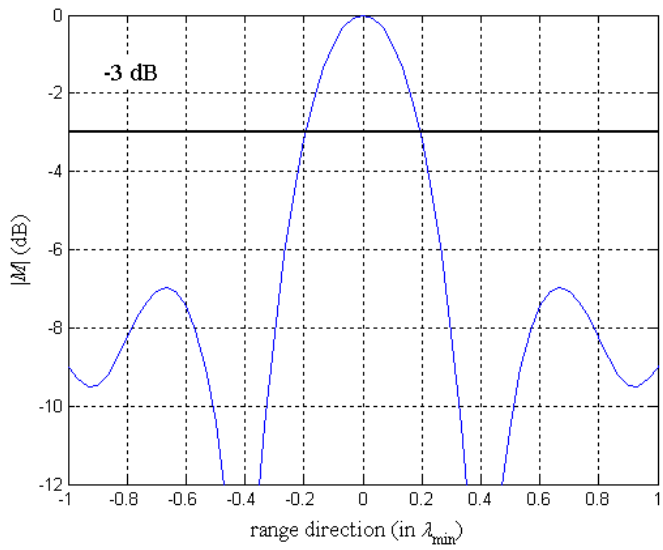

(a)

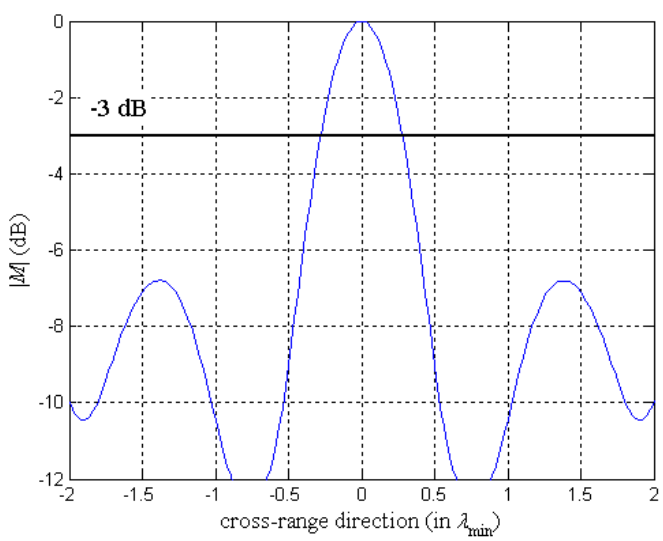

(b)

Fig. 4.3 Point-spread function in the range and the cross-range directions with far-zone wideband data: (a) range direction; (b) cross-range direction. The PSF width at –3 dB is $R_\Delta^{R} \approx 0.4\lambda_{min}$ in the range direction and $R_\Delta^{CR} \approx 0.6\lambda_{min}$ in the cross-range direction.

The PSF is calculated using (4.41). Fig. 4.3 shows the obtained image cuts of the PSF. The resolution is about $R_{\Delta}^{\mathrm{R}} \approx 0.4\lambda_{\min}$ (or about $0.2\lambda_{\mathrm{c}}$) in the range direction and about $R_{\Delta}^{\mathrm{CR}} \approx 0.6\lambda_{\min}$ (or about $0.3\lambda_{\mathrm{c}}$) in the cross-range direction. Here, $\lambda_{\min}$ is the wavelength at the maximum frequency $f_{\max}$ and λ_{c} is the wavelength at the center frequency f_{c}.

Experiments based on the analytical EM models also show that varying D (as long as D is sufficiently (usually ten times) larger than the central wavelength in the frequency range) has little influence on the resolution (results not shown for brevity).

4.7.2 Fundamental spatial resolution with near-zone data

In the near-zone imaging, various frequencies in the frequency range from $0.01f_{\max}$ to $f_{\max}$ are sampled. Two distances between the scanned planes, $D_1 = d_0$ and $D_2 = 5d_0$, where $d_0 = \lambda_{\min}/100$, are investigated. The PSF at a single frequency can be calculated using (4.42). We observe the image cuts of the single-frequency Jacobian maps $\left|M^{(m)}(\boldsymbol{r}')\right|$. The maps are obtained with different D at $f = f_{\max}$, i.e., $m = N_f$. From the results shown in Fig. 4.4(a)-(b), we observe that the resolution limit R_{Δ} relates to the scanning plane distance D. It is about $R_{\Delta}^{\mathrm{R}} \approx 0.3D$ in the range direction and about $R_{\Delta}^{\mathrm{CR}} \approx 0.8D$ in the cross-range direction. It is expected that in the near-zone imaging, the spatial resolution is practically independent of the frequency. This is confirmed by further experiments with the PSF at various frequencies between $0.01f_{\max}$ and $f_{\max}$. The results

are not shown for brevity. The averaged frequency maps at $D_1 = d_0$ and $D_2 = 5d_0$ are practically identical to the single-frequency maps shown in Fig. 4.4.

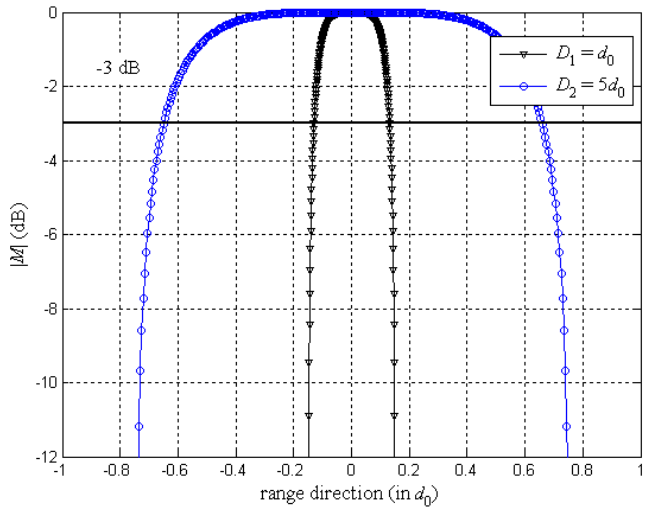

(a)

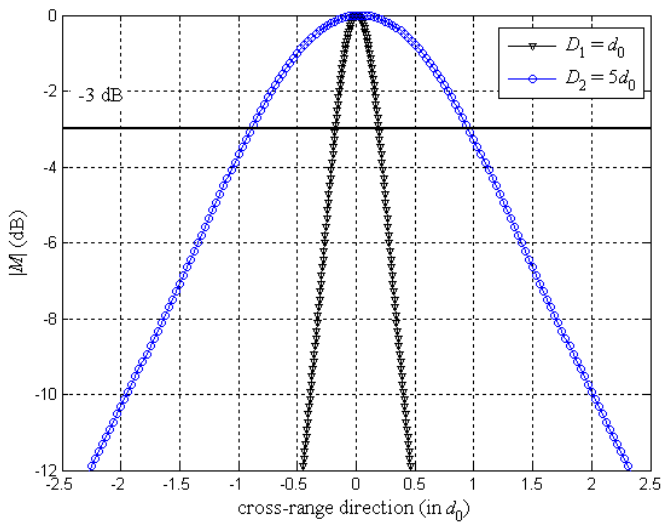

(b)

Fig. 4.4 Point-spread function in the range and the cross-range directions with near-zone data: (a) range direction; (b) cross-range direction. Here, $d_0 = \lambda_{\min} / 100$.

In a noise-free environment, the resolution limits obtained above are not influenced by the variation of the following factors: i) the size of the scatterer; ii) the discretization of the scatterer, i.e., the number of voxels in the scatterer volume as long as it is very small; and iii) the contrast of the scatterer as long as it observes (4.28) and (4.29).

It should also be noted that the resolution limits obtained above correspond to an ideal scenario where the spatial/frequency sampling is continuous and infinitely large scanning planes are used. The resolution may be affected by a limited number of spatial and frequency sampling points. This is valid particularly when noise is present since increasing the number of frequency and spatial samples in this imaging technique is a very efficient way to overcome noise through incoherent addition. The impact of the spatial sampling step on the image quality is discussed further through examples with noisy data in Section 4.11.

4.8 FAR-ZONE RESOLUTION LIMITS WITH SCANNING ON FINITE ACQUISITION PLANES

We first define an aperture angle $\alpha_{\max} = \arctan(H/D)$, which is the angle defined by the edge length of the scanning plane and the distance between the two scanned planes. The fundamental far-zone resolution limits in Section 4.7 corresponds to the case where $\alpha_{\max} \to \pi/2$. However, this is not practical in real-life scenarios where the size of the

scanning plane is usually limited.

Here, we study the impact of varying $\alpha_{\max}$ on the resolution limits in far-zone imaging. Fig. 4.5 summarizes the variation of the cross-range resolution versus $\alpha_{\max}$. It is evident that the cross-range resolution R_{Δ}^{CR} improves as the aperture angle $\alpha_{\max}$ increases. The relation between $\alpha_{\max}$ and R_{Δ}^{CR} can be approximately described by

$$R_{\Delta}^{\mathrm{CR}}(\alpha) \approx \frac{R_{\Delta\mathrm{O}}^{\mathrm{CR}}}{\sin \alpha_{\max}} \tag{4.43}$$

where $R_{\Delta\mathrm{O}}^{\mathrm{CR}}$ is the cross-range resolution obtained with infinite acquisition planes ($\alpha_{\max} = \pi / 2$). Further study also shows that $\alpha_{\max}$ has little influence on the range resolution.

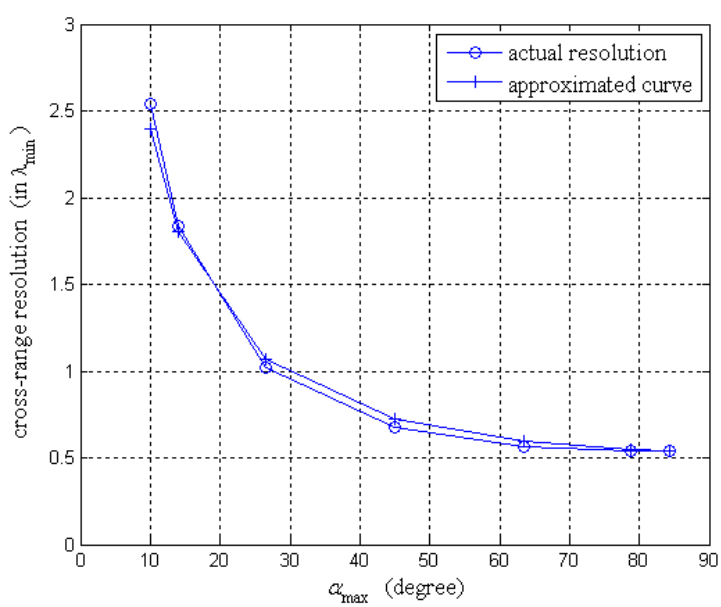

Fig. 4.5 Variation of the cross-range resolution versus $\alpha_{\max}$ and the approximated curve.

We emphasize that the above relationship holds as long as the constraints of the linear-Born approximation in (4.28) and (4.29) are satisfied. The result in (4.43) provides a theoretical guideline for determining the optimal size of the scanning plane for the required resolution limit.

4.9 FAR-ZONE RESOLUTION LIMITS WITH LIMITED TYPES OF RESPONSES IN PLANAR RASTER SCANNING

Here, we discuss the method's capability to resolve targets along the range and cross-range directions in the cases where only the reflection coefficients or only the transmission coefficients are available from planar-scan measurements.

In the cases where the scanning plane is infinitely large, by solving the exact PSFs in (4.41) using only the reflection or transmission coefficients, we can obtain the following results in the far-zone imaging:

- In the cases where only the reflection coefficients are used, both the range and cross-range resolution limits are well defined. The range resolution is about $0.4\lambda_{\min}$ and the cross-range resolution limit is about $0.6\lambda_{\min}$. The obtained results are identical to the fundamental range and cross-range resolution limits, respectively; see subsection 4.7.1.
- In the cases where only the transmission coefficients are used, resolving a target along the range direction is not possible. Meanwhile, the cross-range resolution limit is finite and it is the same as the fundamental cross-range resolution limit

$R_{\Delta CR} \approx 0.6\lambda_{\min}$.

Further numerical experiments show that, in both cases, the aperture angle $\alpha_{\max}$ has little influence on the range resolution while its relation to the cross-range resolution observes (4.43) (or Fig 4.5).

The above relationships also provide a guideline for the method's resolving capability when limited responses (i.e., only reflection or transmission coefficients) are available in real-life applications.

The exact inversion of the PSF in (4.41) is not possible, thus analytical expression for the above resolution limits are not available. However, an approximated inversion can be estimated under the assumption of $\alpha_{\max}$ being small, i.e., $H \ll D$. The detailed proof is presented in the Appendix.

4.10 VALIDATION OF THE RESOLUTION LIMITS WITH DOUBLE SCATTERER TARGET IN PLANAR RASTER SCANNING

The resolution limits obtained in the Section 4.7 are validated here with examples of a double-scatterer target imaging in both the far-zone and the near-zone scenarios. The setup for the OUT data acquisition has been illustrated in Fig 4.1. We set the voxel size to $\delta = 2$ mm . The distance between the two scatterers is denoted by *l*. In the range resolution example, the two scatterers are located at (0, 0, –*l*/2) and (0, 0, *l*/2). In the cross-range resolution example, the scatterers are located at (–*l*/2, 0, 0) and (*l*/2, 0, 0). The scanning step is set to $\Delta h = 8$ mm . Note that further decrease in Δh does not improve the

image quality. The length H of the scanning plane is set to $H = 2.5D$ in all examples. The aperture angle $\alpha_{\max}$ in this case is about 68˚. According to Fig 4.5, the cross-range resolution is expected to be practically the same as the fundamental cross-range resolution $R_{\Delta}^{\mathrm{CR}} \approx 0.6\lambda_{\min}$.

In the analytical models, the incident and scattered fields are computed as explained in Section 4.5. In particular, the incident field $\mathbf{E}_{\mathrm{RO}}^{(m)}$ is calculated using (4.19); the S-parameters $S_{\mathrm{RO},jk}^{(m)}$ are calculated using (4.24); and $S_{\mathrm{OUT},jk}^{(m)}$ are calculated using (4.23).

In this study, we consider the detection reliable when two criteria are met in the linear-scale maps: (i) the peaks that indicate the two scatterers are at least twice as large as all other local maxima in the reconstructed image; (ii) the minimum (dip) between the two maxima (peaks), as defined in (i) is at least twice smaller than these peaks.

4.10.1 Range resolution limit with far-zone data

In the far-zone imaging, we set $f_{\min} = 3$ GHz and $f_{\max} = 10$ GHz which is used in some microwave imaging systems [15][16]. Two scatterers are embedded in the OUT along the range direction (z-axis). The distance parameters used in the range resolution examples are listed in Table 4.1, cases 1 to 2.

TABLE 4.1

DISTANCE PARAMETERS IN THE DOUBLE SCATTERER: FAR-ZONE RASTER SCANNING EXAMPLES.

	case 1	case 2	case 3	case 4
l (mm)	8.00	28.00	12.00	36.00
D (mm)	200	200	200	200

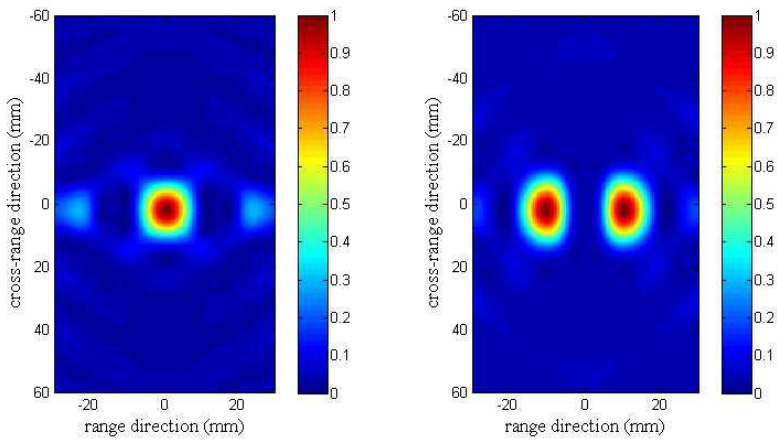

(a) (b)

Fig. 4.6 Reconstructed images in cases 1 to 2 (see Table 4.1): (a) case 1, $D = 200$ mm ($\approx 7\lambda_{\min}$), $l = 8$ mm ($\approx 0.3\lambda_{\min}$); (b) case 2, $D = 200$ mm ($\approx 7\lambda_{\min}$), $l = 28$ mm ($\approx \lambda_{\min}$).

Fig. 4.6 shows the reconstructed images. There, the two scatterers are discernible when l = 28 mm (about $\lambda_{\min}$ which is larger than $R_{\Delta}^{\mathrm{R}} = 0.4\lambda_{\min}$). Here, $\lambda_{\min}$ is the minimum wavelength in the frequency band. However, the two scatterers merge into a single object when l = 8 mm (about $0.3\lambda_{\min}$ which is less than $R_{\Delta}^{\mathrm{R}} = 0.4\lambda_{\min}$).

Further experiments show that, as expected, the variation of D has little influence on the range resolution. This confirms that the range resolution is about $R_{\Delta}^{\mathrm{R}} \approx 0.4\lambda_{\min}$ as obtained in Section 4.7.1.

4.10.2 Cross-range resolution limit with far-zone data

Two scatterers are embedded in the OUT along the cross-range direction (x-axis). The distance parameters used in the examples are listed in Table 4.1, cases 3 to 4. Fig. 4.7 shows the reconstructed images. The two scatterers are discernible when their separation distance is l = 36 mm (about 1.2 $\lambda_{\min}$ which is larger than $R_{\Delta}^{\mathrm{CR}} = 0.6\lambda_{\min}$). However, the two scatterers merge into a single object when l = 12 mm (about $0.4\lambda_{\min}$, less than $R_{\Delta}^{\mathrm{CR}} = 0.6\lambda_{\min}$). We observe that the cross-range resolution is about $R_{\Delta}^{\mathrm{CR}} \approx 0.6\lambda_{\min}$.

Further experiments show that the variation of D_0 has little influence on the resolution as expected. These examples confirm the cross-range resolution obtained in Section 4.7.

Double-scatterer validation examples have also been carried out using small aperture angles $\alpha_{\max}$. The results (not shown for brevity) are consistent with the conclusions in Section 4.8.

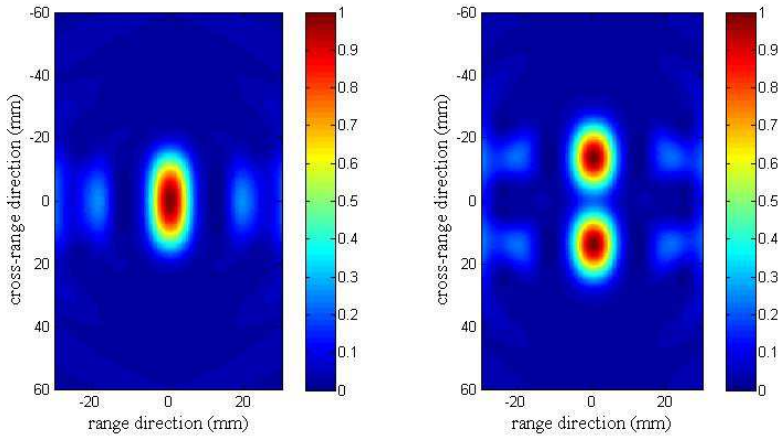

(a) (b)

Fig. 4.7 Reconstructed images in cases 3 to 4 (see Table 4.1): (a) case 3, $D = 200$ mm ($\approx 7\lambda_{\min}$), $l = 14$ mm ($\approx 0.5\lambda_{\min}$); (b) case 4, $D = 200$ mm ($\approx 7\lambda_{\min}$), $l = 36$ mm ($\approx 1.2\lambda_{\min}$).

TABLE 4.2

DISTANCE PARAMETERS IN THE DOUBLE SCATTERER: NEAR-ZONE RASTER SCANNING EXAMPLES.

	case 5	case 6	case 7	case 8
l (mm)	100	500	240	1200
D (mm)	200	1000	200	1000

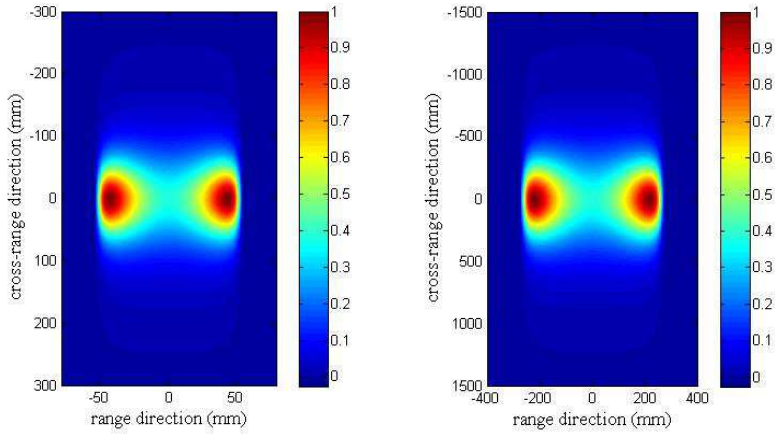

(a) (b)

Fig. 4.8 Reconstructed images in cases 5 and 6 (see Table 4.2): (a) case 5, D_1 = 200 mm, $l = 100$ mm ($\approx D_1/2$); (b) case 6, D_2 = 1000 mm, $l = 500$ mm ($\approx D_2/2$).

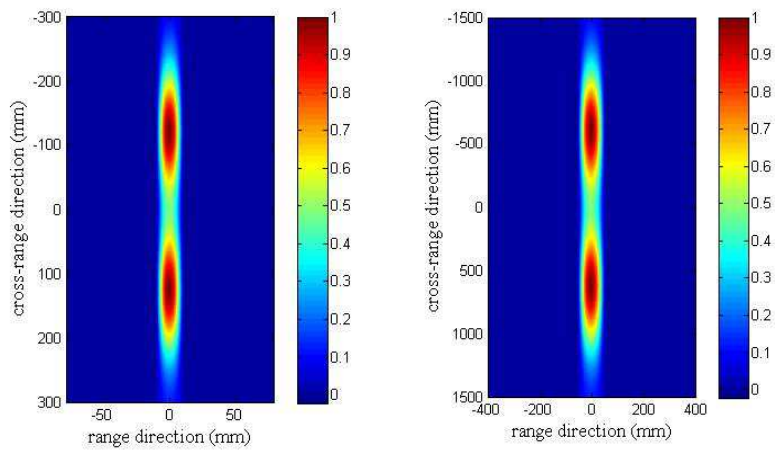

(a) (b)

Fig. 4.9 Reconstructed images of cases 7 and 8 (see Table 4.2): (a) case 7, D_1 = 200 mm, $l = 240$ mm ($\approx 1.2D_1$); (b) case 8, D_1 = 1000 mm, $l = 1200$ mm ($\approx 1.2D_2$).

4.10.3 Range and cross-range resolution limits with near-zone data

Two scanning plane distances are used: D_1 = 200 mm and D_2 = 1000 mm. The OUT distance parameters are listed in Table 4.2, cases 5 to 8. The frequency range is from 0.6 MHz to 6 MHz. The two scatterers are discernible in all the cases where they are placed at a distance above the theoretical resolution limits. The images are shown in Fig. 4.8 and 4.9.

Further experiments show that the two scatterers tend to merge into a single object when their separation distance l decreases (results not shown here). We observe that the resolution is about $R_{\Delta}^{\mathrm{R}} \approx 0.4D$ in the range direction, and it is about $R_{\Delta}^{\mathrm{CR}} \approx 0.8D$ in the cross-range direction. These limits are independent of the frequency. These examples confirm the theoretical resolution limits obtained in Section 4.7.

4.11 EFFECT OF NOISE ON IMAGE RECONSTRUCTION IN PLANAR RASTER SCANNING

In order to study the robustness to noise of the imaging algorithm, far-zone imaging examples with both the OUT and RO responses corrupted by Gaussian white noise (GWN) are used. The complex-valued GWN is generated as real plus imaginary part at given SNR level relative to the respective responses using Matlab function *awgn* [21]. Every example is repeated ten times in order to obtain a reliable observation.

Here, in order to study the impact of the spatial sampling rate on the image reconstruction with noisy data, we re-visit the double-scatter imaging setup used in

Section 4.10. In the range resolution examples, the distance between the two voxel-size targets is $l \approx \lambda_{\min}$ (larger than $R_{\Delta}^{\mathrm{R}} \approx 0.4\lambda_{\min}$). In the cross-range resolution examples, we set $l = 1.2\lambda_{\min}$ (larger than $R_{\Delta}^{\mathrm{CR}} \approx 0.6\lambda_{\min}$). The target contrast is again $\Delta\tilde{\varepsilon}_{\mathrm{p}}(\boldsymbol{r}_0)$ = 0.05. Fig. 4.10 summarizes the results in the case when the distance btween the acquisition planes is $D \approx 7\lambda_{\min}$ ($D = 200$ mm), $f_{\min}$ = 3 GHz, and $f_{\max}$ = 10 GHz. The scanning step Δh decreases from 32 mm to 4 mm. And for each Δh the minimum required SNR is determined such that the target is imaged reliably as per the criteria described in Section 4.10. As expected, the minimum SNR decreases as the scanning step Δh decreases. Reducing Δh below 16 mm (about $\lambda_{\min}/2$) does not lead to further significant improvement in the image quality. Note that the same relation between the scanning step Δh and the minimum SNR is obtained in examples of double scatterer in the cross-range direction. This result is not shown for brevity.

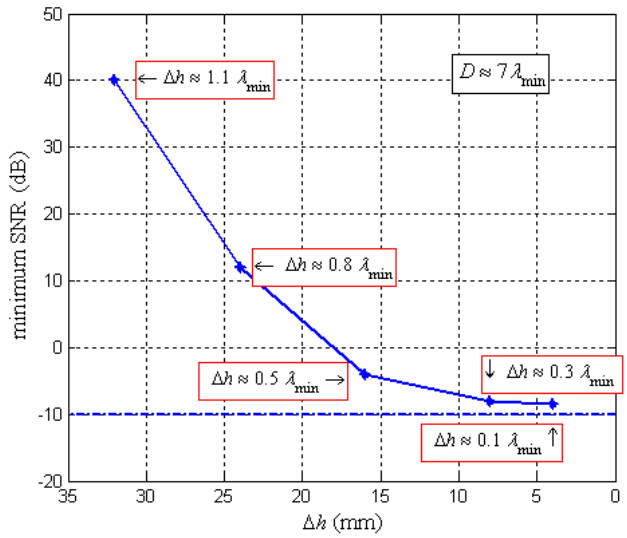

Fig. 4.10 Minimum SNR for resolving the two scatterers along the range direction at different scanning steps Δh. All results are obtained in the cases where $D = 7\lambda_{\min}$.

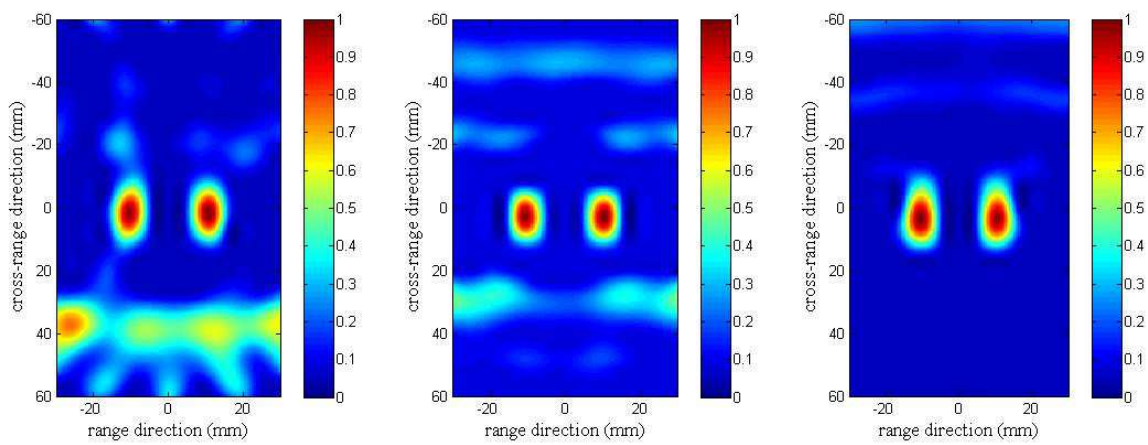

(a) (b) (c)

Fig. 4.11 Images in case 6 using noisy data: (a) Δh = 32 mm; (b) Δh = 8 mm; and (c) Δh = 4 mm. Here, $l = 28$ mm $\approx \lambda_{\min}$, $D = 200$ mm $\approx 7\lambda_{\min}$, SNR = 0 dB.

Further, note that the above general observation—minimum SNR decreases as spatial sampling rate increases—holds for any target contrast as long as it observes (4.28) as well as for any other distance D that is sufficiently larger than the wavelength at the minimum frequency (far-zone data acquisition). However, as the size of the scatterer and/or the scatterer-to-background contrast increases, the minimum required SNR decreases for a given spatial sampling step Δh.

As an illustration of the impact of noise on the image quality, Fig. 4.11 shows the images obtained with SNR = 0 dB when $D = 7\lambda_{\min}$ and $\Delta\tilde{\varepsilon}_{\mathrm{p}}(\boldsymbol{r}_0) = 0.05$. The two scatterers are placed along the range direction at a distance $l \approx \lambda_{\min}$. The frequency is from 3 GHz to 10 GHz. Three scanning steps are used in both the range and cross-range examples: $\Delta h = 32$ mm, $\Delta h = 8$ mm, and $\Delta h = 4$ mm. The image quality visibly improves when the spatial sampling rate is higher (Δh is smaller). However, this improvement becomes unnoticeable when Δh is below about $\lambda_{\min}/2$. Note that similar results (not shown for brevity) are also obtained in the cases where the two scatterers are placed along the cross-range direction.

This study (see Fig. 4.10) also reveals that the sensitivity-based imaging technique is not fundamentally limited by the minimum Nyquist sampling rate of half-wavelength, which is typical for the imaging methods performing inversion in Fourier space. In fact, further experiments with analytical models and noise-free responses ($\mathrm{SNR} \to \infty$) show reliable reconstruction even when the spatial sampling step Δh is as large as $1.5\lambda_{\min}$.

Analogous study has also been carried out with respect to the frequency sampling rate. As expected, increasing the number of frequency samples improves the noise

robustness and results in a reduced minimum SNR with which reliable target detection is obtained.

4.12 FUNDAMENTAL RESOLUTION LIMITS IN CIRCULAR ARRAY DATA ACQUISITION

Similar to the case of planar raster scanning in Section 4.7, the fundamental resolution limit is achieved under two conditions: (i) no noise or uncertainty in the responses; and (ii) continuous sampling in the observation domains (e.g., space and frequency). In the chosen setup, the first requirement is satisfied due to the analytical models of the incident and the scattered field. To satisfy the second requirement, the following conditions are imposed: (i) the number of the Tx/Rx antennas is infinite, i.e., $N_{\mathrm{e}} \to \infty$; (ii) the number of frequency samples is infinite in the desired frequency band, i.e., $N_{\mathrm{f}} \to \infty$. In any other non-ideal case, the resolution limit can be expected to be larger than the fundamental limit R_{Δ}.

Under the above conditions, the sums over the spatial and frequency samples in (4.17) are transformed into integrals. Using (4.40) and normalizing with respect to the circle's circumference $C = 2\pi R$, the averaged frequency Jacobian map is obtained as:

$$M(\boldsymbol{r}') = \frac{1}{B} \int_{f_{\min}}^{f_{\max}} N\left(D(\boldsymbol{r}')\right) \mathrm{d}f \tag{4.44}$$

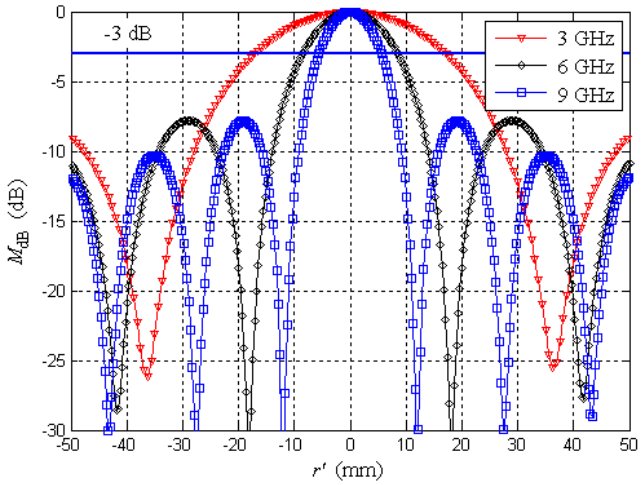

(a)

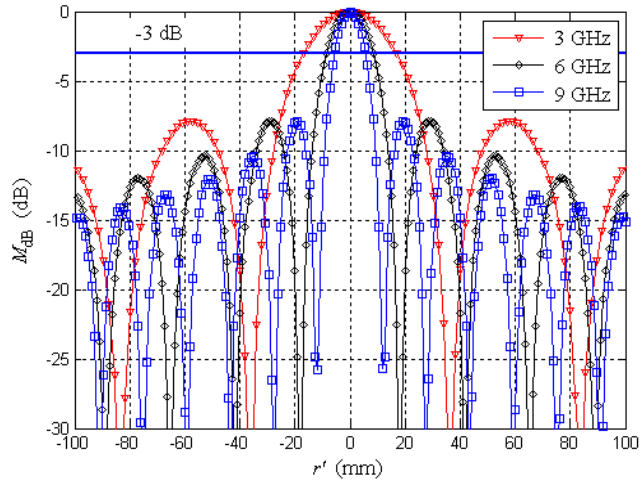

(b)

Fig. 4.12 Image cuts at the frequencies $f_0 = 3$ GHz, 6 GHz, and 9 GHz, obtained with different array radii: (a) $R = 100$ mm ; (b) $R = 500$ mm . The image cut is along the array diameter passing through the scatterer.

where $B = f_{\max} - f_{\min}$ is the bandwidth, N denotes energy normalization using (4.13) and

$$D(\boldsymbol{r}') = -\frac{\Delta\tilde{\varepsilon}(\boldsymbol{r}_0)c^{(m)}}{4\pi^2}\int_0^{2\pi}\int_0^{2\pi}\mathrm{Re}\left\{\left[P(\boldsymbol{r}_0)\right]^* P(\boldsymbol{r}')\right\}\mathrm{d}\varphi_j\mathrm{d}\varphi_k\,. \tag{4.45}$$

In this section, the resolution limits are obtained by solving (4.44) numerically. The obtained PSF is plotted along the diameter passing through the point scatterer and the resolution is estimated as its width at the –3 dB level. Here, we set the scatterer location at the origin of the coordinate system.

4.12.1 Spatial resolution with far-zone data

In the far-zone imaging, the frequency band is from 3 GHz to 10 GHz. The array radius R, which varies between 100 mm and 500 mm, is at least three times larger than $\lambda_{\min}$ in the frequency band. We first observe the PSF at the sampled frequencies f_m obtained by using (4.45). The double integral is calculated numerically and the maps $|M(\boldsymbol{r}')|$ of the single scatterer (in dB) are obtained for two different array radii, R = 100 mm and R = 500 mm, at various frequencies. Fig. 4.12 shows the variation of $|M(\boldsymbol{r}')|$ (in dB) along the array diameter passing through the single-voxel scatterer. We observe that the resolution R_Δ at the –3 dB level is subject to the diffraction limit and is about $R_\Delta \approx \lambda_m / 3$. Here, λ_m is the wavelength of the sampled frequency f_m. Comparing Fig. 4.12 (a) and (b), we also observe that an increase in the array radius R has little influence on the result.

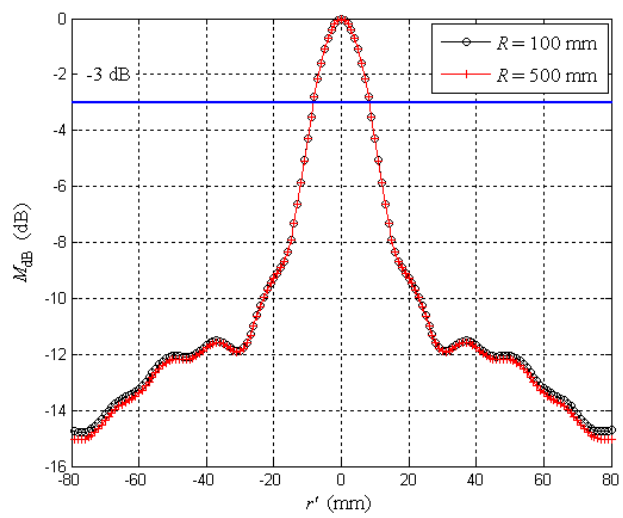

Fig. 4.13 Image cuts obtained using wideband data from 3 GHz to 10 GHz with different array radii. The image cut is along the array diameter passing through the scatterer.

Next, we obtain an image by evaluating the integral in (4.44) using wideband data in the frequency band from 3 GHz to 10 GHz:

$$M(\boldsymbol{r}') = \frac{1}{B} \int_{3\text{ GHz}}^{10\text{ GHz}} N\left(D(\boldsymbol{r}')\right) \mathrm{d}f. \tag{4.46}$$

Again, the array radius R is set to 100 mm and 500 mm. The integral in (4.46) is calculated numerically and the results are shown in Fig 4.13. The resolution limit is about R_Δ = 16 mm (about $\lambda_{\min}/2$) in both cases. It is evident that the spatial resolution is a function of wavelength (or frequency) and it decreases as sampled frequency increases. Again, the array radius has little influence on the spatial resolution.

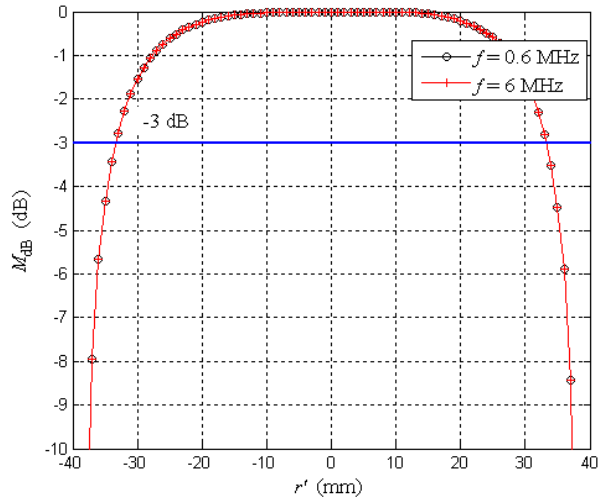

(a)

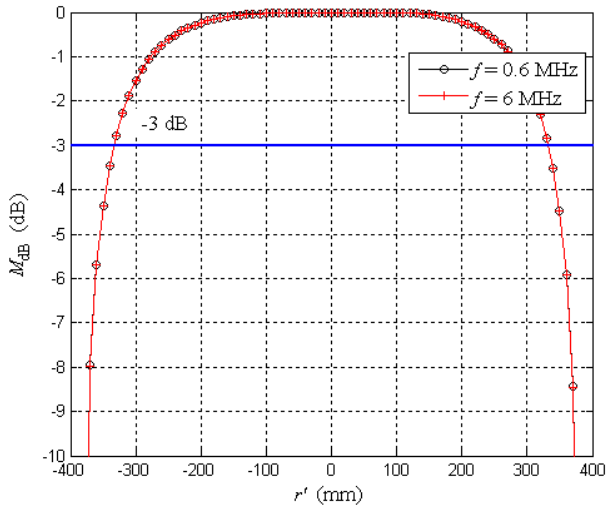

(b)

Fig. 4.14 Image cuts obtained with different array radii at 0.6 MHz and 6 MHz: (a) $R = 100$ mm ; (b) $R = 500$ mm . The image cut is along the array diameter passing through the scatterer.

4.12.2 Spatial resolution with near-zone data

In the near-zone imaging, the frequency range is set from 0.6 MHz to 6 MHz. In this case, the array radius R is at least a hundred times smaller than the shortest wavelength $\lambda_{\min}$.

We first observe the image cuts obtained from the frequency Jacobian maps at single frequencies: $f_1 = 0.6$ MHz and $f_2 = 6$ MHz. From the results shown in Fig. 4.14, we observe that the resolution limit R_Δ is related to the array radius and is about $R_\Delta \approx 2R/3$. We also observe that in the near-zone imaging, the resolution limit is practically independent of the frequency. As a result, the averaged frequency Jacobian map shows a resolution limit R_Δ which is the same as the one obtained from the single-frequency maps.

Note that similar to the case of planar raster scanning, in a noise-free environment, the resolution limits obtained with circular array data acquisition are not affected by the variation of the following factors: (i) the size of the small scatterer, (ii) the discretization of the scatterer, and (iii) the permittivity of the scatterer as long as it observes (4.28) and (4.29).

Further, note that the fundamental resolution limits are obtained assuming that the spatial and frequency sampling are continuous. The resolution limits may be affected by the number N_{e} of the Tx/Rx antennas and the number N_{f} of the frequency points. In addition, the choice of N_{e} also depends on the expected noise level. The impact of N_{e} on the image quality is discussed through the examples with noisy data in Section 4.14.

TABLE 4.3

DISTANCE PARAMETERS IN THE DOUBLE SCATTERER EXAMPLES WITH FAR-ZONE CIRCULAR ARRAY

case	l (mm)	R (mm)	true location (mm)	estimated location (mm)
1	10.00	100.00	$P_1(-5,0)$, $P_2(5,0)$	NA
2	22.00	100.00	$P_1(-11,0)$, $P_2(11,0)$	$P_1'(-13.5,-2.0)$, $P_2'(9.0,-1.9)$
3	22.00	250.00	$P_1(-11,0)$, $P_2(11,0)$	$P_1'(-11.1,-1.9)$, $P_2'(10.8,-1.9)$
4	22.00	500.00	$P_1(-11,0)$, $P_2(11,0)$	$P_1'(-8.8,-1.8)$, $P_2'(12.1,-1.8)$

4.13 VALIDATION OF THE RESOLUTION LIMITS WITH DOUBLE SCATTERER USING CIRCULAR ARRAY DATA ACQUISITION

The resolution limits obtained in Section 4.12 are validated with examples of double-scatterer imaging in the far-zone and the near-zone scenarios. The setups for the RO and the OUT data acquisitions have been illustrated in Fig 4.2. We set the voxel size to $\delta = 2$ mm. The number of Tx/Rx antennas is set to $N_e = 36$. Note that further increase in N_e does not improve the image quality. The distance between the two scatterers is denoted by l.

Note that the criteria of reliably detecting double scatterer are the same as those discussed in Section 4.9.

4.13.1 Far-zone imaging

The parameters used in the examples are listed in Table 4.3 together with the true and predicted locations of the two scatterers. The frequency band is from 3 GHz to 10 GHz.

In case 1, $R = 100$ mm (about $3\lambda_{\min}$) while $l = 10$ mm ($< \lambda_{\min}/2$), which is smaller than R_{Δ}. The two scatterers are not discernible. They have merged into a single bright spot in the image as shown in Fig. 4.15(a). In cases 2 to 4, where the scatterers are separated by a distance $l = 22$ mm ($> \lambda_{\min}/2$), the two scatterers are discernible regardless of the increase in the array radius; see Fig. 4.15(b) to (d). These results confirm the resolution limit obtained in Section 4.12.1.

4.13.2 Near-zone imaging

Here, the frequency band is set from 0.6 MHz to 6 MHz. Two array radii $R =$ 100 mm and $R =$ 500 mm are used in order to investigate the dependence of the results on this system parameter. The scatterers' separation is set to l = 100 mm and l = 500 mm in two separate examples. The two scatterers are discernible and the images are shown in Fig. 4.16. Further experiments also show that the two scatterers tend to merge into a single object as l decreases below $R_{\Delta} = 2R/3$ (results not shown here). The above examples confirm the resolution limit obtained in Section 4.12.2.

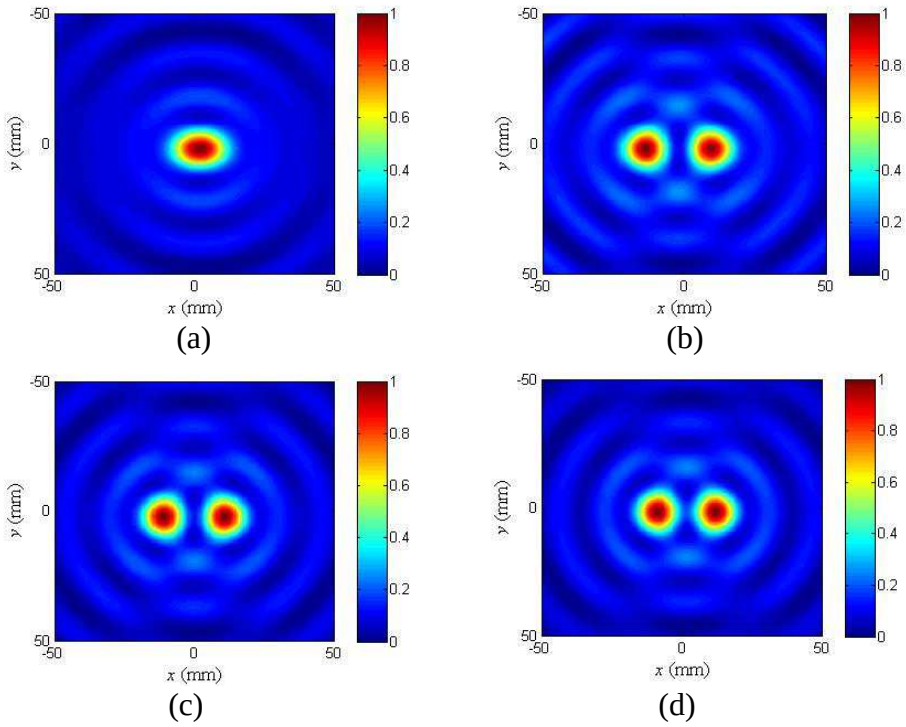

Fig. 4.15 Images obtained in the far-zone scenario with $N_e = 36$: (a) case 1, l = 10.00 mm ($\approx \lambda_{min}/3$) and R = 100 mm ($\approx 3\lambda_{min}$); (b) case 2, l = 22.00 mm ($> \lambda_{min}/2$) and R = 100 mm ($\approx 3\lambda_{min}$); (c) case 3, l = 22.00 mm ($> \lambda_{min}/2$) and R = 250 mm ($\approx 8\lambda_{min}$); (d) case 4, l = 22.00 mm ($> \lambda_{min}/2$) and R = 500 mm ($\approx 16\lambda_{min}$).

It should be noted that the spatial resolution limit is hardly influenced by the position of the scatterer(s) relative to the array in the far-zone imaging. However, this is not the case in the near-zone imaging where further experiments have shown that the resolution improves when the double-scatter pair is located off-center. The resolution limit obtained in Section 4.13.2 is the worst case scenario as far as the scatterer location is concerned.

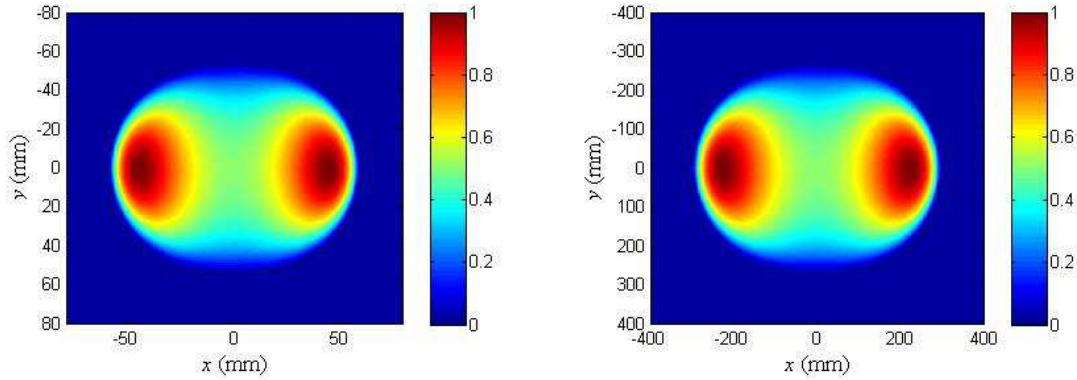

(a) (b)

Fig. 4.16 Images obtained in the near-zone scenario with $N_e = 36$: (a) l = 100 mm ($\approx R$) and R = 100 mm; (b) l = 500 mm ($\approx R$) and R = 500 mm.

4.14 EFFECT OF NOISE ON IMAGE RECONSTRUCTION IN CIRCULAR ARRAY DATA ACQUISITION

Similar to Section 4.11 where the effect of noise is studied for the case of planar raster scan, here, far-zone imaging examples with responses in both the OUT and RO models corrupted by GWN are used in the cases of circular-sensor array data acquisition.

For a given SNR, the image quality is influenced by the following factors: (i) the array radius R, (ii) the number N_e of Tx/Rx antennas, and (iii) the arc length t along the circumference between two adjacent receivers. These factors are inter-related. It is expected that the spatial sampling rate, which is reflected by the value of t, is the most relevant system parameter.

Here, we re-visit the double-scatterer imaging setup used in Section 4.12. The distance between the two voxel-size scatterers is fixed at $l = 22$ mm $(> \lambda_{\min}/2)$. The target contrast is again $\Delta\tilde{\varepsilon}_{\mathrm{p}}(\boldsymbol{r}_0) = 0.05$. Fig. 4.17 summarizes the results in the case when the array radius is $R \approx 16\lambda_{\min}$ ($R = 500$ mm, $f_{\min} = 3$ GHz and $f_{\max} = 10$ GHz). The number of Tx/Rx points N_{e} increases from 9 to 360 and for each N_{e} the minimum SNR is determined such that the target is imaged reliably as per the criteria described in Section 4.10. The spatial sampling step t is also shown. As expected, the minimum SNR decreases as the sensor number N_{e} increases (or the spatial sampling step t decreases). Reducing t below $\lambda_{\min}/2$ does not lead to further significant improvement in the noise robustness.

The above general relation, i.e., minimum SNR decreases as spatial sampling rate increases, holds for any target contrast as long as it observes (4.28) and (4.29) in the far-zone imaging.

As an illustration of the impact of noise on the image quality, Fig. 4.18 shows images obtained with SNR = 20 dB when $R \approx 16\lambda_{\min}$ and $\Delta\tilde{\varepsilon}_{\mathrm{p}}(\boldsymbol{r}_0) = 0.05$. Three images are shown for the cases of N_{e} = 18, N_{e} = 144, and N_{e} = 288. The image quality visibly improves when more spatial samples are used. However, this improvement becomes unnoticeable when N_{e} exceeds 288 (or t decreases below $\lambda_{\min}/3$).

This study (see Fig. 4.17) also reveals that the sensitivity-based imaging technique is not fundamentally limited by the minimum Nyquist sampling rate of half a wavelength, which is typical for the imaging methods performing inversion in Fourier space. In fact,

further experiments with analytical models and noise-free responses ($\mathrm{SNR} \to \infty$) show reliable reconstruction when the spatial sampling step t is as large as $10\lambda_{\min}$.

Analogous study has also been carried out with respect to the frequency sampling rate. As expected, increase in the number N_{f} of the frequency samples improves the noise robustness and results in a reduced minimum SNR at which the reliable target detection is obtained.

Comparing the results shown in Fig. 4.10 and 4.17, the minimum required SNR is lower in the case of planar raster scanning than that of the circular array. This is because the signal in the former case transmits and receives in a direct path and it allows maximum power coupled to the receiver which results in better robustness to noise.

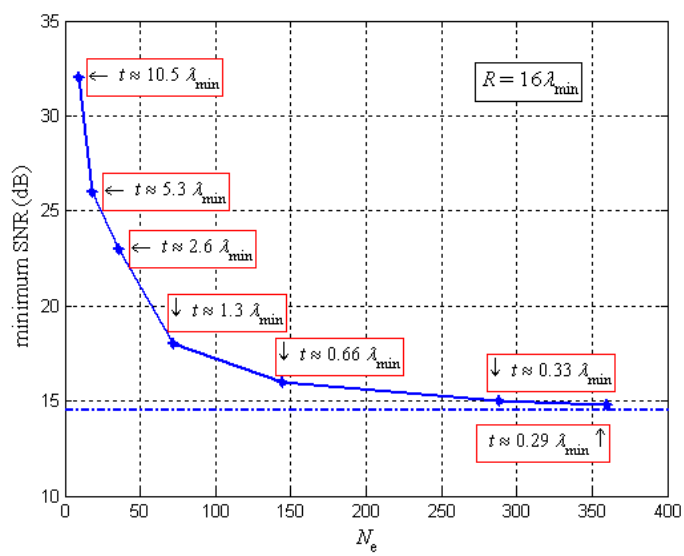

Fig. 4.17 Minimum SNR versus the number of Tx/Rx antennas required to resolve the two scatterers when $R = 16\lambda_{\min}$ and $\Delta\tilde{\varepsilon}_{\mathrm{p}}(\boldsymbol{r}_0) = 0.05$.

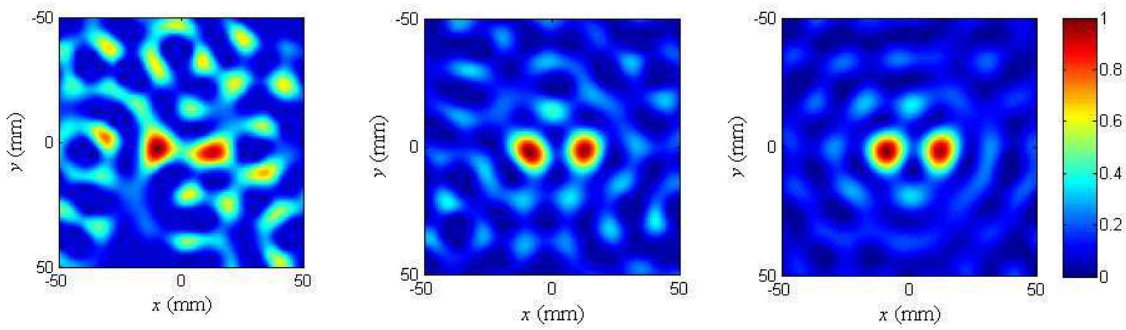

(a) (b) (c)

Fig. 4.18 Images obtained with varying number of Tx/Rx antennas (SNR = 20 dB, $R \approx 16\lambda_{\min}$): (a) $N_e = 18$, (b) $N_e = 144$, and (c) $N_e = 288$.

4.15 CONCLUSION

The spatial resolution of a promising microwave imaging technique based on response sensitivity analysis is studied. The technique features real-time image reconstruction from the measured microwave responses of an object under test once the electromagnetic simulation of the reference object is available.

Here, regorous methodology is proposed to study the spatial resolution of the sensitivity-based imaging with a raster-scan and a circular-array data acquisitions. The fundamental spatial resolution limits are derived from the analytical point-spread function (PSF) of the method and are then validated with double-scatterer imaging examples. It is concluded that the resolution limits are fractions of the center frequency wavelength in the far-zone imaging, and they are fraction of the sensor-to-sensor distance in the near-zone imaging.

The analytical PSF of the method is derived under ideal conditions as follows: (i)

point-wise sources and point-wise field sampling which allow for analytically modeled noise-free responses, and (ii) infinitesimal spatial and frequency sampling steps. Therefore, the obtained resolution limits are fundamental, i.e., they describe the best possible performance of the method. The spatial resolution is expected to be poorer under realistic non-ideal conditions depending on factors such as spatial and frequency sampling rates, signal-to-noise ratio (SNR), and the fidelity of the EM model of the reference object. Note also that the method has been proven to rely on the linear Born approximation [20]; therefore, the contrast and size of the scatterer would impact the spatial resolution if the respective limits (4.28) and (4.29) are not observed.

In the case of planar raster scanning, the method's resolution limits are also studied in non-ideal cases. The cross-range resolution is affected by the aperture angle $\alpha_{\max}$ and it improves as $\alpha_{\max}$ increases. In the case where only the reflection coefficients are available, both the range and cross-range resolution limits are finite and identical to the fundamental limits. Meanwhile, in the case where only the transmission coefficients are available, range resolution cannot be achieved, i.e., it is infinite. The cross-range resolution is the same as that for the reflection coefficients.

Further, the performance of the algorithm under various SNR levels in the measured responses is studied and related to the spatial and frequency sampling rates. As expected, the method's robustness to noise improves as the spatial and frequency sampling rates increases.

REFERENCES

[1] L. E. Larsen, and J. H. Jacobi, *Medical Applications of Microwave Imaging*. New York: IEEE Press, 1986.

[2] A. B. Wolbarst, R. G. Zamenhof, and W. R. Hendee *Advances in Medical Physics*. Madison WI: Medical Physics Publishing, 2006.

[3] R. M. Meaney, M. W. Fanning, D. Li, S. P. Poplack, and K. D. Paulsen, "A clinical prototype for active microwave imaging of the breast," *IEEE Trans. Microwave Theory Tech*., vol. 48, no. 11, pp. 1841–1853, 2000.

[4] E. Fear, X. Li, S. C. Hagness, and M. A. Stuchly, "Confocal microwave imaging for breast cancer detection: localization of tumours in three dimensions," *IEEE Trans. Biomed. Eng.*, vol. 49, no. 8, pp. 812–822, 2001.

[5] Z. Q. Zhang, and Q. H. Liu, "Three-dimensional nonlinear image reconstruction for microwave biomedical imaging," *IEEE Trans. Biomed. Eng.*, vol. 51, no. 3, pp. 544–548, 2004.

[6] T. Rubaek, P. M. Meaney, P. Meincke, and K. D. Paulsen, "Nonlinear microwave imaging for breast-cancer screening using Gauss–Newton's method and the CGLS inversion algorithm," *IEEE Trans. Antennas Propag.*, vol. 55, no. 8, pp. 2320–2331, 2007.

[7] M. Pastorino, *Microwave Imaging*. USA: John Wiley & Sons, Inc., 2010.

[8] R. Zoughi, *Microwave Non-Destructive Testing and Evaluation*. USA: Kluwer Academic Publishers, 2002.

[9] M. Pastorino, A. Massa, and S. Caorsi, "A global optimization technique for

microwave nondestructive evaluation," *IEEE Trans. Instrum. Meas.*, vol. 51, no. 4, pp. 666–673, 2002.

[10] I. Aliferis, C. Pichot, J. Y. Dauvignac, and E. Guillanton, "Tomographic reconstructions of buried objects using a nonlinear and regularized inversion method," *Proc. Int. Non-Linear Electromagn. Syst. Symp.*, 1999.

[11] T. K. Chan, Y. Kuga, and A. Ishimaru, "Subsurface detection of a buried object using angular correlation function measurement," *Waves in Random and Complex Media*, vol. 7, pp. 457–465, 1997.

[12] N. G. Paulter, *Guide to the technologies of concealed weapon imaging and detection*. Available online at: http://www.ncjrs.gov/pdffiles1 /nij/184432.pdf, 2001.

[13] A. Agurto, Y. Li, G. Y. Tian, N. Bowring and S. Lockwood, "A review of concealed weapon detection and research in perspective," *Proc. of the IEEE Int. Conf. on Networking, Sensing and Control*, pp. 443–448, 2007.

[14] L. Liu, A. Trehan, and N. K. Nikolova, "Near-field detection at microwave frequencies based on self-adjoint response sensitivity analysis," *Inverse Problems*, vol. 26, 105001, 2010.

[15] N. K. Nikolova, "Microwave imaging for breast cancer detection," *IEEE Microwave Magazine*, vol. 12, no. 7, pp. 78–94, 2011.

[16] R. K. Amineh, M. Ravan, A. Khalatpour, and N. K. Nikolova, "Three-dimensional near-field microwave holography using reflected and transmitted signals," *IEEE Trans. Antennas Propag.*, vol. 59, no. 12, pp. 4777−4789, 2011.

[17] IEEE standard board, *IEEE standard definitions of terms for antennas*, IEEE Std 145-1993 (NY, USA: IEEE), 1993.

[18] Y. Song, and N. K. Nikolova, "Memory efficient method for wideband self-adjoint sensitivity analysis," *IEEE Trans. Microwave Theory Tech.*, vol. 56, no. 8, pp. 1917–1927, 2008.

[19] C. A. Balanis, *Antenna Theory, 2nd ed.* USA: WILEY, 1997.

[20] W. C. Chew, *Waves and Fields in Inhomogeneous Media*. NY, USA: IEEE PRESS, 1995.

[21] MATLAB (R2010a), The MathWorks, Inc., USA, 2010.

Chapter 5

APPLICATIONS TO IMAGING OF NUMERICAL AND PHYSICAL TISSUE PHANTOMS

5.1 INTRODUCTION

Preliminary study [1]-[4] has shown the promise of the sensitivity-based imaging using numerical examples. In this work, the resolution and robustness to noise of the sensitivity-based imaging method have been studied using data provided by analytical models in the cases of planar raster scan and circular array data acquisitions; see Chapter 4. In this chapter, image reconstruction is performed utilizing the simulated and measured data obtained from raster scanning over human-tissue models/phantoms containing tumor simulant(s).

In the sensitivity-based imaging, the choice of the reference object (RO) affects greatly the reconstructed image as it provides the incident field distribution and the RO responses to the algorithm. When imaging a given object under test (OUT), different ROs can be used, which will result in different images. Typically, the RO would mimic as closely as possible the background (target-free) medium and would include an accurate representation of the antennas. However, obtaining the simulated **E**-field distribution in

the RO requires significant computational effort when the background medium is highly heterogeneous, which is the case in human-tissue imaging. In addition, in human tissue imaging, the knowledge of the heterogeneous background of the OUT is usually not available. Thus, an exact RO, having the same background medium as that of the OUT, is usually not available. Therefore, based on numerical models, we present a preliminary study of image reconstruction using inexact ROs where the background medium differs from that in the OUT.

Image reconstruction is also performed using measured data. The phantoms are box shaped to emulate the slightly compressed human tissue (e.g. breast) during examination. The background materials of the phantoms are made to mimic the human breast tissues[1]. The tumor simulants have similar dielectric properties to those of malignant tumors [6][7]. In the raster scanning data acquisition, two identical TEM horn antennas [8][9] are used. They are placed on the opposite sides of the imaged object while facing each other along boresight. This is because the signal attenuation in tissue is very high and the signal-to-noise ratio (SNR) for signals propagating away from the boresight is usually low. Such alignment of the sensors can provide the shortest path for the signals and, therefore, results in the strongest signal level. During the scanning over the *xy*-plane, they move simultaneously to scan the rectangular aperture at a pre-determined sampling step while one antenna transmits and the other receives. The scattering parameters (*S*-parameters) are measured at all desired frequencies at each scan location. The raster scanning is performed twice to provide two data sets: (i) the *S*-parameters measured with

[1] The background medium of the breast tissue phantom has the properties of the weighted average of the whole breast [6].

the OUT; (ii) the *S*-parameters measured with the RO. Here, we choose the RO to be the same as the OUT except that there is no tumor simulant.

The impedance of the two TEM horn antennas is well matched from 3 GHz to 10 GHz. The antennas are filled with high permittivity low loss dielectric material, the permittivity of which is similar to the property of the phantom's background material. The reflection at the interface between the antenna aperture and the phantom is thus reduced.

5.2 IMAGE RECONSTRUCTION USING SIMULATED DATA

Two types of models are presented: (i) simple layered structure model, and (ii) complex human breast model. Point-like Tx/Rx pair is used for the raster scanning in both models. During the scan, two antennas placed on the opposite sides of the imaged object move together to scan their respective (mutually parallel) planes.

The OUT contains the tumor simulant embedded in a heterogeneous medium. The RO does not contain tumor simulants and the medium is assumed to be homogeneous. The dielectric properties of the homogeneous background are chosen to match one of dielectric materials in the OUT.

5.2.1 Simple layered structure

The 2D cross section which contains the center of the scatterer in the 3D structure of the OUT is shown in Fig. 5.1 (a). The scatterer is embedded in the fibroglandular tissue. In its turn, the fibroglandular tissue is embedded in the transitional tissue, which is surrounded

by fat. The thicknesses of the three types of tissue layers are d_1, d_2, and d_3, respectively. The length of the model is H. The width (along x) of the model is W. The value of the shape parameters used in the models are listed in Table 5.1. The radius R of the scatterer is set to 2.0 mm. The Tx/Rx antennas (shown as black dots) are modeled with short dipoles which are oriented along z. The scanning step size is h = 3 mm. The constitutive parameters (relative permittivities and conductivities) of the scatterer (tumor simulant), fibroglandular tissue, transitional tissue, and fat are set to ε_{sc} = 20, σ_{sc} = 12 S/m; ε_{fb} = 10.4, σ_{fb} = 6.1 S/m; ε_{tran} = 8.52, σ_{tran} = 4.5 S/m; and ε_{fat} = 1.09, σ_{fat} = 0.3 S/m, respectively.

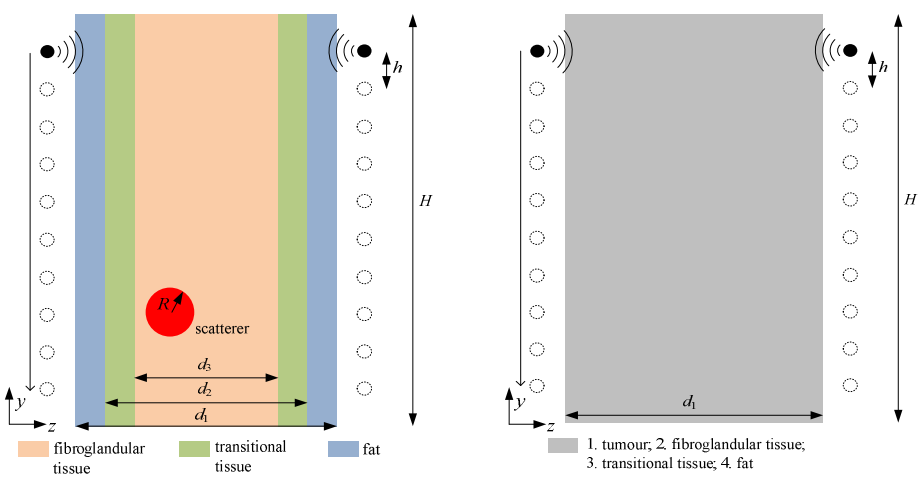

(a) (b)

Fig. 5.1 2D cross section passing through the scatterer of the 3D model of the layered structure: (a) OUT; (b) RO.

TABLE 5.1
PARAMETERS USED IN THE LAYERED STRUCTURE MODEL.

parameter	length (mm)	parameter	length (mm)
H	120 mm	d_1	20 mm
h	5 mm	d_2	16 mm
W	60 mm	d_3	12 mm

The RO has the same dimensions as the OUT and its homogeneous background medium properties are chosen to match one of the tissues in the OUT: i) fibroglandular tissue; ii) transitional tissue; iii) fat tissue; or iv) malignant tissue. Both the OUT and the RO models are simulated using the full-wave EM simulator FEKO [10]. The frequency range is from 3 GHz to 10 GHz with a sampling interval of 0.5 GHz.

The reconstructed images using different RO models are shown in Fig. 5.2. The target is detected in the first three RO scenarios and detection fails in the tumor-tissue background RO scenario. The image obtained with a fibroglandular-tissue background has the least localization error. This is consistent with the fact that in the OUT the target is indeed embedded in the fibroglandular-tissue layer.

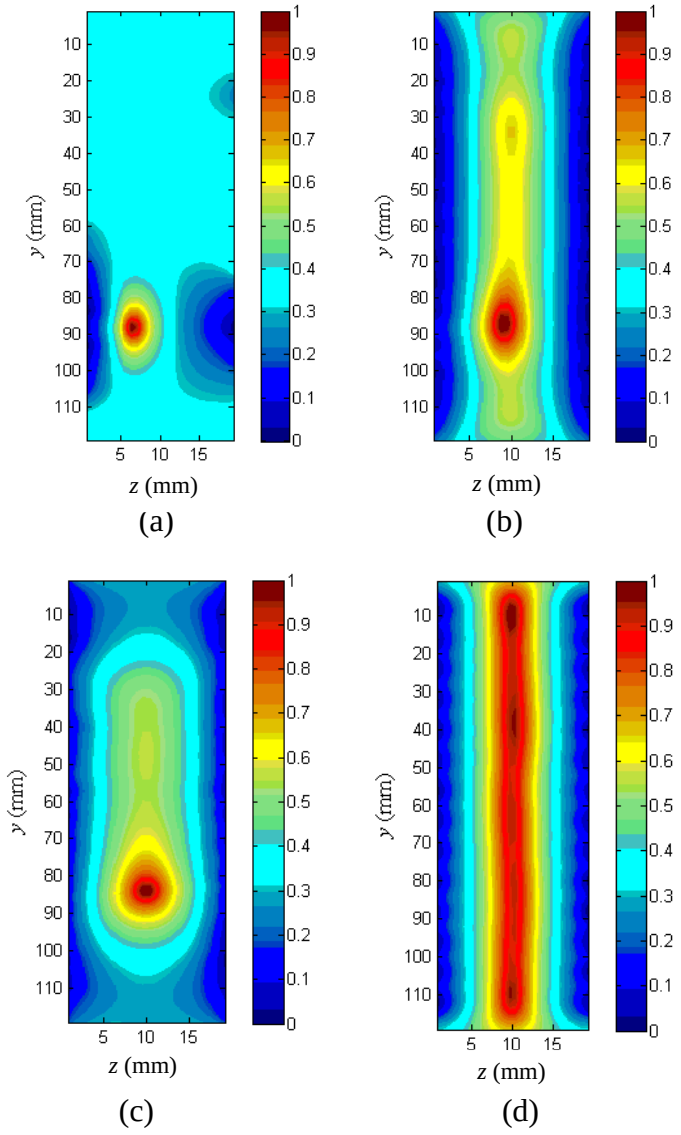

Fig. 5.2 Reconstructed images of the layered structure with a spherical tumor simulant using ROs of different homogeneous backgrounds: (a) fibroglandular tissue, P_s'(6.5, 89.0) mm; (b) transitional tissue, P_s' (9.0, 88.0) mm; (c) fat tissue, P_s'(10.0, 84.0) mm; and (d) tumor. Here, P_s' denotes the estimated location of the target. The true location of the target: P_s(7.5, 90.0) mm.

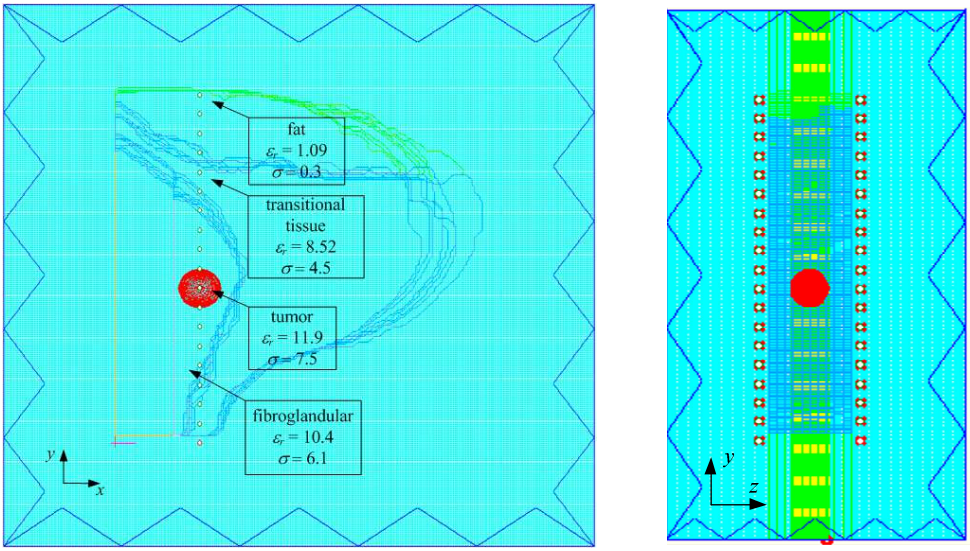

(a) (b)

Fig. 5.3 Heterogeneous human breast tissue model with tumor simulant (i.e., the OUT): (a) *xy*-view; (b) *yz*-view.

5.2.2 Complex breast tissue structure

In this example, a magnetic resonance imaging (MRI) based numerical model of the breast (as shown in Fig. 5.3) is simulated using the FDTD based EM software QW-3D [11]. The thickness (along the *z*-direction) of the breast model is 22 mm. A tumor simulant with radius of R = 2.0 mm is embedded in the fibroglandular tissue. The constitutive parameters based on those reported in [1] are also shown in Fig. 5.3. These constitutive parameters are scaled down from the actual values of the respective tissues; however, the contrast in these values is preserved. The lower permittivities allow for larger FDTD discretization cells which results in faster computation. Also, in order to keep the computational resources at a reasonable level, the skin layer is not included in the model since it requires a very thin layer surrounding the breast tissue.

The frequency band is from 3.0 GHz to 10.0 GHz with a sampling step of 0.1 GHz. The FDTD mesh is 0.5 mm for the air background. The step size of the raster scanning is 5 mm along the *y*-axis.

Similar to the previous example (subsection 5.2.1), four types of homogeneous background ROs are used in this example: i) fibroglandular-tissue RO; ii) transitional-tissue RO; iii) fat-tissue RO; and iv) tumor-tissue RO.

The reconstructed images are shown in Fig 5.4. The target is detected in the images obtained with fibroglandular and transitional-tissue ROs. The localization error is the least in the former scenario as shown in Fig. 5.4 (a). Note that the tumor simulant in the OUT is indeed embedded in the fibroglandular tissue. The image is less reliable with significant localization errors in the images obtained with the fat and the tumor background ROs.

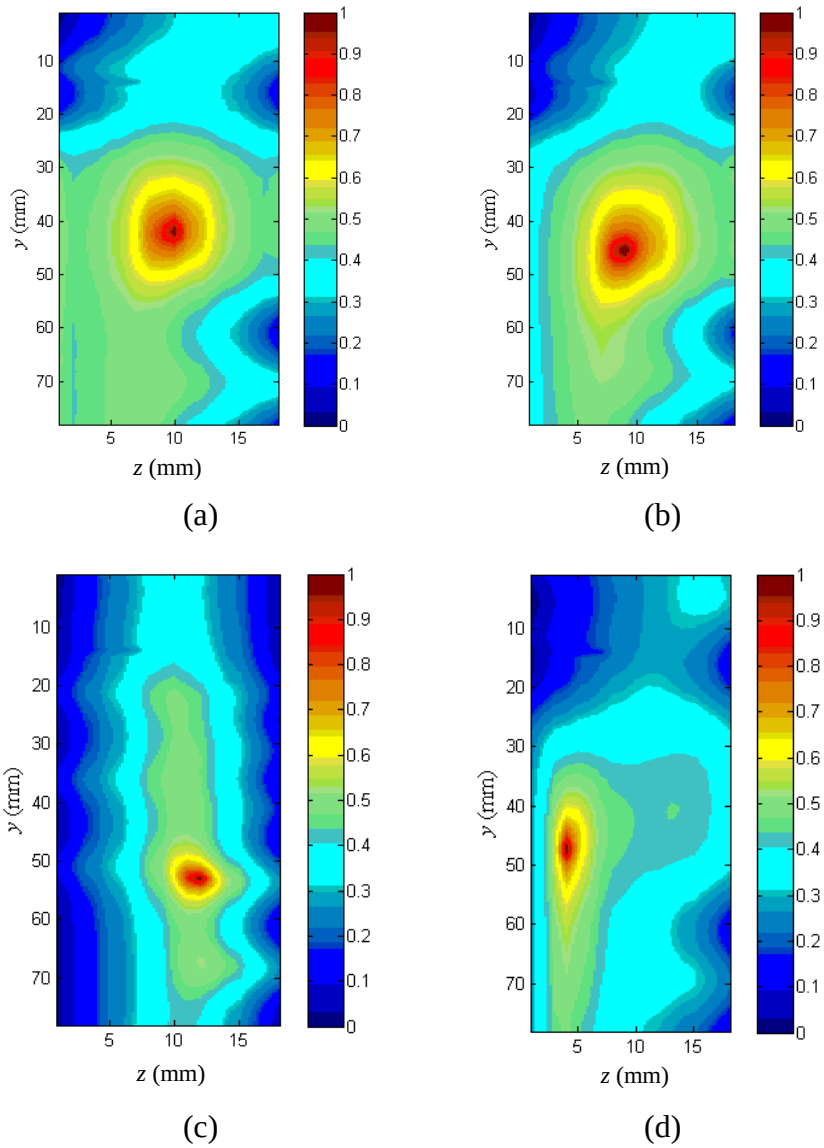

Fig. 5.4 Reconstructed images of the breast tumor using homogeneous background RO with four types of material properties: (a) fibroglandular tissue, P_s' (10.0, 41.5) mm; (b) transitional tissue, P_s'(8.5, 45.5) mm; (c) fat, P_s'(12.0, 52.5) mm; and (d) tumour, P_s'(4.0, 48.0) mm. The true location is P_s(10.0, 40.0) mm.

In both examples presented above, we observe that the reconstructed image is the most reliable (least localization error) when the homogeneous background of the RO is assumed to be fibroglandular tissue, i.e., the medium in the OUT that the scatterer is actually embedded in. In other homogeneous-background ROs, the image becomes less reliable as its assumed permittivities/conductivities deviate significantly from those of the fibroglandular tissue.

It is important to note that the preliminary study presented in this section only provides initial observations based on comparing visually the image quality. Significant and systematic future work is needed to uncover a conclusive guideline of a proper selection of the RO background medium.

5.3 PHYSICAL HUMAN-TISSUE PHANTOM

The box-shaped phantom with two identical horn antennas and their scanning route are shown in Fig 5.5. During scanning, the two antennas move together over the data acquisition plane (*xy*-plane). The thickness of the phantom is denoted as *t*.

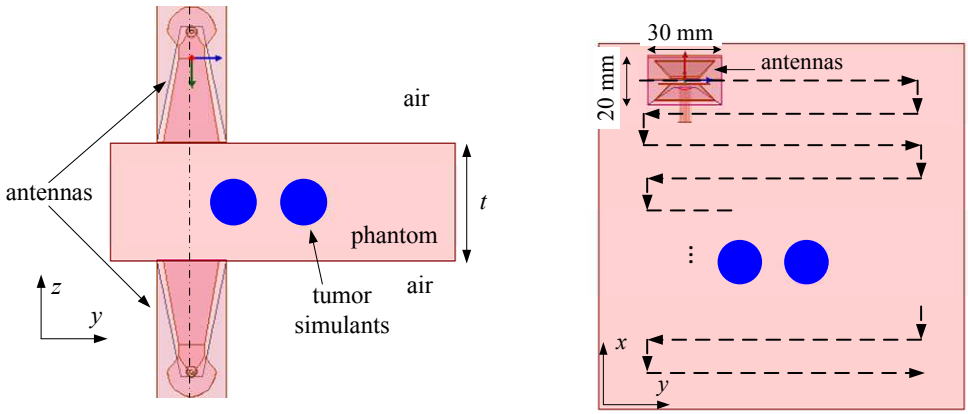

(a) (b)

Fig. 5.5 The planar raster scanning setup with two antenna where an example phantom contains two embedded tumor simulants [9]: (a) side view, (b) top view. Dashed lines represent the route of the scan (not to scale).

5.3.1 Object under test 1: double target with separation $l \approx 50$ mm.

Here, a homogeneous flat phantom made of glycerin-based material with thickness t = 30 mm is used. Two cubical tumor simulants are embedded in the phantom. We denote the two targets as Scatterer 1 and Scatterer 2. Their edges are 10 mm and 15 mm long, respectively. The separation is $l \approx 50$ mm and they are located at (25, 75, 15) mm and (35, 30, 15) mm. Scatterer 1 is made of alginate powder and Scatterer 2 is made of glycerin. The dispersive constitutive parameters of the two tumor simulants and the background medium are given in Fig. 5.6 (see curves denoted as Sc1 and Sc2) [6].

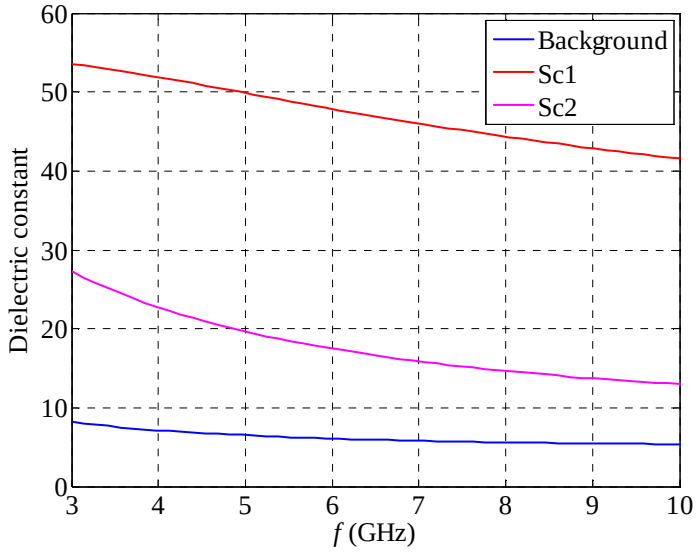

(a)

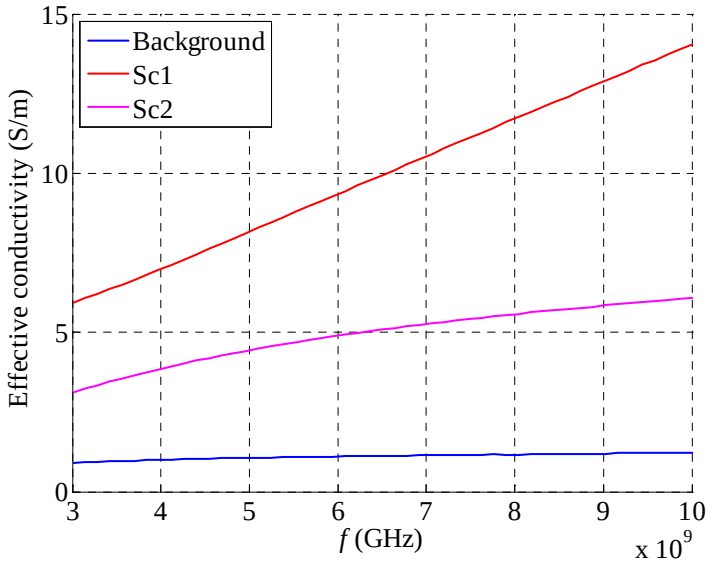

(b)

Fig. 5.6 Constitutive parameters of phantoms: (a) dielectric constant; and (b) effective conductivity. (Figures is from [6].)

5.3.2 Object under test 2: double target with distance l = 15 mm.

In this example, a homogeneous flat phantom is made of the same background material (see "Background" curve in Fig. 5.6). Its thickness is t = 50 mm. Two identical cubical tumor simulants made of alginate powder are embedded in the phantom. Their edge lengths are 10 mm. The center-to-center separation is $l \approx 15$ mm (or l' = 5 mm from surface to surface). The dispersive constitutive parameters of the two tumor simulants are given in Fig. 5.6 (see curves denoted as Scatterer1).

5.3.3 Reference object

As has been stated in Chapter 4, two types of data are needed from the RO: (i) the responses S_{RO}, and (ii) the incident field $\mathbf{E}_{\mathrm{RO}}$. In this study, we choose the RO to be the same as their respective OUT with the same setup except that there is no embedded scatterer(s). The responses S_{RO} are measured from the RO.

The incident field distribution can be obtained in two ways: i) through simulation; or ii) through measurement with a field probe if the object is mechanically penetrable. To perform the measurement, field probes mounted on robot are used. However, this is not practical in human tissue imaging which is our ultimate goal of this study. Therefore, in this thesis, we use full wave EM simulator FEKO [10] to obtain the **E**-field distribution in the RO.

5.4 RASTER SCANNING SYSTEM SETUP

5.4.1 Imaging sensor: antenna

In both the OUT and the RO, two identical TEM horn antennas [8][9] are used as a transmitting and a receiving antenna. The input impedance is matched from 3 GHz to 10 GHz. The antenna is covered with copper sheets to ensure the coupling of all available power into tissue. This also eliminates interference from the outside environement and minimizes leakage of power away from the tissue.

The antenna is filled with high-permittivity low-loss dielectric material, the permittivity of which ($\varepsilon_{\mathrm{r}} = 10$ and $\tan\delta \leq 0.002$) is similar to that of the background medium of the phantoms. Thus, the reflection at the interface between the antenna aperture and the phantom is reduced.

5.4.2 Scanning aperture setup

The photo of the scanning system and the phantom is shown in Fig. 5.7 [12]. The two TEM horn antennas are used to perform a 2D scan of the phantom slightly compressed with two thin plexiglass sheets. A slight compression of the breast phantom between two rigid parallel plates would prevent undesired movement during the microwave measurements. The *S*-parameters at the two antenna terminals are measured with Advantest R3770 vector network analyzer on an area of 100 mm $\times$ 60 mm in the OUT 1 and 70 mm $\times$ 70 mm in the OUT 2. The sampling step is $h = 5$ mm in both *x* and *y* directions.

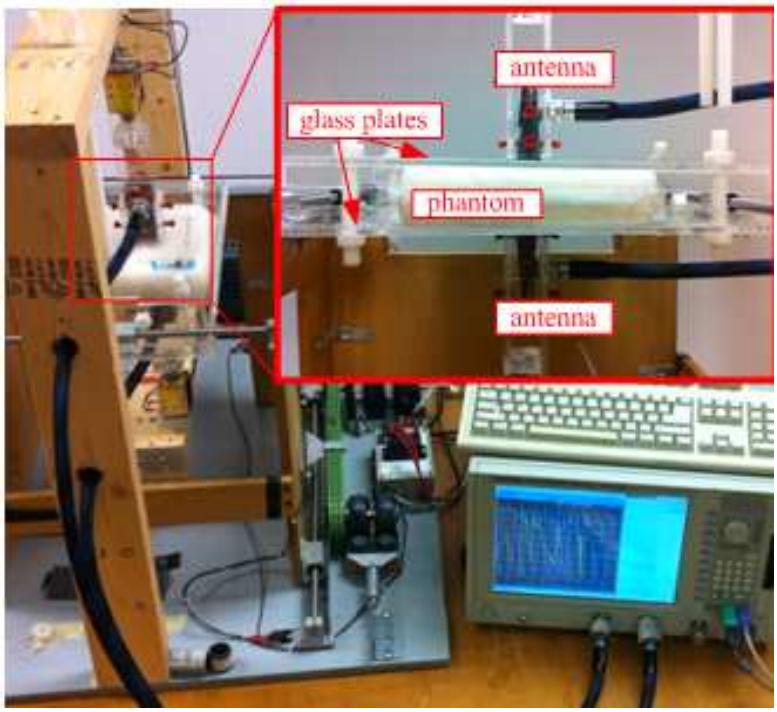

Fig. 5.7 Photo of the raster scanning measurement system. (Figure is from [12].)

5.5 RECONSTRUCTED IMAGES USING MEASURED DATA

Due to limited SNR in the reflection coefficients with our current data acquisition system, we use only the transmission coefficients for image reconstruction. As discussed in Chapter 4, the range resolution cannot be achieved when only the transmission coefficients are available. Therefore, in this chapter, the reconstructed images are 2D in nature showing the projection of the targets on the scanning plane.

Here, to obtain the image value at a certain pixel at (x, y), we only use the responses acquired at that pixel and at its adjacent pixels; i.e., we use the responses at

(x, y), $(x-h, y)$, $(x+h, y)$, $(x, y-h)$, $(x, y+h)$, $(x-h, y-h)$, $(x-h, y+h)$, $(x+h, y+h)$, and $(x+h, y-h)$. This forms a 3 by 3 "window" in the scanning plane as illustrated in Fig. 5.8. The size of the window affects the image quality, i.e., as the size becomes larger, the targets become less resolvable. This is because the value of the response Jacobian at a given voxel becomes less accurate due to noise when using responses far from the imaged pixel.

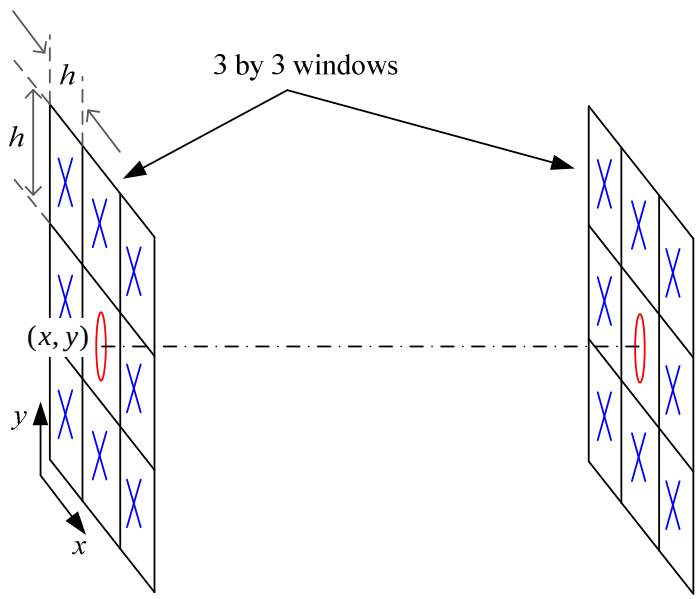

Fig. 5.8 Illustration of the 3 by 3 "window" for choosing the responses used to form the image value at the (x, y) pixel.

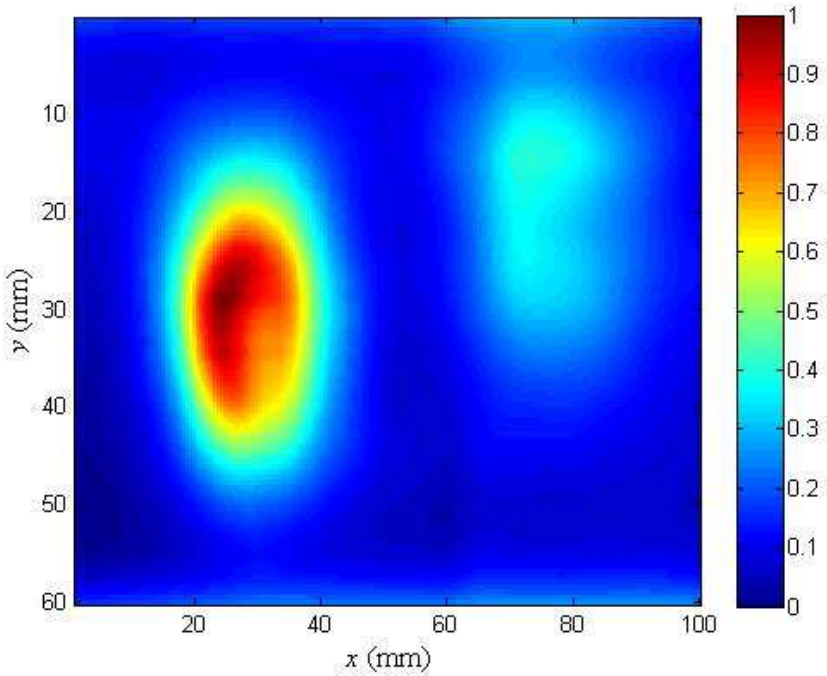

Fig. 5.9 Reconstructed image of OUT 1 (l = 50 mm).

5.5.1 Imaging object under test 1 (l = 50 mm)

The image of the double-tumor simulant is shown in Fig. 5.9. It is a 2D image slice at z = 15 mm, i.e., to obtain this image the incident field at z = 15 mm has been used.

It is observed that Scatterer 1 is significantly brighter (more observable) than Scatterer 2 in Fig. 5.9. This reflects the fact that the permittivity/conductivity contrast between Scatterer 1 and the background medium is stronger than that of Scatterer 2. It also reveals that the imaging method is more sensitive to the target-background contrast than to the size of the target.

5.5.2 Imaging object under test 2 (l = 15 mm)

The double-tumor simulant is successfully detected and the image is shown in Fig. 5.10 as a 2D image slice at z = 25 mm. The result also demonstrates the capability of the imaging method to resolve details the size of which is about l = 15 mm $(\approx 1.1\lambda_c)$. This result is expected according to the theoretical derivation in Chapter 4 where the cross-range resolution is obtained as $R_{\Delta}^{\mathrm{CR}} = 0.6\lambda_c$. However, in this imaging example, the method's performance is limited by the following factors: (i) measurement noise from the environment and the instrument; (ii) uncertainties in the scanning system due to mechanical vibration and sensor positioning; (iii) limited sensitivity of the sensor due to its large aperture. The performance of the sensitivity-based method is expected to improve by improving the hardware and addressing the problems stated above.

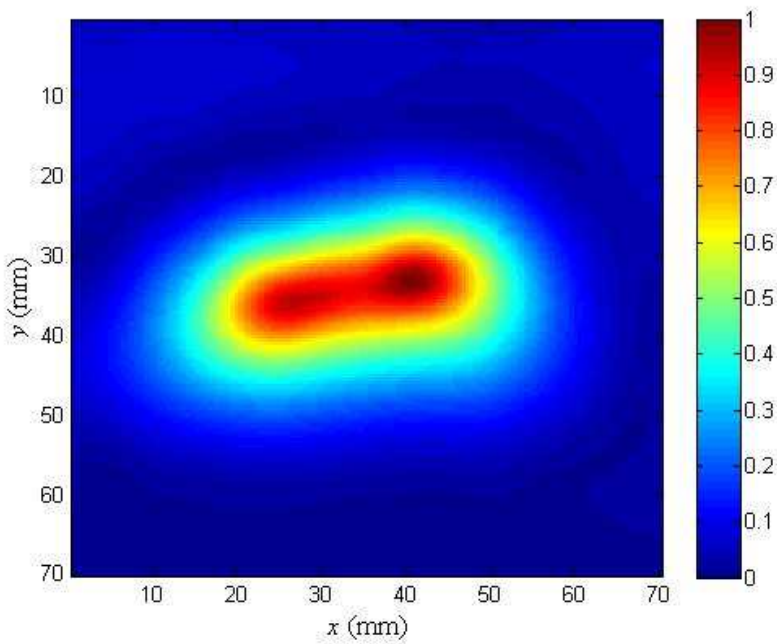

Fig. 5.10 Reconstructed image of OUT 2 (l = 15 mm).

It should also be noted that with simulated data, the sensitivity-based imaging method is able to detect tumor simulants with low tumor-to-background contrast (about 1.1:1) which has been reported in [13][14]. Due to the fact that our data acquisition system does not have sufficient sensitivity to obtain reliable strong signals with such low contrast, we work with higher contrast targets in measurements. The typical contrast of the tumor simulants used in our measurement are about 4:1 in permittivity and conductivity at the center frequency.

5.6 CONCLUSION

Imaging results using measured and simulated microwave signals (frequency-sweep) are presented. The data acquisition uses planar raster scanning. The technique features real-time image reconstruction because the required incident-field information from the electromagnetic simulations of the RO is already available.

The preliminary study of the image reconstruction using inexact ROs is performed based on numerical models. The background medium of the OUT is heterogeneous containing three different tissue layers. We observe that the image is the most reliable when the homogeneous-background RO is chosen to have the properties of the medium (material) in which the tumor simulant in the OUT is actually embedded.

In the image reconstruction with measured data of tissue phantoms, the technique has shown promise in detecting targets as small as 1 cm^3 with contrast from about 2:1 to 4:1. The difference in contrast between targets is also qualitatively reflected in the reconstructed image. The cross-range resolution of the imaging method with the current

data acquisition system and with simulated incident field information is about 15 mm. The results further confirm that range resolution is not achievable when only transmission coefficients are available in planar scanning.

The performance of the imaging method using measured data is expected to improve by reducing the noise and uncertainties of the measurements as well as improving of the sensor sensitivity.

REFERENCES

[1] L. Liu, A. Trehan, and N. K. Nikolova, "Near-field detection at microwave frequencies based on self-adjoint response sensitivity analysis," *Inverse Problems*, vol. 26, 105001, 2010.

[2] Li Liu, A. Trehan, and N.K. Nikolova, "Detection using microwaves and self-adjoint sensitivity analysis," XX URSI Comm. B Int. Symp. on Electromagnetic Theory (EMT-S) 2010, Aug. 2010, pp. 589–592.

[3] Y. Zhang, L. Liu, and N. K. Nikolova, "Resolution study for detection algorithm based on self-adjoint sensitivity analysis with microwave responses," *The 27th Annual Review of Progress in Applied Computational Electromagnetics (ACES 2011)*, Mar. 2011.

[4] Y. Zhang, L. Liu, and N.K. Nikolova, “Sensitivity-based imaging with near-zone microwave raster scanning,” *The 8th European Radar Conference (EuRAD) 2011*, Oct. 2011.

[5] Y. Zhang, S. Tu, R. K. Amineh and N. K. Nikolova, “Resolution and robustness to noise of the sensitivity-based method for microwave imaging with data acquired on cylindrical surfaces,” *Inverse Problems*, vol. 28, 115006, 2012.

[6] A. Trehan, “Numerical and physical models for microwave breast imaging,” M.A.Sc. Thesis, McMaster University, Hamilton, Canada, 2009.

[7] Y. Baskharoun, A. Trehan, N. K. Nikolova, and D. Noseworthy, “Physical phantoms for microwave imaging of the breast,” *IEEE BioWireleSS*, Jan. 2012.

[8] R. K. Amineh, M. Ravan, N. K. Nikolova, and A. Khalatpour, “Three-dimensional near-field microwave holography using reflected and transmitted signals,” *IEEE Trans. Antennas Propag*. vol. 59, pp. 4777–4789, 2011.

[9] R. K. Amineh, M. Ravan, A. Trehan, and N. K. Nikolova, “Near-field microwave imaging based on aperture raster scanning with TEM horn antennas,” *IEEE Trans. Antennas Propag*., vol. 59, no. 3, pp. 928–940, Mar. 2011.

[10] FEKO, *Suite 6.0*, EM Software & Systems, Inc., USA, 2010.

[11] QuickWave-3D ver. 7.0, QWED Sp. z o.o.ul., Nowowiejska 28 lok. vol. 32, 02-010, Warsaw, Poland.

[12] H. Xu, “Planar raster-scanning for near-field microwave imaging,” M.A.Sc. Thesis, McMaster University, Hamilton, Canada, 2011.

[13] C. Gabriel, “The dielectric properties of biological tissues. I. literature survey,” *Phys Med Biol*, vol. 41, pp. 2231–49, 1996.

[14] M. Lazebnik, D. Popovic, L. McCartney, C. B. Watkins, M. J. Lindstrom, J. Harter, S. Sewall, T. Ogilvie, A. Magliocco, T. M. Breslin, W. Temple, D. Mew, J. H. Booske, M. Okoniewski, and S. C. Hagness, "A large-scale study of the ultrawideband microwave dielectric properties of normal, benign, and malignant breast tissues obtained from cancer surgeries," *Physics in Medicine and Biology*, vol. 52, pp. 6093-6115, 2007.

Chapter 6

CONCLUSIONS

This thesis presents advanced applications of the self-adjoint *S*-parameter sensitivity analysis. In the application to antenna design optimization based on the method of moments (MoM), the proposed technique aims at providing fast and accurate response sensitivities. In the sensitivity-based imaging, the technique allows for real-time image reconstruction. The studies of the method's resolution limits and robustness to noise are performed here for the first time. Also, our first attempts at image reconstruction using measured microwave data are reported.

In Chapter 2, the mathematical basis of *S*-parameters sensitivity analysis based on a self-adjoint approach is presented. The formulation of the sensitivity expression using the MoM current solution based on specific EM solver (FEKO) is given. Then, the sensitivity formula using volumetric field solution is presented. In both formulations, the computation of the sensitivity information is accelerated significantly because the analysis of the adjoint problem is avoided. This becomes possible due to the self-adjoint nature of the linear electromagnetic problem, which allows for a simple linear relationship between the original and the adjoint problems in the case of network-parameter responses such as *S*-parameters.

Chapter 3 presents the application of the *S*-parameters sensitivity analysis with MoM solutions to design optimization. The self-adjoint approach is implemented with discrete shape perturbations on a non-uniform grid. The design optimization of a planar printed antenna and a microwave double-stub tuner are used as validation examples. The gradient-based optimization is accelerated due to the use of discrete shape perturbations and the availability of computationally cheap sensitivity information.

In Chapter 4, the resolution limits and the noise robustness of a new sensitivity-based imaging method are studied using data acquired with two common approaches: (i) planar raster scanning; and (ii) circular sensor array. The analytical EM models of the incident and the scattered field are derived where the latter is based on the linear Born approximation. The spatial resolution limits are derived from the analytical point-spread function (PSF) of the method and are then validated with double-scatterer imaging examples. In both data acquisition approaches, the far-zone resolution limits are related to the minimum wavelength, while the near-zone resolution limits are related to the distance between transmitting and receiving sensors. In addition, in the case of planar raster scanning, the cross-range resolution limit is also a function of the aperture angle. Finally, the method's robustness to noise with respect to spatial and frequency sampling rates is studied. The image quality improves as the spatial and frequency sampling rates increase, which is expected.

Chapter 5 presents the imaging of numerical and physical tissue phantoms. Preliminary study on imaging without the exact knowledge of the normal state of the object is also performed with simulated data. Reference objects (RO) with various

homogeneous background media are tested. We observe that the image of the object under test (OUT) is visually the best when the RO is assumed to be made of the homogeneous medium where the scatterer is actually embedded. Further, the imaging is for the first time tested with measured data of tissue phantoms. The technique has shown promise in detecting targets of size 1 cm^3 with the target-to-background contrast from about 2:1 to 4:1. It is able to resolve targets at separation of 15 mm with the current raster scanning acquisition system. In addition, it is observed that the difference in contrast between targets is qualitatively reflected in the reconstructed images.

From the experience gained during the course of this work, the author suggests the following research topics to be addressed in future developments.

(1) Enhancing the sensitivity-based imaging technique using iterative updates of the incident field information, thus, overcoming the limitations of the linear Born approximation.

(2) Developing methods for noise suppression in the microwave measured data.

(3) Investigating algorithms for data fusion of the images reconstructed at various sampled frequencies. Data fusion algorithms can also be used to combine the outcome of the sensitivity-based reconstruction method (which operates directly in the spatial domain) and the holography reconstruction (which operates in *k*-space) [1].

(4) Building circular and hemi-spherical sensor-array acquisition systems which allow for obtaining more responses from varying viewing angles.

(5) Investigating the possibility to acquire the incident field and the Green tensor via measurements instead of simulations of the RO.

(6) Designing an antenna able to acquire reliable reflected signal by further reducing the reflection at the interface between the antenna and phantom. Improving the antenna sensitivity by reducing the effective area.

(7) Systematic study of imaging without exact background medium information of the OUT.

REFERENCES

[1] M. Ravan, R. K. Amineh, and N. K. Nikolova, "Two-dimensional near-field microwave holography," *Inverse Problems*, vol. 26, 2010.

APPENDIX

A1. SIMPLIFICATION OF POINT SPREAD FUNCTION (PSF)

To simplify the discussion, we observe the image reconstructed in the *xz* plane defined by the 1-D scanning route of the two sensors. The target is located at the origin of this plane (see Fig. A.1). Now, the imaging formula (4.41) in Chapter 4 using single frequency data can be re-written as

$$D^{(m)}\left(\boldsymbol{r}'\right) = -\int_{-H/2}^{+H/2} \sum_{i,j=1}^{2} \mathrm{Re}\left\{\left[P^{(m)}\left(\boldsymbol{r}_0\right)\right]^* P^{(m)}\left(\boldsymbol{r}'\right)\right\} \mathrm{d}x,\ m = 1,\ldots,N_f. \tag{A.1}$$

Here,

$$P^{(m)}(\boldsymbol{\rho}) = -\mathrm{i}\cdot \mathbf{E}_{\mathrm{RO},j}^{(m)}(\boldsymbol{\rho})\cdot \mathbf{E}_{\mathrm{RO},k}^{(m)}(\boldsymbol{\rho}),\quad \boldsymbol{\rho} \equiv \boldsymbol{r}_0, \boldsymbol{r}'. \tag{A.2}$$

We first assume the distance between the two scanning plane is infinite, i.e., $D \to \infty$, the wave propagation factor can be simplified as

$$E^{(m)}(r) \sim e^{-\mathrm{i}k_m r}. \tag{A.3}$$

Here, r is the distance between the transmitting antenna and the observation point. Using (A.3), (A.1) can be obtained as

$$D^{(m)}\left(\boldsymbol{r}'\right) = -\int_{-H/2}^{+H/2} \sum_{j,k=1}^{2} \mathrm{Re}\left[\left(e^{-\mathrm{i}k_m r_{0j}} e^{-\mathrm{i}k_m r_{0k}}\right)^* \left(e^{-\mathrm{i}k_m r_{Pj}} e^{-\mathrm{i}k_m r_{Pk}}\right)\right] \mathrm{d}x. \tag{A.4}$$

Here, $r_{0\xi},\ \xi = j,k$ are the distances between the scatterer and the *j*-th/*k*-th antenna; $r_{P\xi},\ \xi = j,k$ are the distances between the observation point and the *j*-th/*k*-th antenna.

The above equation is then used in the derivation of the PSFs when only reflection or transmission coefficients are available.

A2. POINT SPREAD FUNCTION IN THE RANGE DIRECTION OBTAINED USING REFLECTION COEFFICIENTS

In the case where only reflection coefficients are available, i.e., we use the response differences ΔS_{11} and ΔS_{22}, the PSF in (A.4) can be written as

$$\begin{aligned} D^{(m)}(\boldsymbol{r}') &= -\int_{-H/2}^{+H/2} \mathrm{Re}\begin{bmatrix} \left(e^{-\mathrm{i}k_m r_{01}} e^{-\mathrm{i}k_m r_{01}}\right)^* \left(e^{-\mathrm{i}k_m r_{P1}} e^{-\mathrm{i}k_m r_{P1}}\right) \\ +\left(e^{-\mathrm{i}k_m r_{02}} e^{-\mathrm{i}k_m r_{02}}\right)^* \left(e^{-\mathrm{i}k_m r_{P2}} e^{-\mathrm{i}k_m r_{P2}}\right) \end{bmatrix} \mathrm{d}x \\ &= -\int_{-H/2}^{+H/2} \begin{Bmatrix} \left[\sin(2k_m r_{01})\sin(2k_m r_{P1}) + \cos(2k_m r_{01})\cos(2k_m r_{P1})\right] \\ +\left[\sin(2k_m r_{02})\sin(2k_m r_{P2}) + \cos(2k_m r_{02})\cos(2k_m r_{P2})\right] \end{Bmatrix} \mathrm{d}x. \end{aligned} \tag{A.5}$$

Since the target is located at the origin of the coordinate system, we have

$$r_{01} = r_{02}\,. \tag{A.6}$$

Substituting (A.6) into (A.5), we have

$$D^{(m)}(\boldsymbol{r}') = -2\int_{-H/2}^{+H/2} \cos\left[k_m(r_{P1} - r_{P2})\right] \begin{Bmatrix} \sin(2k_m r_{01})\sin\left[k_m(r_{P1} + r_{P2})\right] \\ +\cos(2k_m r_{01})\cos\left[k_m(r_{P1} + r_{P2})\right] \end{Bmatrix} \mathrm{d}x. \tag{A.7}$$

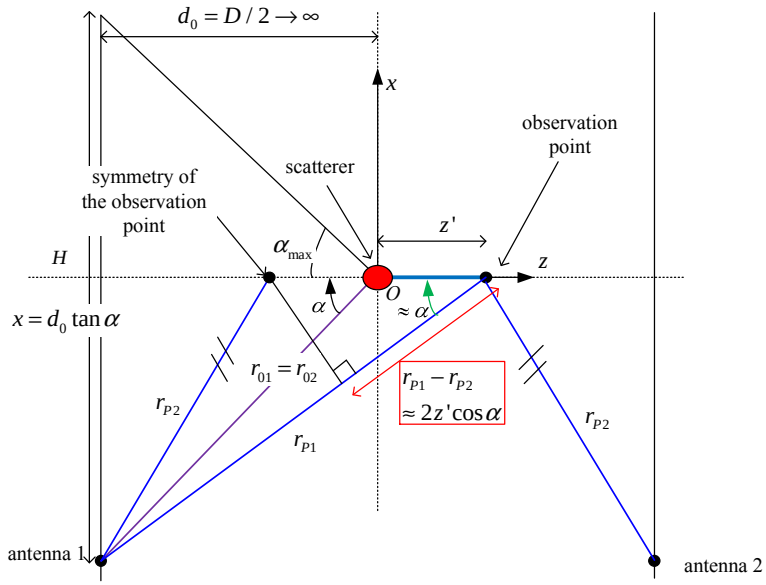

Fig. A.1 Observing along the range direction.

Since the scanning antennas are very far from the target, we have (see Fig. A.1)

$$r_{P1} + r_{P2} \approx 2r_{01} = 2r_{02} \tag{A.8}$$

and

$$r_{P1} - r_{P2} \approx 2z'\cos\alpha\,. \tag{A.9}$$

Substituting (A.8) and (A.9) into (A.7), we have

$$D^{(m)}(z') = -2\int_{-H/2}^{+H/2} \cos\left(2k_m z'\cos\alpha\right)\mathrm{d}x. \tag{A.10}$$

(A.10) can also be written as

$$D^{(m)}(z') = -2d_0\int_{-\alpha_{\max}}^{\alpha_{\max}} \frac{1}{\cos^2\alpha}\cos\left(2k_m z'\cos\alpha\right)\mathrm{d}\alpha. \tag{A.11}$$

The solution of (A.11) becomes trivial by assuming very small scanning angle where

$$\alpha \in \left(-\alpha_{\max},\ \alpha_{\max}\right), \qquad \alpha_{\max} \to 0\,. \tag{A.12}$$

Using (A.12) and Taylor expansion, (A.11) can be obtained as

$$\begin{aligned} D^{(m)}\left(z'\right) &\approx -2d_0 \int_{-\alpha_{\max}}^{\alpha_{\max}} \frac{1}{\cos^2\alpha} \cos\left(2k_m z'\right) \mathrm{d}\alpha \\ &= -2d_0 \cos\left(2k_m z'\right) \tan\alpha \Big|_{-\alpha_{\max}}^{\alpha_{\max}} \\ &\approx -4d_0 \alpha_{\max} \cos\left(2k_m z'\right). \end{aligned} \tag{A.13}$$

This is the PSF in the range direction when using only the reflection coefficients at a single frequency.

The resolution is defined as the width at half of the maximum value (indicating center of the scatterer) of the PSF, thus we have the following relation:

$$\left| \frac{D^{(m)}\left(z'\right)}{D^{(m)}(0)} \right| = \frac{1}{2}\,. \tag{A.14}$$

Solving (A.14), we have

$$2k_m z' = \pm\frac{\pi}{3} \pm n\pi, \quad n = 0,1,\ldots,N \tag{A.15}$$

and

$$R_{\Delta 1}^{\mathrm{R}} = \left|2z'\right| = \frac{\lambda_m}{6}, \ \text{ when } n = 0\,. \tag{A.16}$$

The obtained range resolution is consistent with the theoretical resolution limit obtained by calculating (4.41) at a single sampled frequency when $\alpha_{\max}$ is very small.

(A.16) also shows that when using small scanning planes, the range resolution is not a function of $\alpha_{\max}$ but of the wavelength which is also consistent with our observations in Section 4.8.

A3. POINT SPREAD FUNCTION IN THE CROSS-RANGE DIRECTION OBTAINED USING REFLECTION COEFFICIENTS

In this case, we have (see Fig. A.2)

$$r_{P1} + r_{P2} \approx 2r_{01} - 2x'\sin\alpha \tag{A.17}$$

and

$$r_{P1} - r_{P2} = 0\,. \tag{A.18}$$

Substituting (A.17) and (A.18) into (A.7), we have

$$\begin{aligned} D^{(m)}(x') &= -2\int_{-H/2}^{+H/2} \cos\left(2k_m r_{01} - k_m(r_{P1} + r_{P2})\right)\mathrm{d}x \\ &\approx -2\int_{-H/2}^{+H/2} \cos\left(2k_m \sin\alpha\right)\mathrm{d}x. \end{aligned} \tag{A.19}$$

(A.19) can also be written as

$$D^{(m)}(x') = -2d_0\int_{-\alpha_{\max}}^{\alpha_{\max}} \frac{1}{\cos^2\alpha}\cos\left(2k_m x'\sin\alpha\right)\mathrm{d}\alpha. \tag{A.20}$$

This is the PSF in the cross-range direction when using only reflection coefficients at single frequency.

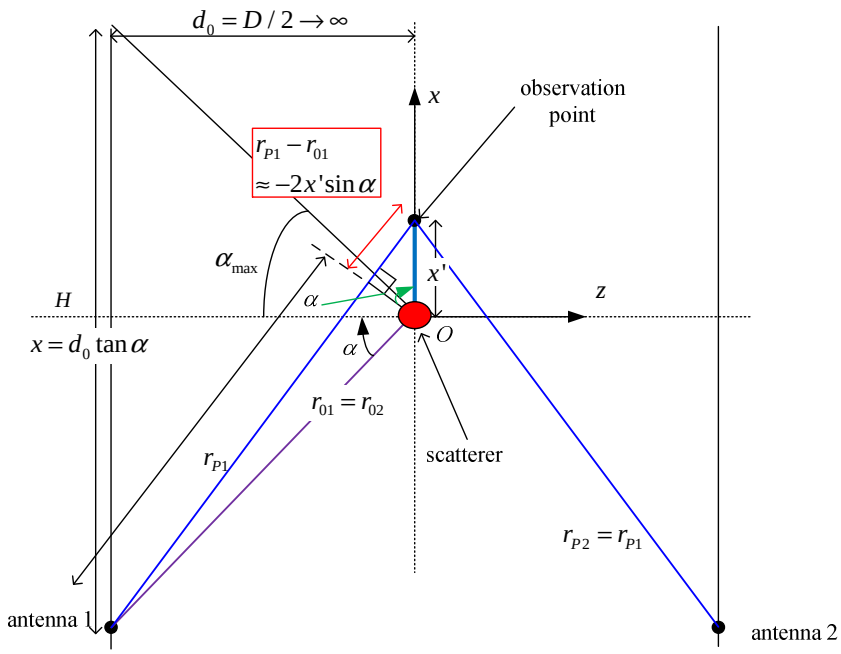

Fig. A.2 Observing along the cross-range direction.

By using (A.12) and Taylor expansion, (A.20) can be obtained as

$$\begin{aligned} D^{(m)}(x') &\approx -2d_0 \int_{-\alpha_m}^{\alpha_m} \left(1+\sin^2\alpha\right)\cos\left(2k_m x'\sin\alpha\right)\mathrm{d}\alpha \\ &\approx -2d_0 \int_{-\alpha_m}^{\alpha_m} \left(1+\alpha^2\right)\cos\left(2k_m x'\left(\alpha - \frac{\alpha^3}{6}\right)\right)\mathrm{d}\alpha \\ &\approx -2d_0 \int_{-\alpha_m}^{\alpha_m} \left(1+\alpha^2\right)\left[1-\frac{1}{2}\left(2k_m x'\left(\alpha - \frac{\alpha^3}{6}\right)\right)^2\right]\mathrm{d}\alpha \\ &\approx -4d_0\left[\alpha_{\max} - \frac{1}{3}\alpha_{\max}^3\left(2k_m^2 x'^2 - 1\right)\right]. \end{aligned} \tag{A.21}$$

From the definition of the resolution limit, we have the following relation

$$\left|\frac{D^{(m)}(x')}{D^{(m)}(0)}\right| = \frac{1}{2}. \tag{A.22}$$

Solving (A.22), we have

$$R_{\Delta 1}^{\mathrm{CR}} = 2|x'| = \frac{\lambda_m}{2\pi}\sqrt{\frac{3}{\alpha_{\max}^2} + 2}. \tag{A.23}$$

The above equation shows that when a small scanning plane is used, the cross-range resolution is not only proportional to the wavelength but also is a function of $\alpha_{\max}$. Again, the conclusion is consistent with the theoretical resolution limit at single frequency when $\alpha_{\max} < 0.1\,\mathrm{rad}$. The resolution improves as $\alpha_{\max}$ increases, which is expected and it is consistent with conclusion in Section 4.8.

Note that the PSF in (A.21) and the cross-range resolution in (A.23) are identical to those obtained in the cross-range resolution using the transmission coefficients. Thus, the PSF in the latter case is not shown for brevity.

A4. POINT SPREAD FUNCTION IN THE RANGE DIRECTION OBTAINED USING TRANSMISSION COEFFICIENTS

In this case, the response difference ΔS_{12} and ΔS_{21} are used. As per (A.4), we have

$$D^{(m)}(\boldsymbol{r}') = -2\int_{-H/2}^{+H/2} \cos(k_m \Delta r)\mathrm{d}x, \tag{A.24}$$

where

$$\Delta r = (r_{01} + r_{02}) - (r_{P1} + r_{P2}). \tag{A.25}$$

It is calculated using (refer to Appendix 5)

$$\Delta r \approx -\frac{z'^2}{d_0}\sin^2\alpha\cos\alpha. \tag{A.26}$$

Substituting (A.26) into (A.24), we have

$$\begin{aligned} D^{(m)}\left(z'\right) &= -2\int_{-H/2}^{+H/2} \cos\left(\frac{k_m z'^2}{d_0}\sin^2\alpha\cos\alpha\right)\mathrm{d}x \\ &= -2d_0\int_{-\alpha_{\max}}^{\alpha_{\max}} \frac{1}{\cos\alpha^2}\cos\left(\frac{k_m z'^2}{d_0}\sin^2\alpha\cos\alpha\right)\mathrm{d}\alpha. \end{aligned} \tag{A.27}$$

This is the PSF in the cross-range direction when using only the transmission coefficients at single frequency. Since $\alpha_{\max} \to 0$, we have

$$\frac{k_m z'^2}{d_0}\sin^2\alpha\cos\alpha \to 0\,. \tag{A.28}$$

Now, using Taylor expansion, (A.27) becomes

$$\begin{aligned} D^{(m)}\left(z'\right) &\approx -2d_0\int_{-\alpha_{\max}}^{\alpha_{\max}} \frac{1}{\cos^2\alpha}\left[1-\frac{1}{2}\left(\frac{k_m}{d_0}z'^2\cos\alpha\sin^2\alpha\right)^2\right]\mathrm{d}\alpha \\ &= -4d_0\left[\tan\alpha_{\max} + \frac{k_m^2 z'^4}{d_0^2}\left(\frac{3}{16}\alpha_{\max} - \frac{\sin 2\alpha_{\max}}{8} + \frac{\sin 4\alpha_{\max}}{64}\right)\right]. \end{aligned} \tag{A.29}$$

By definition, the resolution limits is defined as the width of the PSF at half of the maximum value (indicating center of target), we have the following relationship:

$$\left|\frac{D^{(m)}\left(z'\right)}{D^{(m)}(0)}\right| = \frac{1}{2}\,. \tag{A.30}$$

Solving (A.30), we have

$$z' = 2\sqrt[4]{\frac{-2d_0^2\tan\alpha_{\max}}{k_m^2\left(12\alpha_{\max} - 8\sin 2\alpha_{\max} + \sin 4\alpha_{\max}\right)}}\,. \tag{A.31}$$

Since

$$12\alpha_{\max} - 8\sin 2\alpha_{\max} + \sin 4\alpha_{\max} > 0, \qquad \alpha_m \in \left(0,\ \pi/2\right), \tag{A.32}$$

the solution of (A.31) does not lead to a real value which indicates that the PSF with transmission coefficients does not provide range resolution. This conclusion is consistent with our results in Section 4.9 where the exact PSF is solved numerically.

A5. DISTANCE PARAMETERS USED IN CALCULATING THE PSF USING ONLY TRANSMISSION COEFFICIENTS

First, the normalized distance between antenna 1 and the observation point is calculated using

$$\begin{aligned} r_{P1} &= \sqrt{z'^2 + r_{01}^2 - 2z' r_{01} \cos\alpha} \\ &= r_{01}\sqrt{1 + \left(\frac{z'^2}{r_{01}^2} - 2\frac{z'}{r_{01}}\cos\alpha\right)}. \end{aligned} \tag{A.33}$$

Using Taylor expansion, (A.33) becomes

$$\begin{aligned} r_{P1} &\approx r_{01}\left\{1 + \frac{1}{2}\left[\left(\frac{z'}{r_{01}}\right)^2 - 2\frac{z'}{r_{01}}\cos\alpha\right] - \frac{1}{8}\left[\left(\frac{z'}{r_{01}}\right)^2 - 2\frac{z'}{r_{01}}\cos\alpha\right]^2\right\} \\ &= r_{01}\left\{1 - \frac{z'}{r_{01}}\cos\alpha + \frac{1}{2}\left(\frac{z'}{r_{01}}\right)^2 - \frac{1}{2}\left(\frac{z'}{r_{01}}\right)^2\cos^2\alpha + \frac{1}{2}\left(\frac{z'}{r_{01}}\right)^3\cos\alpha - \frac{1}{8}\left(\frac{z'}{r_{01}}\right)^4\right\}. \end{aligned} \tag{A.34}$$

Since

$$r_{01} = \frac{d_0}{\cos\alpha} \to \infty, \tag{A.35}$$

and

$$\frac{z'}{r_{01}} \to 0, \tag{A.36}$$

(A.34) can be further simplified as

$$r_{P1} = r_{01}\left[1 - \frac{z'}{r_{01}}\cos\alpha + \frac{1}{2}\left(\frac{z'}{r_{01}}\right)^2 \sin^2\alpha\right]. \tag{A.37}$$

Similarly, we obtain the formula for computing r_{P2}:

$$r_{P2} = r_{01}\left[1 + \frac{z'}{r_{01}}\cos\alpha + \frac{1}{2}\left(\frac{z'}{r_{01}}\right)^2 \sin^2\alpha\right]. \tag{A.38}$$

Therefore, from (A.37) and (A.38), we have

$$2r_{01} - (r_{P1} + r_{P2}) = -\frac{z'^2}{r_{01}}\sin^2\alpha\,. \tag{A.39}$$

Substituting (A.35) into (A.39), we have

$$\Delta r = -\frac{z'^2}{d_0}\sin^2\alpha\cos\alpha. \tag{A.40}$$

The above expression is used in calculating the distance in the case of the range-resolution study using transmission coefficients in Appendix 4.

REFERENCES

[1] C. A. Balanis, *Antenna Theory, 2nd ed.* USA: WILEY, 1997.

BIBLIOGRAPHY

A. Agurto, Y. Li, G. Y. Tian, N. Bowring and S. Lockwood, “A review of concealed weapon detection and research in perspective,” *Proc. of the IEEE Int. Conf. on Networking, Sensing and Control* pp. 443–448, 2007.

H. Akel and J. P. Webb, “Design sensitivities for scattering-matrix calculation with tetrahedral edge elements,” *IEEE Trans. Magn*., vol. 36, no. 4, pp. 1043–1046, Jul. 2000.

I. Aliferis, C. Pichot, J. Y. Dauvignac, and E. Guillanton, “Tomographic reconstructions of buried objects using a nonlinear and regularized inversion method,” *Proc. Int. Non-Linear Electromagn. Syst. Symp.*, 1999.

R. K. Amineh, M. Ravan, A. Trehan, and N. K. Nikolova, “Near-field microwave imaging based on aperture raster scanning with TEM horn antennas,” *IEEE Trans. Antennas Propag*., vol. 59, No. 3, pp. 928–940, Mar. 2011.

R. K. Amineh, M. Ravan, A. Khalatpour, and N. K. Nikolova, “Three-dimensional near-field microwave holography using reflected and transmitted signals,” *IEEE Trans. Antennas and Propag*., vol. 59, no. 12, pp. 4777−4789, 2011.

Ansoft HFSS ver. 10.1.2, Ansoft Corporation, 225 West Station Square Drive, Suite 200, Pittsburgh, PA 15219, USA, 2006, www.ansoft.com.

M. H. Bakr and N. K. Nikolova, “An adjoint variable method for frequency domain TLM problems with conducting boundaries,” *IEEE Microwave and Wireless Components Letters*, vol. 13, no. 9, pp. 408–410, Sep. 2003.

M. H. Bakr and N. K. Nikolova, “An adjoint variable method for time domain TLM with fixed structured grids,” *IEEE Trans. Microwave Theory Tech*., vol. 52, no. 2, pp. 554–559, Feb. 2004.

M. H. Bakr, N. K. Nikolova, and P. A. W. Basl, “Self-adjoint S-parameter sensitivities for lossless homogeneous TLM problems,” *Int. J. of Numerical Modelling: Electronic Networks, Devices and Fields*, vol. 18, no. 6, pp. 441–455, Nov./Dec. 2005.

C. A. Balanis. *Advanced Engineering Electromagnetics*, New York: J. Wiley & Sons,1989.

Y. Baskharoun, A. Trehan, N. K. Nikolova, and D. Noseworthy, “Physical phantoms for microwave imaging of the breast,” *IEEE BioWireleSS*, Jan. 2012.

M. Benedetti, M. Donelli, G. Franceschini, M. Pastorino, and A. Massa, “Effective exploitation of the *a priori* information through a microwave imaging procedure based on the SMW for NDE/NDT applications,” *IEEE Trans. Geosc. Remote Sens.*, vol. 43, pp. 2584-2592, 2005.

D. G. Cacuci, Sensitivity & Uncertainty Analysis, Volume 1: Theory. Boca Raton, FL: Chapman & Hall/CRC, 2003.

S. Caorsi, G. L. Gragnani, M. Pastorino, and M. Sartore, “Electromagnetic imaging of infinite dielectric cylinders using a modified Born approximation and including *a priori* information on the unknown cross sections,” *Proc. Inst. Elect. Eng.-Microw. Antennas Propag.*, vol. 141, pp. 445-450, 1994.

T. K. Chan, Y. Kuga, and A. Ishimaru, “Subsurface detection of a buried object using angular correlation function measurement,” *Waves in Random and Complex Media*, vol. 7, pp. 457–465, 1997.

S. S. Chaudhury, R. K. Mishra, A. Swarup, and J. M. Thomas, “Dielectric properties of normal and malignant human breast tissues at radiowave and microwave frequencies,” *Ind. J. Biochem. Biophys.*, vol. 21, pp. 76-79, 1984.

W. C. Chew, *Waves and Fields in Inhomogeneous Media* (NY, USA: IEEE PRESS), 1995.

W. C. Chew and J. H. Lin, "A frequency-hopping approach for microwave imaging of large inhomogeneous bodies," *IEEE Microwave Guided Wave Lett.*, vol. 5, pp. 439-441, 1995.

M. S. Dadash, N. K. Nikolova, and J. W. Bandler, "Analytical adjoint sensitivity formula for the scattering parameters of metallic structures," *IEEE Trans. Microwave Theory Tech*., vol. 60, no. 9, pp. 2713–2722, Sep. 2012.

Q. Fang, P. M. Meaney, S. D. Geimer, K. D. Paulsen, and A. V. Streltsov, "Microwave image reconstruction from 3-D fields coupled to 2-D parameter estimation," *IEEE Transactions on Medical Imaging*, vol. 23, pp. 475-484, 2004.

Q. Fang, P. M. Meaney, and K. D. Paulsen, "Singular value analysis of the Jacobian matrix in microwave image reconstruction," *IEEE Trans. Antennas Propag.*, vol. 54, pp. 2371-2380, 2006.

E. C. Fear and M. A. Stuchly, "Microwave detection of breast cancer," *IEEE Trans. Microwave Theory Tech.*, vol. 48, pp. 1854–1863, 2000.

E. Fear, X. Li, S. C. Hagness, and M. A. Stuchly, “Confocal microwave imaging for breast cancer detection: localization of tumours in three dimensions,” *IEEE Trans. Biomed. Eng.*, vol. 49, no. 8, pp. 812–822, 2001.

E. C. Fear, S. C. Hagness, P. M. Meaney, M. Okoniewski, and M. A. Stuchly, “Enhancing breast tumor detection with near field imaging,” *IEEE Microwave magazine*, vol. 3, pp. 48–56, 2002.

E. C. Fear, X. Li, S. C. Hagness, and M. A. Stuchly, “Confocal microwave imaging for breast cancer detection: localization of tumors in three dimensions,” *IEEE Trans. Biomed. Eng.*, vol. 49, pp. 812–821, 2002.

FEKO, *Suite 6.0*, EM Software & Systems, Inc., USA, 2010.

C. Gabriel, “The dielectric properties of biological tissues. I. literature survey,” *Phys Med Biol*, vol. 41, pp. 2231–49, 1996.

N. K. Georgieva, S. Glavic, M. H. Bakr, and J. W. Bandler, “Feasible adjoint sensitivity technique for EM design optimization,” *IEEE Trans. Microwave Theory Tech.*, vol. 50, no. 12, pp. 2751–2758, Dec. 2002.

R. F. Harrington, *Time-Harmonic Electromagnetic Fields*, McGraw-Hill Inc., chapter 6, pp. 264–307, 1961.

IEEE standard board, *IEEE standard definitions of terms for antennas*, IEEE Std 145-1993 (NY, USA: IEEE), 1993.

J. M. Johnson, and Y. Rahmat-Samii, “Genetic algorithm and method of moments for the design of integrated antennas,” *IEEE Trans. Antennas Propagat*., Vol. 47, pp. 1606-1614, Oct. 1999.

L. E. Larsen, and J. H. and Jacobi, *Medical Applications of Microwave Imaging*. New York: IEEE Press, 1986.

M. Lazebnik, D. Popovic, L. McCartney, C. B. Watkins, M. J. Lindstrom, J. Harter, S. Sewall, T. Ogilvie, A. Magliocco, T. M. Breslin, W. Temple, D. Mew, J. H. Booske, M. Okoniewski, and S. C. Hagness, "A large-scale study of the ultrawideband microwave dielectric properties of normal, benign, and malignant breast tissues obtained from cancer surgeries," *Physics in Medicine and Biology*, vol. 52, pp. 6093-6115, 2007.

L. Liu, A. Trehan, and N. K. Nikolova, “Near-field detection at microwave frequencies based on self-adjoint response sensitivity analysis,” *Inverse Problems*, vol. 26, 105001, 2010.

MATLAB (R2010a), The MathWorks, Inc., USA, 2010.

R. M. Meaney, M. W. Fanning, D. Li, S. P. Poplack, and K. D. Paulsen, “A clinical prototype for active microwave imaging of the breast,” *IEEE Trans. Microwave Theory Tech*., vol. 48, no. 11, pp. 1841–1853, 2000.

N. K. Nikolova, J.W. Bandler, and M. H. Bakr, “Adjoint techniques for sensitivity analysis in high-frequency structure CAD,” *IEEE Trans. Microwave Theory Tech*., vol. 52, no. 1, pp. 403–419, Jan. 2004.

N. K. Nikolova, R. Safian, E. A. Soliman, M. H. Bakr, and J. W. Bandler, “Accelerated gradient based optimization using adjoint sensitivities,” *IEEE Trans. Antennas Propag*., vol. 52, pp. 2147–2157, Aug. 2004.

N. K. Nikolova, H. W. Tam, and M. H. Bakr, “Sensitivity analysis with the FDTD method on structured grids,” *IEEE Trans. Microwave Theory Tech*., vol. 52, no. 4, pp. 1207–1216, Apr. 2004.

N. K. Nikolova, J. Zhu, D. Li, M. H. Bakr, and J. W. Bandler, “Sensitivity analysis of network parameters with electromagnetic frequency-domain simulators,” *IEEE Trans. Microwave Theory Tech*., vol. 54, No. 2, pp. 670–681, Feb. 2006.

N. K. Nikolova, Y. Li, Y. Li, and M. H. Bakr, “Sensitivity analysis of scattering parameters with electromagnetic time-domain simulators,” *IEEE Trans. Microw. Theory Tech*., vol. 54, no. 4, pp. 1598–1610, Apr. 2006.

N. K. Nikolova, X. Zhu, Y. Song, A. Hasib, and M. H. Bakr, “S-parameter sensitivities for electromagnetic optimization based on volume field solutions,” *IEEE Trans. Microwave Theory Tech*., vol. 57, no. 6, pp. 1526–1538, June 2009.

N. K. Nikolova, “Microwave imaging for breast cancer detection,” *IEEE Microwave Magazine*, vol. 12, pp. 78–94, 2011.

M. Pastorino, A. Massa, and S. Caorsi, “A global optimization technique for microwave nondestructive evaluation,” *IEEE Trans. Instrum. Meas.*, vol. 51, no. 4, pp. 666–673, 2002.

M. Pastorino, *Microwave Imaging*. USA: John Wiley & Sons, Inc., 2010.

M. Ravan, R. K. Amineh, and N. K. Nikolova, “Two-dimensional near-field microwave holography,” *Inverse Problems*, vol. 26, 2010.

I. T. Rekanos, S. M. Panas, T. D. Tsiboukis, “Microwave imaging using the finite-element method and a sensitivity analysis approach,” *IEEE Trans. Medical Imaging*, vol.

18, pp. 1108-1114, 1999.

T. Rubaek, P. M. Meaney, P. Meincke, and K. D. Paulsen, “Nonlinear microwave imaging for breast-cancer screening using Gauss–Newton’s method and the CGLS inversion algorithm,” *IEEE Trans. Antennas Propag.*, vol. 55, no. 8, pp. 2320–2331, 2007.

E. A. Soliman, M. H. Bakr, and N. K. Nikolova, “Accelerated gradient-based optimization of planar circuits,” *IEEE Trans. Antennas Propag*., vol. 53, no. 2, pp. 880–883, Feb. 2005.

Sonnet ***em***, Suites 12.52, Sonnet Software, Inc., USA, 2009.

Y. Song and N. K. Nikolova, “Memory efficient method for wideband self-adjoint sensitivity analysis,” *IEEE Trans. Microwave Theory Tech*., vol. 56, no. 8, pp. 1917–1927, Aug. 2008.

A. Trehan, “Numerical and physical models for microwave breast imaging,” M.A.Sc. Thesis, McMaster University, Hamilton, Canada, 2009.

A. Trehan, L. Liu and N. K. Nikolova, “Sytematic fidelity assessment of microwave sensors for near-field imaging,” accepted for presentation at *IEEE AP-S/URSI Int. Symp. On Antennas and Propagation*, 2010.

J. P. Webb, “Design sensitivity of frequency response in 3-D finite-element analysis of microwave devices,” *IEEE Trans. Magn*., vol. 38, no. 2, pp. 1109–1112, Mar. 2002.

A. B. Wolbarst, R. G. Zamenhof, and W. R. Hendee *Advances in Medical Physics*. Madison WI: Medical Physics Publishing, 2006.

E. Fear, X. Li, S. C. Hagness, and M. A. Stuchly, “Confocal microwave imaging for breast cancer detection: localization of tumours in three dimensions,” *IEEE Trans. Biomed. Eng.*, vol. 49, no. 8, pp. 812–822, 2001.

Y. Zhang and N. K. Nikolova, “Sensitivity analysis with discrete perturbation of planar structure on method-of-moment grids,” *IEEE AP-S/URSI Int. Symp. on Antennas and Propagation*, July 2010.

Y. Zhang, N. K. Nikolova, and M. H. Bakr, “Input impedance sensitivity analysis of patch antenna with discrete perturbations on method-of-moment grids,” *Applied Computational Electromagnetics Society Journal*, vol. 25, no. 10, pp. 867−876, Oct. 2010.

Y. Zhang, L. Liu, and N. K. Nikolova, “Resolution study for detection algorithm based on self-adjoint sensitivity analysis with microwave responses,” *Applied Computational Electromagnetics Symposium*, Mar. 2011.

Y. Zhang, L. Liu, and N. K. Nikolova, “Performance study of a microwave imaging method based on self-adjoint sensitivity analysis,” *European Radar Conference*, Oct. 2011.

Y. Zhang, A. Pimpale, M. K. Meshram, and N. K. Nikolova, “Printed antenna design using sensitivity analysis based on method of moment solutions,” *IEEE Radio and Wireless Symposium*, Jan. 2012.

Y. Zhang, N. K. Nikolova, and M. K. Meshram, “Design optimization of planar structures using self-adjoint sensitivity analysis,” *IEEE Trans. Antenna Propag*. vol. 60, no. 6, pp. 3060−3066, June 2012.

Y. Zhang, S. Tu, and N. K. Nikolova, “Sensitivity-based microwave imaging with raster scanning,” *IEEE MTT-S Int. Microwave Symposium*, June 2012.

Y. Zhang, S. Tu, R. K. Amineh, and N. K. Nikolova, “The resolution and robustness to noise study of a sensitivity-based microwave imaging with data acquired on cylindrical surfaces,” *Inverse Problems*, vol. 28, 115006, 2012.

R. Zoughi, *Microwave Non-Destructive Testing and Evaluation*. USA: Kluwer Academic Publishers, 2002.